A Hybrid Physics-Based and Data-Driven Approach for Predicting the Effective Thermal Conductivity of Heterogeneous Solids

A Dissertation

by

FERGANY BADRY

Submitted to the Office of Graduate and Professional Studies of
Texas A&M University
in partial fulfillment of the requirements for the degree of

DOCTOR OF PHILOSOPHY

Chair of Committee,	Karim Ahmed
Co-Chair of Committee,	Sean M. McDeavitt
Committee Members,	Lin Shao
	Pavel V. Tsvetkov
	Bobak J. Mortazavi
Head of Department,	Michael Nastasi

May 2021

Major Subject: Nuclear Engineering

ABSTRACT

Thermal conductivity is one of the most important physical properties of materials. It plays a significant role in operation, performance and efficiency of the nuclear reactors. This study introduces a novel model for the effective thermal conductivity of polycrystalline solids based on the thin-interface description of grain boundaries (GBs). In contrast to existing models, the new model treats a GB as an autonomous “phase” with its own thermal conductivity. The Kapitza resistance/conductance of a thin interface is then derived in terms of the interface thermal conductivity and width. The predictions of the new model deviate from the corresponding ones from existing models by 1-100% as the grain size approaches the GB width. The development and implementation of two quantitative mesoscale models for the effective thermal conductivity of two important types of nuclear fuels are undertaken. These models account for the effects of temperature, underlying microstructure, and interface thermal resistance for calculating the effective thermal conductivity. High-fidelity finite-element simulations were conducted to validate the predictions of the developed models. These simulations proved the higher accuracy of the developed models. Lastly, to reduce the required computational power, advanced machine learning algorithms were integrated with the validated mesoscale models. This approach is novel and significantly saved the running time and computational cost. The advantages and limitations of the developed models are summarized, and some future directions are highlighted.

DEDICATION

This document is dedicated to my family, especially my father, who passed away while I was at the beginning of the path to start this study.

ACKNOWLEDGEMENTS

I would like to express my great gratitude for the inspiring and patient instructions from Prof. Karim Ahmed. It would be impossible for me to carry out this research without his guidance and support. Many thanks to Prof. Sean M. McDeavitt and his group for their cooperation.

I would like to thank my other committee members, Prof. Sean M. McDeavitt, Prof. Lin Shao, Prof. Pavel V. Tsvetkov, and Prof. Bobak Motazavi, for their guidance and support throughout the course of this research.

I would like to thank my colleagues in our research group for their kind help and sweet company during these years.

I acknowledge support from the U.S. Department of Energy, Office of Nuclear Energy through the Nuclear Energy University Program, and also acknowledge the computing resources from INL.

Finally, thanks to my mother, brothers, and sisters for their encouragement. My wife, Sarah Abdellatief, and my children (Salma, Omar, and Ali) for their patience and support.

CONTRIBUTORS AND FUNDING SOURCES

Contributors

This work was supervised by a thesis committee consisting of Professor Karim Ahmed [advisor], Professor Sean M. McDeavitt, Professor Lin Shao, and Professor Pavel V. Tsvetkov of the Department of Nuclear Engineering, Texas A&M University, and Professor Bobak Motazavi of the Department of Computer Science & Engineering, Texas A&M University.

Funding Sources

The authors for this work would like to acknowledge the support from the Department of Energy Office of Nuclear Energy (DE- NE0008764). Portions of this research were conducted with the advanced computing resources provided by Texas A&M high-performance research computing and the computing resources from INL.

NOMENCLATURE

UO_2	Uranium dioxide
BeO	Beryllium oxide
U-Zr	Uranium Zirconium
Dep_U.	Depleted Uranium
T	Temperature
GBs.	Grain-Boundaries
R_k	Kapitza Resistance
G_k	Kapitza Conductance
K_{int}	Interface Thermal Conductivity
K_b	bulk Thermal Conductivity
l	Interface thickness
D_f	Fractional difference
K_{2D}	Thermal conductivity based on 2D simulations
K_{3D}	Thermal conductivity based on 3D simulations
RMSE	Root-mean-square error
r	Pearson's correlation coefficient
ML	Machine learning
DL	Deep Learning

TABLE OF CONTENTS

Page

LIST OF FIGURES

Page

LIST OF TABLES

Page

CHAPTER I

INTRODUCTION

1.1. Background and Motivation

Thermal conductivity is one of the most important physical properties of materials. It is the main attribute that determines the material of choice in several industrial and technological applications. For instance, materials used in thermal barrier coatings and thermoelectric materials should have low thermal conductivity, while common materials suited for electronic devices and nuclear fuel fabrication must exhibit high thermal conductivity.

Similar to most physical properties of solids, thermal conductivity is sensitive to the underlying microstructure[1-11]. The main reason for this dependency is the effect of interfaces in heterogeneous materials on the overall heat transfer. Interfaces usually act as obstacles for heat conduction by scattering heat carriers. For example, polycrystalline solids generally show lower thermal conductivity than the corresponding bulk single crystals. More reduction can be seen as grain size decreases. Nonetheless, interfaces can also be engineered to improve the overall conductivity of heterogeneous materials by precipitating out a highly conducting phase, adding highly conductive intermediate layers, or doping[12, 13].

Attempting to understand the interaction between heat carriers and interfaces is a very active area of research[8-37]. An in-depth comprehension of this process is still not fully achieved[32, 35, 37]. For most purposes, however, it is the effective/overall thermal conductivity of the inhomogeneous material that is of interest. Nonetheless, accurate predictions of the effective thermal conductivity require a precise description of the interfacial heat transport.

Several models and simulation techniques were developed for predicting the conductivity of polycrystals [8-10, 12-37]. They can be classified into two main categories, continuum and atomistic/particulate models. The acoustic mismatch model, diffuse mismatch model[38], and molecular dynamics simulations preserve the underlying particulate nature of heat carriers [12, 13, 32, 35, 37]. Continuum models and finite element simulations, on the other hand, utilize specific constitutive laws and interfacial boundary conditions that coarse grain the atomistic details [8-11, 15-22, 39, 40]. The advantages of continuum models are the simplicity of implementation and usage, ease of interpretation of results, and capability of verification and validation using relatively

simple experiments. In these models, the most crucial parameter that accounts for interfacial transport is the thermal boundary (Kapitza) resistance/conductance. This parameter, however, can be determined only from atomistic models or advanced experiments. Several studies have shown that its value depends on grain boundary (GB) energy, GB misorientation angle, GB excess volume, and strain energy[30-35].

Moreover, similar to heterojunctions in semiconductors [12, 13], segregation and interface structure/phase transition are expected to affect the value of the Kapitza resistance as well. Yet, all these factors are not taken into consideration in the analytical and continuum models[8-10] commonly used in literature[10, 14-29]. Since these models are based on the sharp-interface description of GBs, their predictions for nano-sized polycrystalline solids are questionable. Moreover, experimental data of many materials are limited due to the high cost and technical challenges of conducting these experiments.

This study aims to investigate, examine, and quantify the effect of microstructure heterogeneity/interfaces on effective thermal conductivity. First, this study will focus on the impact of GBs on the effective thermal conductivity of polycrystalline solids. Second, the primary treatment and concepts will be adapted to other types of interfaces and/or heterogeneous solids, namely a composite uranium dioxide-beryllium oxide (UO2-BeO) and uranium - zirconium (U-10Zr) nuclear fuels. One of the significant contributions of this work is that a joint experimental and modeling approach is used to quantify the Kapitza resistance between the fuel components. Then, the obtained Kapitza resistance is utilized to improve the accuracy of predictions for the effective thermal conductivity of heterogeneous fuel. Lastly, we will modify and incorporate novel machine learning (ML) methods to resolve the experimental and computational challenges [32, 41-47].

1.2. Significance of work

Thermal conductivity is one of the most important physical properties of materials. It is the main attribute that determines which material can be used in several industrial and technological applications. This study focuses on the effect of the microstructure heterogeneity on the effective thermal conductivity. This is a crucial step to develop materials with specific thermal properties such as thermoelectric materials and nuclear fuels. Unlike previous work in the literature, the

current study introduces a new continuum model that alleviates the shortcomings of the existing models mentioned above. The proposed model is based on the thin-interface description of GBs/interfaces. This description is common in the thermodynamic theory of heterogeneous materials, which treats GBs and interfaces as autonomous "phases" [41]. In deriving the model, the current study introduces an expression for the effective/average Kapitza resistance/conductance of a thin interface. This model then can account for the changes in thermal resistance/conductance of an interface due to, but not limited to, segregation/doping, localized phase transition, or confined irradiation or mechanical damage. Furthermore, this study introduces the development and implementation of two quantitative mesoscale models for the effective thermal conductivity of two important types of nuclear fuels. These models account for the effects of temperature, underlying microstructure, and interface thermal resistance for calculating the effective thermal conductivity. Additionally, this work uses a joint experimental and modeling approach to quantify the Kapitza resistance between the fuel components; this is an unpreceded achievement, and it is important to understand the effect of fuel microstructure on the effective thermal conductivity, then on the reactor's operation, performance and safety. In order to resolve the encountered challenges with experimental work (such as technical difficulties) and computational work (e.g., computational power), the current study presents a new approach, which is a combination of suitable machine learning (ML) algorithms and validated mesoscale models. This approach is novel and significantly saves running time and computational cost.

1.3. Objectives

The main objective of this study is to investigate, examine and quantify the effect of microstructure on the effective thermal conductivity through:

- Developing a novel model for the effective thermal conductivity of heterogeneous solids based on the thin-interface description of interfaces.
- Developing a general formula for the effective Kapitza resistance of a thin interface.

- Developing an experimentally validated mesoscale model of thermal conductivity of composite UO_2 and BeO and metallic U-Zr nuclear fuels.
- Developing a hybrid ML–Mesoscale Simulation-based approach to thermal conductivity modeling.

1.4. Thesis Layout

The structure of this dissertation was generally shaped by published and submitted journal papers, and is organized as follows. Chapter II gives an overview of a new model of effective thermal conductivity and develops a new general expression for the Kapitza resistance. This chapter is based on the paper entitled "A new model for the effective thermal conductivity of polycrystalline solids" published in *AIP Adv*, volume 10, issue 10 in year 202, and reprinted with permission from AIP. Chapter III presents an experimentally validated mesoscale model of the effective thermal conductivity of a UO2 and BeO composite nuclear fuel. Through this chapter, two types of fuel microstructures (dispersed and continuous) were investigated. This chapter is based on the paper entitled "An Experimentally Validated Mesoscale Model of Thermal Conductivity of a UO2 and BeO Composite Nuclear Fuel" published in *journal of materials*, volume 71, issue 12 in year 2019, and reprinted with permission from Springer. Chapter IV describes experimentally validated mesoscale models of the effective thermal conductivity for dep_U and U-Zr. Chapter V develops a hybrid ML– Mesoscale simulation-based approach to thermal conductivity modeling. Finally, chapter VI outlines the summary and the concluding remarks

CHAPTER II

A NEW MODEL FOR THE EFFECTIVE THERMAL CONDUCTIVITY OF POLYCRYSTALLINE SOLIDS[1]

This study proposed a new analytical Kapitza resistance formula based on based on the Fourier law. This expression was verified against a finite element simulation for various spatial dependence functions of grain boundary thermal conductivity. Additionally, a new model for effective thermal conductivity of the polycrystals has been developed by taking into consideration the effect of interface/grain boundary thickness; the new model verified against the finite element simulations and its results are matching well and better than previous models. Both new models are applied to bi-crystal and polycrystal microstructures specifically hexagonal and Voronoi microstructures with steady state and transient calculations that have been done. In all cases that are investigate the new models produced better results than the previous models.

2.1 Modeling and Methodology

2.1.1 A new model of the effective thermal conductivity of heterogeneous solids

Before introducing our new model of the effective thermal conductivity of heterogeneous solids based on a thin interface, we briefly review the classical models that use sharp-interface description. In 1998, using the averaging grain theory [42], Nan and Birringer proposed an analytical model to study the effect of grain size on the effective thermal conductivity of polycrystals. By incorporating the concept of the Kapitza resistance into an effective medium approach, the model describes the effective thermal conductivity for common polycrystals with isotropic, equisized spherical crystallites [1, 9].

$$k = \frac{k_b}{1 + \frac{2k_b R_k}{d}} \tag{2.1}$$

Where, $k_b$is the single crystal thermal conductivity $\left(\frac{W}{m.K}\right)$, R_k is the Kapitza thermal resistance from grain boundaries $\left(\frac{m^2K}{W}\right)$, and d is grain size (nm).

[1] Reprinted with permission from "Fergany Badry and Karim Ahmed, AIP Advances 10, 105021 (2020); licensed under a Creative Commons Attribution (CC BY) license." [43]

This model has been revised by Yang et al. in 2002 by noting that each grain boundary region is shared by two grains[1, 8]. Therefore, instead of Eq. (2.1), the effective thermal conductivity is given by [8]

$$k = \frac{k_b}{1 + \frac{k_b R_k}{d}} \tag{2.2}$$

More recently, Palla and Giordano [11] generalized the above models to anisotropic materials and considered both the high- and low-conductive interfaces. While this generalization made a salient contribution to the earlier work, the dependence of the effective thermal conductivity on grain size remained unchanged. The classical models summarized above are based on a sharp-interface description of the interface. In such description, it is assumed that, while the heat flux is continuous, there is a discontinuity in the temperature field across the GB.

Nonetheless, as mentioned before, at small scale, the thin-interface description provides more natural and accurate treatment of the interfacial region. Moreover, it accounts in a straightforward manner for the possibility of drastic physical property change in this region due to doping, segregation, and/or interface phase transition. Therefore, it is important to develop the thin-interface model of heat transfer across grain boundaries in solids.

The description of the sharp- and thin- interface treatments are schematically illustrated in Figure. 1. In contrast to the sharp-interface description, the thin-interface description treats the interfacial region as autonomous with its own thermodynamic properties (e.g. a surface phase). In its simplest form, which will be considered here, the thin interface implies the continuity of both heat flux and temperature across the boundaries; effectively transforming an imperfect interface into two perfect interfaces separated by a distance equal to the interface width (as shown in Figure. 1). Firstly, in order to derive an equation for the effective thermal conductivity, we generalize here the procedure carried out by Yang et al [8]for the sharp-interface case to the thin-interface case.

The average temperature drop across a grain is T_o. T_{gb} is the temperature drop across a GB due to its thermal (Kapitza) resistance. Similar to the procedure in [1], [8], we examine the temperature profile across a polycrystalline system in response to an applied heat flux q. The heat flux is assumed to follow the classical Fourier's law,

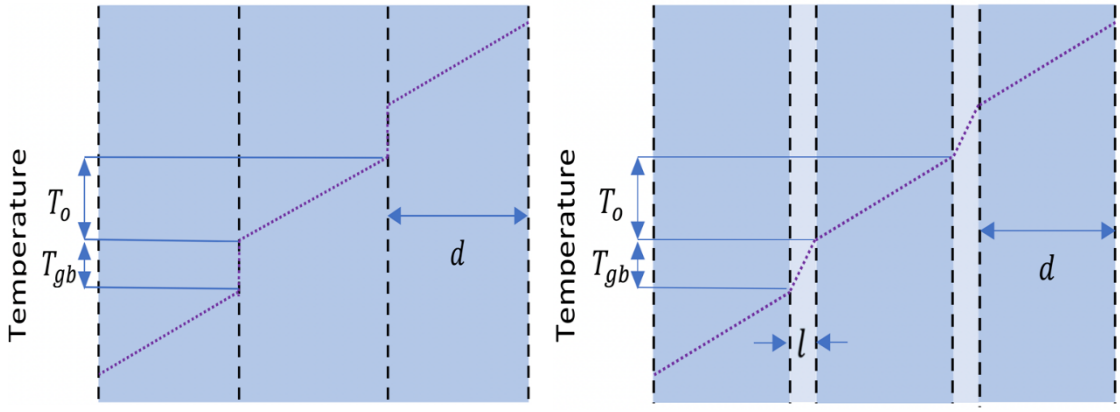

Figure 1. A schematic representation of the sharp- (left, based on) and thin-interface description of temperature drop across grain boundaries in solids. Dashed lines represent grain boundaries.

$$q = -k\frac{dT}{dx} \tag{2.3}$$

As evident from Figure. 1, the total temperature drop across the grain and its boundary is

$$T_{tot} = T_o + T_{gb} \tag{2.4}$$

By substituting Eq. (2.4) into Eq. (2.3) and rearranging, we obtain

$$k = \frac{-q(d+l)}{T_o + T_{gb}} \tag{2.5}$$

Where $\frac{T_o+T_{gb}}{(d+l)}$ is equivalent to $\frac{dT}{dx}$, and l is the interface thickness (nm).

Similarly, by applying Fourier's law inside the grain, one has

$$T_o = \frac{-qd}{k_b} \tag{2.6}$$

By definition, the Kapitza resistance is the ratio between the temperature drop across the interface to the heat flux passing through it[44], e.g.,

$$R_k = -\frac{T_{gb}}{q} \tag{2.7}$$

Hence,

$$T_{gb} = -qR_k \tag{2.8}$$

By combining Eqs. (2.5), (2.6), and (2.8), we arrive at

$$k = \frac{-q(d+l)}{\frac{-qd}{k_b} - qR_k} \tag{2.9}$$

Or equivalently,

$$k = \frac{(d+l)}{\frac{d}{k_b} + R_k} \tag{2.10}$$

As expected, in the limit where the interface width vanishes, Eq. (2.10) reduces to Eq. (2.2) and we recover Yang et. al. model. It is also worth noting that one can arrive at an equation similar to Eq. (2.10) based on the harmonic-average formula of layered composites [45]. This can be achieved by treating both the grains and grain boundaries as "phases" with their own thermal conductivities, as shown in Figure. 2.

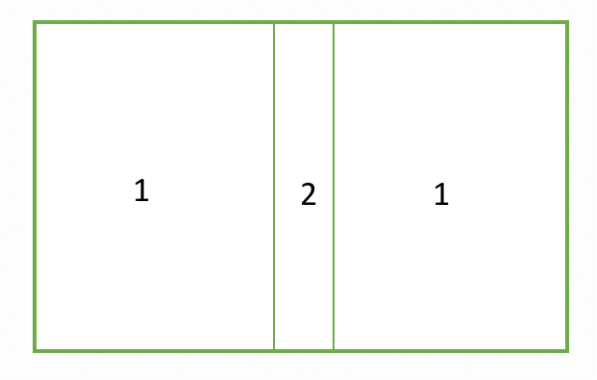

Figure 2. A schematic representation of a bicrystal as a layered composite of two phases, e.g., the grain "phase" (1) and the grain boundary "phase" (2)

In such case, the average thermal conductivity is simply given by,

$$k = (\frac{\emptyset_1}{k_1} + \frac{\emptyset_2}{k_2})^{-1} \tag{2.11}$$

Where, $\emptyset_1$, and $\emptyset_2$ represent bulk volume fraction, and grain boundary volume fraction, respectively, i.e., $k_1 = k_{\mathrm{b}}$, and $k_2 = k_{\mathrm{gb}}$.

The first phase (grain) volume fraction is given by

$$\emptyset_1 = d/(d+l) \tag{2.12}$$

The second phase (grain boundary) volume fraction is

$$\emptyset_2 = l/(d+l) \tag{2.13}$$

By substitution of Eqs. (2.12) and (2.13) in Eq. (2.11), we have

$$k = \frac{1}{\frac{d/(d+l)}{k_b} + \frac{l/(d+l)}{k_{gb}}} \tag{2.14}$$

Or equivalently,

$$k = \frac{(d+l)}{\frac{d}{k_b} + \frac{l}{k_{gb}}} \tag{2.15}$$

The similarity between equations (2.10) and (2.15) is obvious. By comparing Eqs. 2.10 and 2.15, one can relate the interface/Kapitza resistance of the sharp interface to the thermal conductivity of the thin interface as

$$R_k = \frac{l}{k_{gb}} \tag{2.16}$$

Such expression, however, is valid only for the case of constant thermal conductivity of the grains and their boundaries. The generalization of this expression to variable GB conductivity will be considered in the next subsection.

So far, we have shown using two different approaches how to derive the effective thermal conductivity of a polycrystalline solid based on the thin-interface analysis. In such description, the effective thermal conductivity was shown to be

$$k = \frac{(d+l)}{\frac{d}{k_b} + R_k} \tag{2.17}$$

In contrast to the classical sharp-interface-based models of the effective conductivity, here there is a dependence on both the grain size and the grain boundary width. It is interesting to note that the thin-interface-based model always predicts a higher value of the effective thermal conductivity than its sharp-interface-based counterpart. By comparing the new model prediction (Eq. 2.17) with Yang et al model prediction (Eq. 2.2), one can quantify the difference as

$$D_f = \frac{l}{d} \tag{2.18}$$

where D_f is the fractional difference between both analytical models, e.g., $\frac{k_{new\ model}-k_{Yang\ et\ al\ model}}{k_{Yang\ et\ al\ model}}$. As one might expect, the difference increases as the ratio between the grain boundary thickness and grain size increases, with a maximum fractional difference of 100% when the ratio equals one. The predictions of this new model will be validated using finite-element simulations in the next section.

The above thin-interface-based analysis can also be applied to a hetero-interface (interphase interface) between two phases with different bulk conductivities. For such system, in addition to the interfacial parameters, the conductivity, fraction, size and morphology of each phase will affect the effective value. Thus, we generalize the analysis given above for the thermal resistance of grain boundaries to hetero interfaces between different phases. A schematic of this configuration is displayed in Figure. 3. We start again by assuming the validity of Fourier's law of conduction (Eq. 2.3), as shown in Figure.3, the total temperature drop across the two-phase domain is

$$T_{tot} = T_1 + T_{1-2} + T_2 \tag{2.19}$$

By substituting Eq. (2.19) into Eq. (2.3) and rearranging

$$k = \frac{-q(d_1 + d_{1-2} + d_2)}{T_1 + T_{1-2} + T_2} \tag{2.20}$$

Where d_1 : First phase region thicknes, d_{1-2} : Hetero-interface thickness, d_2 : Second phase region thickness, T_1 : Temperature drop through the first phase region, T_{1-2} : Temperature drop across the interface, T_2 : Temperature drop through the second phase region

Where $\frac{T_1+T_{1-2}+T_2}{(d_1+d_{1-2}+d_2)}$ is equivalent to $\frac{dT}{dx}$.

For the case of steady-state heat conduction and by the assumption of the continuity of heat flux, Fourier's law holds in each region. Hence, we have the following relations: for the first phase region,

$$T_1 = \frac{-qd_1}{k_1} \tag{2.21}$$

For the interfacial region (the Kapitza interfacial boundary condition),

$$T_{1-2} = -qR_k \tag{2.22}$$

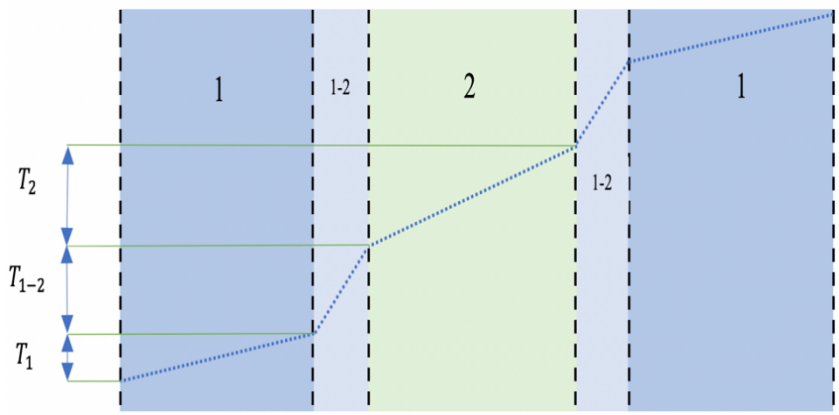

Figure 3. A Schematic representation of a hetero-interface in two-phase systems as a tri-layer composite.

For the second phase region

$$T_2 = \frac{-qd_2}{k_2} \tag{2.23}$$

By combining Eqs. (2.20-2.23), we obtain

$$k = \frac{(d_1 + d_{1-2} + d_2)}{\frac{d_1}{k_1} + R_k + \frac{d_2}{k_2}} \tag{2.24}$$

Clearly, the above analysis was derived based on a specific microstructure, e.g., alternating layers of phases. This simplified the analysis significantly since only 1D treatment is required. Nonetheless, similar to the case of polycrystalline materials considered earlier, the current analysis should apply equally well to configurations with continuous distribution of second phase in isotropic materials.

2.1.2 General formula for the effective Kapitza resistance of a thin interface

As we have shown above, an expression for the effective conductivity of a polycrystalline solid can be derived based on sharp- or thin- interface description of the grain boundary. To shed light into the connection between these two different treatments of interfaces, one must relate the Kapitza/interface thermal resistance of a sharp-interface to both the thin-interface thermal conductivity and width. We derive here such a general formula for the effective thermal resistance of a thin interface.

For the case of steady-state heat conduction, and taking x to be the direction normal to the grain boundary, on has, from Fourier's law,

$$q = -k(x)\frac{dT}{dx} = const \tag{2.25}$$

$$dT = -\frac{q}{k(x)}dx \tag{2.26}$$

For the sake of generality, we assume the thermal conductivity to be spatially dependent. By integrating this equation across the grain boundary/interface, e.g.,

$$\int_0^{T_{gb}} dT = \int_0^{l} \frac{q}{k(x)_{gb}}dx, \tag{2.27}$$

where l , and T_{gb} are the grain boundary width, and the temperature drop through the grain boundary, respectively. For steady-state conditions, we then have

$$\frac{T_{gb}}{q} = \int_0^{l} \frac{dx}{k(x)_{gb}} \tag{2.28}$$

Based on the definition of the Kapitza resistance (recall Eq. (2.7)), one arrives at

$$R_k = \int_0^{l} \frac{dx}{k(x)_{gb}} \tag{2.29}$$

Thus, the Kapitza conductance is

$$G_k = \frac{1}{\int_0^{l} \frac{dx}{k(x)_{gb}}} \tag{2.30}$$

The validation of these formulas of the effective Kapitza resistance and conductance for lowly- and highly conductive thin interfaces with variable conductivities will be verified using finite-element simulations in the next section.

2.1.3 Calculating the effective thermal conductivity of polycrystalline solids

In order to verify the expressions derived above for the thin interface resistance/conductance and the effective thermal conductivity, we utilize a computational approach that combine finite-element and phase-field methods [15, 18, 20, 22, 46-51]. In such approach, constant temperatures T_r & T_l are applied on the right and left sides, respectively. The top and bottom boundaries (y-direction) are taken as adiabatic. Consequently, the thermal gradient points in the x -direction. This configuration is schematically shown in Figure. 4. The heat flux, q, profile in the system is obtained by solving the steady-state conduction equation, e.g.,

$$\nabla.(k\,\nabla T) = 0 \tag{2.31}$$

where k is the thermal conductivity, which varies spatially throughout the domain to account for the underlying microstructure. For the simple case of a bicrystal, which is considered first to validate the model, the location of the grain boundary is known a priori, and Eq. (2.31) can be solved directly. However, for the case of complex grain structures in polycrystalline solids that may undergo grain growth, we use the phase-field method to represent the microstructure. Specifically, the phase-field model of grain growth [52-56] is utilized to distinguish between grains and grain boundaries, and to track the microstructure evolution during grain growth. In that model, phase-field variables η_i are assigned such that their values indicate the type of region (e.g., gains, or GBs). The thermal conductivity is then assigned based on these values. Lastly, the overall effective thermal conductivity can be calculated from:

$$K_{eff} = \frac{q\,L}{T_r - T_l}, \tag{2.32}$$

where q is the average heat flux, T_r & T_l are the temperatures at right and left boundaries respectively, and L is the width of the simulation domain (see Figure. 4). The Kapitza resistance (R_k) is defined as

$$R_k = \frac{\Delta T}{q} \tag{2.33}$$

where ΔT is the temperature drop through the interface between the two phases and q is the average heat flux.

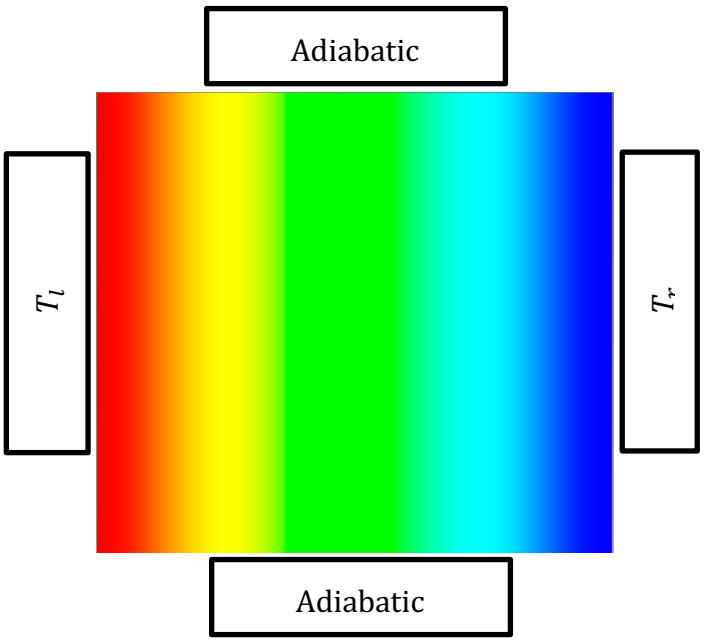

Figure 4. A schematic illustration of the simulation domain used to calculate the effective thermal conductivity.

2.2 Results and Discussion

2.2.1 Validation of the Kapitza resistance/conductance formula for a thin GB

While in most cases interfaces impede heat transport, the concepts of interface engineering can be utilized to optimize the thermal conductivity of the interface [57]. For instance, it was recently shown that mass-graded interlayers enhance the thermal transport through solid-solid interfaces[13]. Moreover, in some situations, the interface conductivity might be higher than the bulk conductivity due to doping and segregation of high thermal conductivity elements in multi-component systems, occurrence of an interface phase transition, or the presence of high density of point and/or line defects in the bulk phases because of irradiation or severe mechanical deformation. We demonstrate here that the derived expressions of Eqs. (2.29) and (2.30) are capable of describing accurately these two scenarios. Namely, Eq. (2.29) gives the Kapitza resistance of a lowly-conducting interface and Eq. (2.30) gives the Kapitza conductance of a highly conducting interface. Furthermore, these relations are also valid even if the interface conductivity changes with position inside the interfacial region. In the coming subsections, we validate both

analytically and numerically the above-mentioned relations for different spatial profiles of the interface thermal conductivity.

2.2.1.1 Kapitza resistance of the lowly-conducting GB

We consider three different interfacial profiles for the thermal conductivity of the GB in a bicrystal configuration as shown in Figure 5 below. For each case, we derive analytically the effective Kapitza resistance of the thin GB using Eq. (2.29). We then verify the results using finite-element simulations.

2.2.1.1.1 Constant profile

$$k(x)_{gb} = k_{gb} \qquad 0 \le x \le l \tag{2.34}$$

k_{gb} is the constant GB thermal conductivity and its value was fixed at 0.1 of the bulk thermal conductivity value (k_b), which is taken to be $1\ W/m.K$. By substituting Eq. (2.34) into Eq. (2.29), we obtain

$$R_k = \int_0^l \frac{dx}{k_{gb}} = \frac{l}{k_{gb}} \tag{2.35}$$

2.2.1.1.2 Linear profile

$$k(x) = \begin{cases} k_b(a + b\,x), & 0 \le x \le \dfrac{l}{2} \\ k_b(c + \mathrm{e}\,x), & \dfrac{l}{2} \le x \le l \end{cases} \tag{2.36}$$

Where $a, b, c, and\ e$ are constants. The interface thermal conductivity value reaches 0.1 of the bulk thermal conductivity at the middle of the GB. Again, by substituting Eq. (2.36) into Eq. (2.29) we obtain,

$$R_k = \int_0^{\frac{l}{2}} \frac{dx}{k_b(a + b\,x)} + \int_{\frac{l}{2}}^{l} \frac{dx}{k_b(c + \mathrm{e}\,x)} \tag{2.37}$$

Which upon integration gives,

$$R_k = \frac{l}{k_b}\left[\frac{1}{b}\ln\left(a+\frac{b\,l}{2}\right)-\frac{1}{b}\ln(a)+\frac{1}{\mathrm{e}}\ln(c+\mathrm{e}l)-\frac{1}{\mathrm{e}}\ln\left(c+\frac{\mathrm{e}\,l}{2}\right)\right] \tag{2.38}$$

The constants and Kapitza resistance value are listed in Table. 1

2.2.1.1.3 Parabolic profile

$$k(x) = k_b(a+bx^2) \qquad -\frac{l}{2} \le x \le \frac{l}{2} \tag{2.39}$$

Where $a\ and\ b$ are constants which are taking specific values to set the interface thermal conductivity as 0.1 of the bulk thermal conductivity at the middle of the GB. By substituting Eq. (2.39) into the new formula Eq. (2.29).

$$R_k = \int_{-\frac{l}{2}}^{\frac{l}{2}} \frac{dx}{k_b(a+bx^2)} \tag{2.40}$$

Direct integration yields,

$$R_k = \frac{2}{k_b\sqrt{ab}}\left[\tan^{-1}\left(\frac{l}{2}\sqrt{\frac{b}{a}}\right)\right] \tag{2.41}$$

The constants and Kapitza resistance value are also listed in Table. 1

To verify the above results, we perform finite-element simulations of the bicrystal configurations shown in Figure. 5. In these simulations, the grain size was 10 nm , the grain boundary width was 2.5 nm, and the bulk conductivity was 1 $W/m.K$. From the simulations, we calculate the Kapitza resistance directly from the flux and thermal gradient across the grain boundary as given by Eq. (2.7). The analytical and numerical values of the Kapitza resistance are included in Table 1 below.

Table 1 analytical and numerical Kapitza resistance results for lowly-conducting grain boundary where, $\boldsymbol{l = 2.5\ nm}$, and $\boldsymbol{k_b = 1\ W/m.K}$

Spatial dependence profile	Constants				Kapitza resistance $(m^2.k)$/W		
					New formula	FEM	
	a	b	c	e		Δx = 0.5 nm	Δx = 0.025 nm
Constant	N/A	N/A	N/A	N/A	2.5×10^{-8}	2.5×10^{-8}	2.5×10^{-8}
Linear	1	$-1.8/l$	-0.8	$1.8/l$	6.396×10^{-9}	6.3132×10^{-9}	6.3960×10^{-9}
Parabolic	0.1	$3.6/l^2$	N/A	N/A	1.0409×10^{-8}	1.0362×10^{-8}	1.0409×10^{-8}

As evident from Table 1, the FEM numerical results agree well with the newly derived Kapitza resistance formula (Eq. (2.29)) and are in close agreement for all spatial profiles of the GB thermal conductivity. This agreement improves with a decrease in element size (or equivalently increasing the number of elements inside the GB). It is worthy to note that the spatial profile of the thermal conductivity of the GB affects the Kapitza resistance, with the constant profile leading to the highest value and the linear profile resulting in the lowest value.

2.2.1.2 Kapitza conductance of the highly conducting GB

Again, we consider three different interfacial profiles for the thermal conductivity of the grain boundary in a bicrystal configuration as shown in Figure 6 below. For each case, we derive analytically the effective Kapitza conductance of the thin GB using Eq. (2.30). We then verify the results using finite-element simulations.

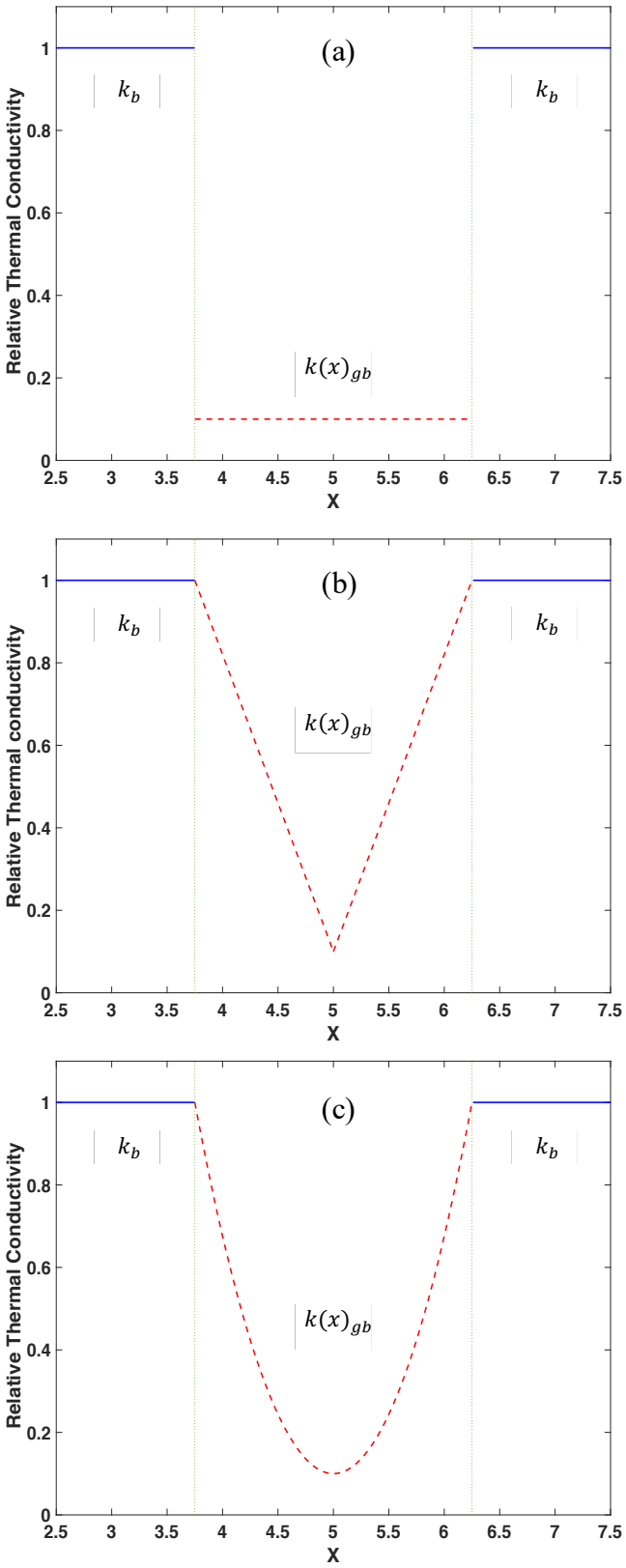

Figure 5. (a), (b), and (c) show constant, linear, and parabolic variation of thermal conductivity, respectively inside the grain boundary thickness with lower values than the bulk thermal conductivity- Kapitza Resistance.

2.2.1.2.1 Constant profile

To represent the highly conductive interface, the GB thermal conductivity was fixed to be 10 times the bulk thermal conductivity value (see Figure 6-a). By combining Eqs. (2.30) and (2.34), we obtain

$$G_k = \frac{1}{\int_0^l \frac{dx}{k_{gb}}} \tag{2.42}$$

which immediately gives,

$$G_k = \frac{k_{gb}}{l} \tag{2.43}$$

2.2.1.2.2 Linear profile

With specific values of $a, b, c, and\ e$ constants (recall Eq. (2.36)), the GB thermal conductivity was fixed to be 10 times the bulk thermal conductivity value at the middle of the GB (see Figure. 6-b) . By combining Eqs. (2.30) and (2.36) we obtain

$$G_k = \frac{1}{\int_0^{\frac{l}{2}} \frac{dx}{k_b(a + b\,x)} + \int_{\frac{l}{2}}^{l} \frac{dx}{k_b(c + \mathrm{e}\,x)}} \tag{2.44}$$

By direct integration, we arrive at

$$G_k = \frac{k_b}{l\left[\frac{1}{b}\ln\left(a + \frac{b\,l}{2}\right) - \frac{1}{b}\ln(a) + \frac{1}{\mathrm{e}}\ln(c + \mathrm{e}l) - \frac{1}{\mathrm{e}}\ln\left(c + \frac{\mathrm{e}\,l}{2}\right)\right]} \tag{2.45}$$

The constants and Kapitza conductance values are listed in Table. 2.

2.2.1.2.3 Parabolic profile

$$k(x) = k_b(a - bx^2) \qquad -\frac{l}{2} \le x \le \frac{l}{2} \tag{2.46}$$

where $a\ and\ b$ are constants that take specific values to set the interface thermal conductivity to be10 times higher than the bulk thermal conductivity value at the middle of the GB (see Figure. 6-c). By combining Eqs (2.30) and (2.46) we get

$$G_k = \frac{1}{\int_{-\frac{l}{2}}^{\frac{l}{2}} \frac{dx}{k_b(a - bx^2)}} \tag{2.47}$$

which after integration results in

$$G_k = \frac{k_b\sqrt{ab}}{\left[\ln\left|\frac{l}{2}\sqrt{\frac{b}{a}} - 1\right| - \ln\left|\frac{l}{2}\sqrt{\frac{b}{a}} + 1\right| - \ln\left|-\frac{l}{2}\sqrt{\frac{b}{a}} - 1\right| + \ln\left|-\frac{l}{2}\sqrt{\frac{b}{a}} + 1\right|\right]} \tag{2.48}$$

The constants and Kapitza conductance values are shown in Table. 2

Table 2. analytical and numerical Kapitza conductance results for highly-conducting grain boundary where, $\boldsymbol{l = 2.5\ nm}$, and $\boldsymbol{k_b = 1\ W/m.K}$

Spatial profile	Constants				Kapitza conductance W / $(m^2.k)$		
					New formula	FEM	
	a	b	c	e		Δx = 0.5 nm	Δx = 0.025 nm
Constant	N/A	N/A	N/A	N/A	4.0×10^9	4.0×10^9	4.0×10^9
Linear	1	$18/l$	-18	$19/l$	1.5634×10^9	1.5839×10^9	1.5634×10^9
Parabolic	10	$36/l^2$	N/A	N/A	2.0868×10^9	2.1429×10^9	2.0868×10^9

As evident from Table 2, the FEM numerical results agree well with the newly derived Kapitza conductance formula (Eq. (2.30)) and are in close agreement for all spatial profiles of the GB thermal conductivity. This agreement improves with a decrease in element size (or equivalently increasing the number of elements inside the GB). Again, it is worthy to note that the spatial profile of the thermal conductivity of the GB affects the Kapitza conductance, with the constant profile leading to the highest value and the linear profile resulting in the lowest value. This agrees with the interface engineering method proposed in[13], where the enhancement of thermal conductance was shown to depend on the spatial profile of the mass-graded interlayers.

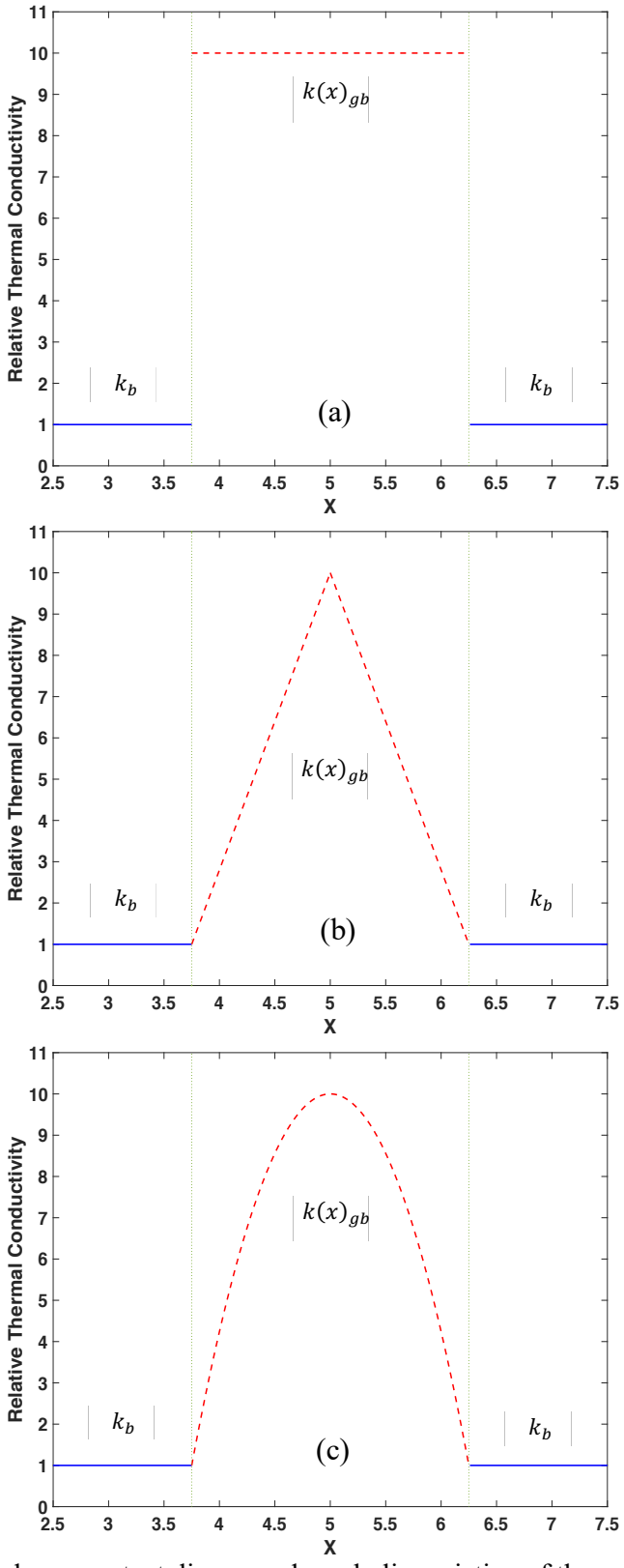

Figure 6. (a), (b), and (c) show constant, linear, and parabolic variation of thermal conductivity, respectively inside the grain boundary thickness with higher values than the bulk thermal conductivity- Kapitza Conductance.

2.2.2 *Effect of the spatial profile of the GB conductivity on the overall thermal conductivity*

In the previous subsection we validated the formulae of the effective Kapitza resistance and conductance of a thin interface. It was shown that these values are affected by how the thermal conductivity of the GB changes with position. Hence, here we study the effect of this change on the overall thermal conductivity. We utilize again the simple configuration of a bicrystal. We run finite-element simulations for the three spatial profiles discussed in the preceding subsection for different grain sizes, with an assumed GB width of 2.5 nm. For both the highly-conducting and lowly-conducting cases, we determine the overall/effective thermal conductivity of the bicrystal using Eq. (2.32) as discussed in section 2.1.3.

For the case of highly conducting GB, Figure. 7 summarizes the general trend. As obvious from the figure, the effective thermal conductivity decreases with the increase of grain size for all spatial profiles of the GB thermal conductivity. This is because in this scenario the GB is the highly conductive 'phase'. This behavior is more pronounced for grain sizes below 100 nm. For instance, as the grain size increases from 10 nm to 100 nm, the effective thermal conductivity decreases by 26.1 %, 22.9%, and 20.5% for the constant, parabolic, and linear spatial profiles, respectively.

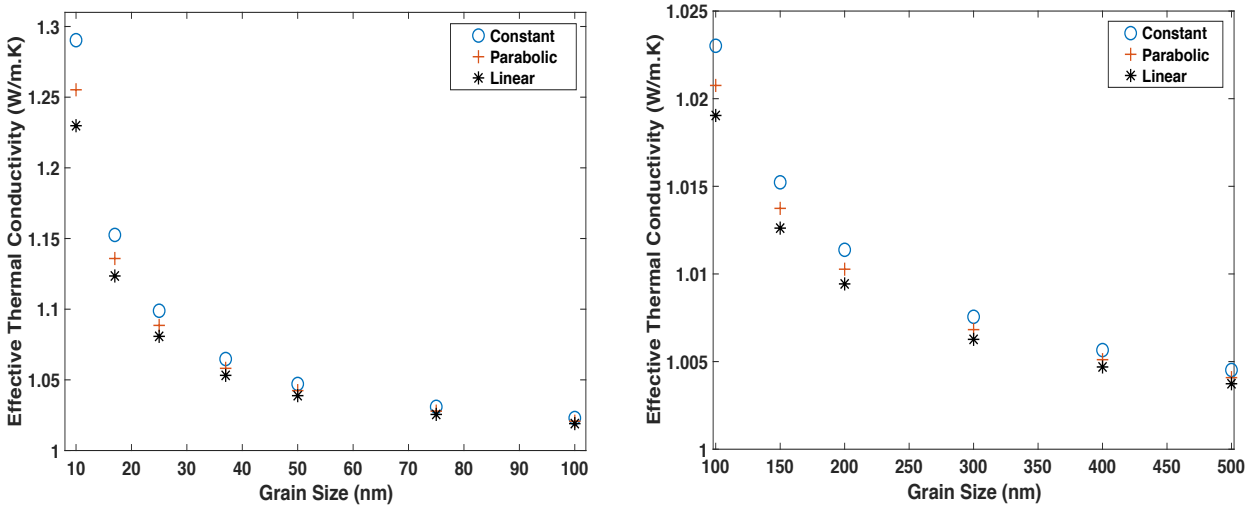

Figure 7. Change of the effective thermal conductivity of a bicrystal with grain size: from 10 nm to 100 nm (left), and from 100 nm to 500 nm (right) for different spatial profiles for the thermal conductivity of the highly-conducting grain boundary.

On the other hand, as the grain size increases from 100 nm to 500 nm, the effective thermal conductivity decreases by 1.84 %, 1.66%, and 1.52% for the constant, parabolic, and linear spatial

profiles, respectively. Additionally, Figure. 7 also shows that for the same grain size the spatial profile leads to different values of the effective thermal conductivity, where the highest value is attained by the constant profile and the lowest value is attained by the linear profile. This is because these profiles have the strongest and weakest Kapitza conductance, respectively (see Table. 2). This variation between the results increases as the grain size decreases. For example, the difference between the effective thermal conductivity produced by the constant and linear spatial dependence functions is 5%, 0.4%, and 0.07% at grain size 10 nm, 100 nm, and 500 nm, respectively.

For the case of lowly-conducting GB, the general trend is depicted in Figure. 8. It shows that, in contrast to the highly conducting boundary, the effective thermal conductivity increases as the grains size increases for all spatial profiles of grain boundary thermal conductivity. This is due to the fact that the grain boundary acts as an obstacle for heat transport, which is commonly the case. Similar to the case of highly conducting boundary, this behavior is more apparent in grain sizes below 100 nm. For instance, as the grain size increases from 10 nm to 100 nm, the effective thermal conductivity increases by 164 %, 65%, and 32.5% for the constant, parabolic, and linear spatial profiles of the GB thermal conductivity, respectively. However, as the grain size increases from 100 nm to 500 nm, the effective thermal conductivity increases by 17.6 %, 6.3%, and 3.2% for the constant, parabolic, and linear spatial profiles, respectively.

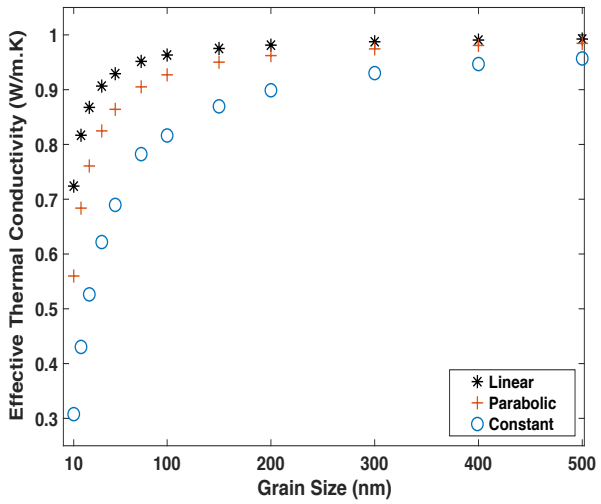

Figure 8. Change of the effective thermal conductivity of a bi-crystal with grain size for different spatial profiles of the thermal conductivity of the lowly-conducting grain boundary.

Thus, different from the case of highly conducting GB, the effective thermal conductivity is still sensitive to variations in the grain size up to 500 nm

It is worth noting that Figure. 8 also demonstrates that for the same grain size, the distinct spatial profiles lead to different values of the effective thermal conductivity, where the lowest value is attained by the constant profile and the highest value is attained by the linear profile. This is in agreement with the predictions listed in Table 1, where the strongest and weakest Kapitza resistances are obtained for the constant and the linear profiles, respectively. Again, similar to the case of highly conducting boundary, the variation of the effective conductivity with the spatial profiles decreases as the grain size increases. For example, the difference between the effective thermal conductivity attained by the constant and linear profiles is 135%, 18.2%, and 3.7% at grain size 10 nm, 100 nm, and 500 nm, respectively. Therefore, in general, for all cases, the sensitivity of the effective thermal conductivity to the GB thermal conductivity reduces with increasing grain size due to the decrease of GB area per unit volume.

2.2.3 Comparison the predictions of the sharp interface and thin interface models

In this subsection, we compare the predictions of the effective thermal conductivity models based on the sharp-interface (Eq. (2.2)) and the thin-interface (Eq. (2.15)) descriptions. We utilize again the simple bicrystal configuration and study the effects of grain size, GB width, and Kapitza resistance. Clearly, the effect of GB width can appear only in the thin interface-based model. Hence, first, to investigate this effect, we run finite-element simulations of the bicrystal configuration with different GB width and grain size. In these simulations, the bulk thermal conductivity was 1.0 W/m.K and the GB thermal conductivity was 0.35 W/m.K.

The results of these simulations are shown in Figure. 9. Generally speaking, the effective thermal conductivity decreases as the GB thickness increases regardless of grain size. While the physical width of a typical GB is usually less than a few nanometers, we expand the results for tens of nanometers to account for scenarios as segregation or grain boundary phase formation that may occur. The dependence of the effective thermal conductivity on the GB width is nonlinear as evident from Figure. 9 and predicted from Eq. (2.15). Since thermal conductivity of the GB is taken as

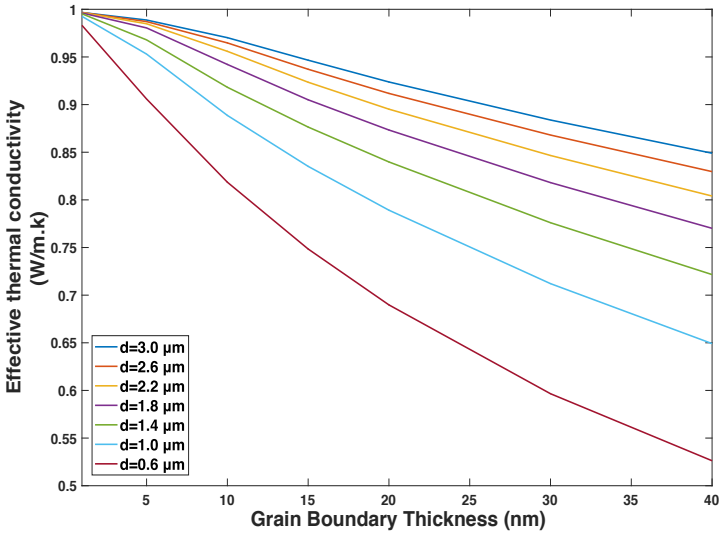

Figure 9. Finite-element simulations of the effect of GB thickness on the effective thermal conductivity of a bicrystal with different grain sizes.

a constant, the Kapitza resistance can be obtained from Eq. (2.35). Hence, the interfacial resistance is directly proportional to the GB thickness. Clearly, for the same interface width/Kapitza resistance, grains with larger sizes attain higher effective thermal conductivities. Moreover, the sensitivity of the effective thermal conductivity to the grain boundary thickness is inversely proportional to grain size.

As discussed above, the effects of GB width and thermal resistance are more pronounced for smaller grain sizes. Hence, we now compare the difference in the predictions of the effective thermal conductivity between Yang et al. model (Eq. (2.2)) and our new model (Eq. (2.15)) for the case of a nanometer-sized bicrystal. As before, the bulk thermal conductivity was taken to be 1 (W/m.k). The effective conductivity is then calculated based on the above-mentioned equations as function of Kapiza resistance and grain size. In our model, the GB width was set to 2 nm. The results are summarized in Figure. 10. First, the effective thermal conductivity is plotted against the Kapitza resistance, where the grain size was fixed at 20 nm. For both models, the effective thermal conductivity decreases as the Kapitza resistance increases. Moreover, it is clear that the new model predicts higher values of the effective thermal conductivity than Yang et al. model, where the difference in values is directly proportional to the Kapitza resistance. For example, the difference increased from 0% to 10% across the range of Kapitza resistance studied. Second, the effective thermal conductivity is plotted against the grain size in the range 2-20 nm, where the Kapitza

resistance was fixed at $20 \times 10^{-9}\, m^2.\frac{k}{W}$. For both models, the effective thermal conductivity increases as the grain size increases. Again, the new model always predicts higher values of the effective thermal conductivity than Yang et al. model for all grain sizes. The difference in the values is inversely proportional to the grain size. For instance, the difference increased from 10% to 100% as the grain size decreased from 20 nm to 2 nm. The reason is that, in contrast to the new model, Yang et al. model neglects the effect of GB thickness, which becomes more apparent as the value of the grain size approaches the value of the GB width.

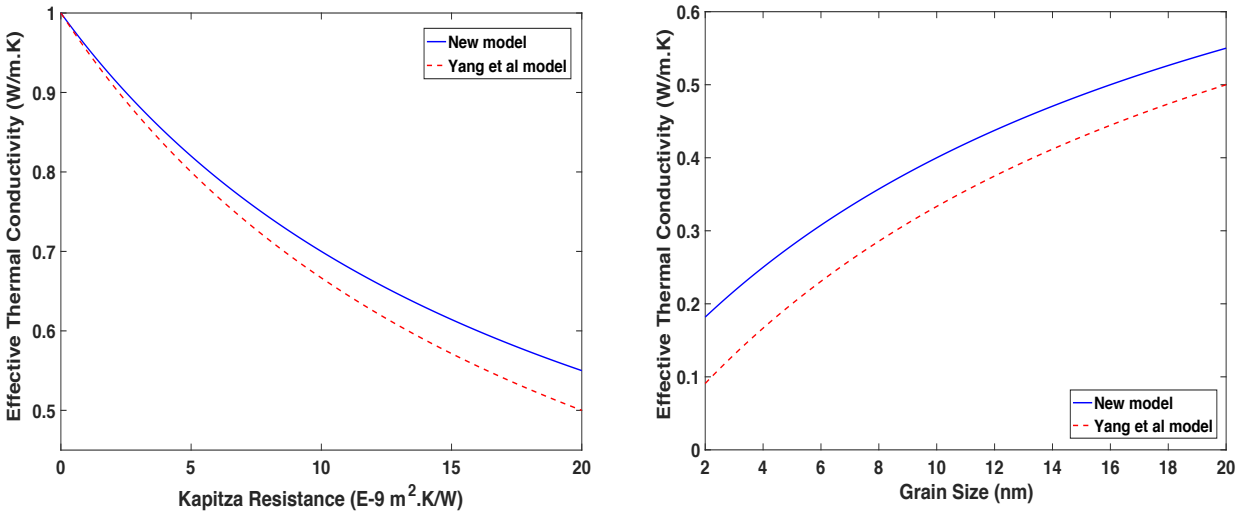

Figure 10. Comparison of the predictions of the new and Yang et al. models for the effective thermal conductivity of a nanometer-sized bi-crystal. The effect of the Kapitza resistance (left) and the effect of grain size (right).

The plots in Figure. 10 were combined into 3D figures to better illustrate the behavior of the two models against variations in both grain size and Kapitza resistance concurrently. These 3D plots are presented in Figure. 11. Both models show qualitatively similar trends. The effective thermal conductivity decreases as the Kapitza resistance increases. For the same Kapitza resistance, the effective thermal conductivity increases with grain size. Moreover, the sensitivity of the effective thermal conductivity to grain size variation is directly proportional to the Kapitza resistance. For instance, for the new model, as the grain size increased from 2 nm to 20 nm, the effective thermal conductivity increased by 36.7% and 205.5% for the Kapitza resistance values of 1×10^{-9} and $20 \times 10^{-9}\, m^2.\frac{k}{W}$, respectively.

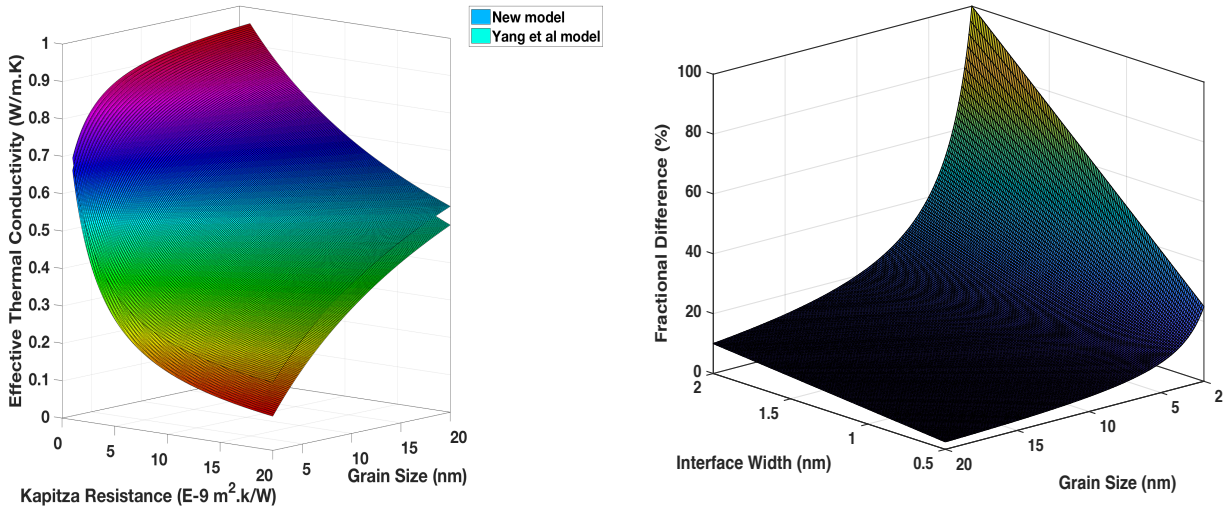

Figure 11. Comparison of the predictions of the new and Yang et al. models for the effective thermal conductivity of a nanometer-sized bi-crystal. The effect of the Kapitza resistance and grain size (left) and the effect of GB width (right). The difference increases

On the other hand, the sensitivity of effective thermal conductivity to variation in the Kapitza resistance is inversely proportional to grain size. For example, for the new model, as the Kapitza resistance value increased from 0 to $20 \times 10^{-9}\, m^2.\frac{k}{W}$, the effective thermal conductivity was decreased by 74 % and 425.5% for the grain size values of 20 and 2 nm, respectively.

While the two models agree qualitatively, there is a notable quantitative difference in their predictions. The new models always predict higher values of the effective conductivity than Yang et al. model. The deviation between the models increases with decreasing grain size. This is also illustrated in Figure. 11 (right subplot). When the grain size becomes equal to the grain boundary width, a maximum fractional difference of 100% is realized (recall Eq. 2.18).

2.2.4 Comparison of the predictions of the analytical models based on data from simulations and experiments

To further investigate the differences between the analytical models, we compare their predictions using new finite-element simulations and existing results from molecular dynamics simulations

and experiments. Note that similar to Yang et al. model, our model can predict either the effective thermal conductivity given the Kapitza resistance or the Kapitza resistance given the effective thermal conductivity. We will utilize those two indicators in comparing the models.

2.2.4.1 Comparison of models using FEM simulations of a bicrystal

We compare here the predictions of the analytical models for the effective thermal conductivity value as function of Kapitza resistance for specific grain sizes. Two different grain sizes of 200 nm and 20 nm were considered. Finite-element simulations of a bicrystal with different values of the Kapitza resistance were performed. The bulk thermal conductivity and GB width were taken as 1 W/m.k and $2nm$, respectively. Figure. 12 summarizes the results of the analytical models and the finite-element simulations. As evident from the figure, the new model is always closer to the results from the numerical simulations than Yang et al. model for all values of grain size and Kapitza resistance. The deviation becomes more apparent for smaller grain sizes. The difference between both analytical models is 1% for the 200 nm grain size and 20% for the 20 nm grain size. Moreover, Figure. 12 also shows that, for the same effective conductivity, the new model always predicts higher values for the Kapitza resistance for all grain sizes.

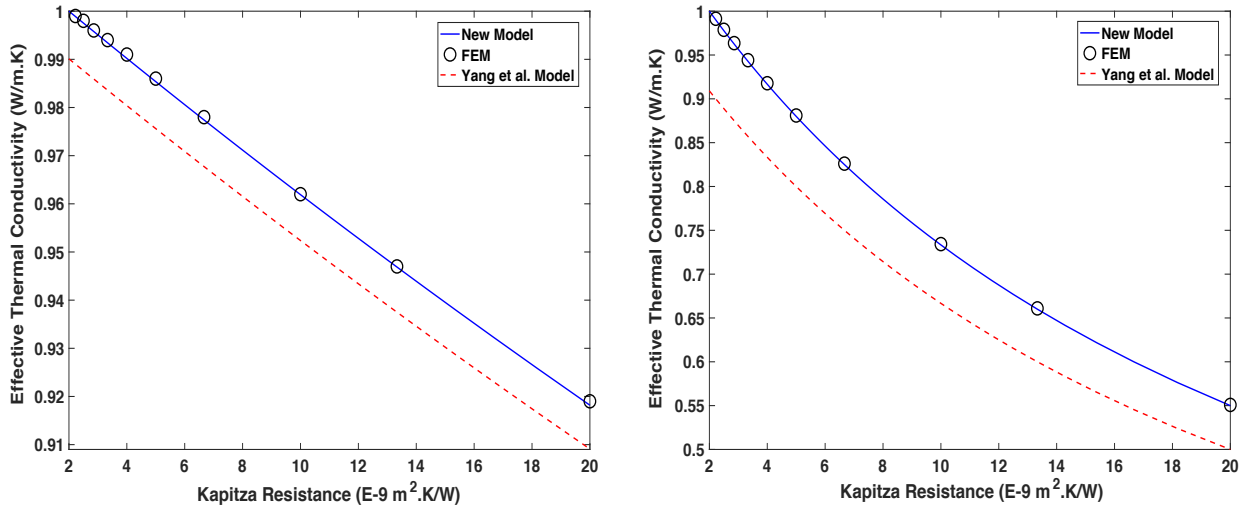

Figure 12. Comparison between the predictions of our new model, Yang et al. model, and FEM simulations for a bicrystal with grain sizes of 200 nm (left) and 20 nm (right).

2.2.4.2 Comparison of models using molecular dynamics simulations of solid argon

Here, we compare the models with the molecular dynamics simulations (MD) of nanocrystalline argon reported in [28]. To keep argon in solid state, where it assumes an FCC crystal structure, the temperature was set to 30 K [28]. Based on the literature, the GB width is about 1-2 nm for similar materials [58-60]. Hence, the Kapitza resistance will be determined for that range. To achieve that goal, for a specific GB width, we fit our model (Eq. (2.15)) to the effective thermal conductivity calculations from the MD simulations. An example of this fitting procedure is shown in Figure. 13. The two-sharp interface-based models (Eq. (2.1) and Eq. (2.2)) were also fitted against the MD results. The predicted values of the Kapitza resistance for the three analytical models are summarized in Table 3. Based on the results listed in Table 3, the Kapitza resistance predicted by our new model is higher than the value from Yang et al. model by 44.3 % for a 1 nm boundary width and by 88% for 2 nm boundary width.

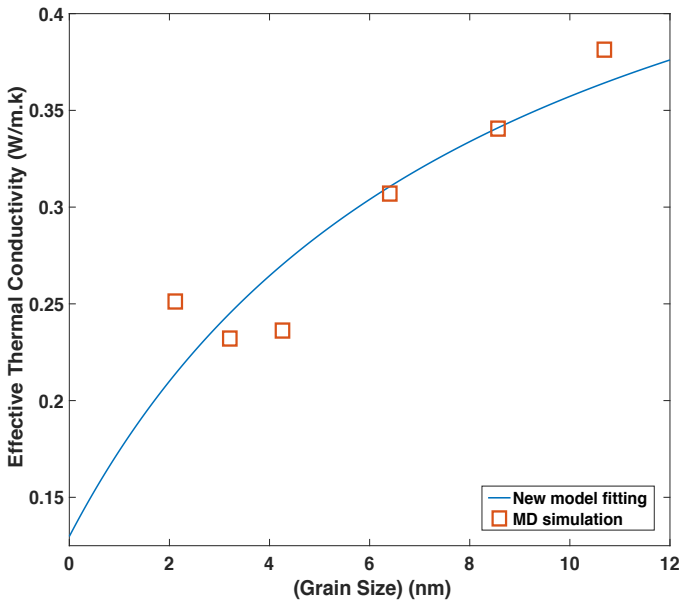

Figure 13. Fitting of the results of molecular dynamics simulations for the effective thermal conductivity of solid argon at 30 K. The solid line is the best fit to the new model (Eq. (2.15)).

Table 3. The Kapitza resistance predicted by the different analytical models.

Fitted model		$l\ (nm)$	R_k (m^2 K/W)
Nan and Birringer	$k = \frac{k_b}{1 + 2R_k k_b/d}$	N/A	4.096×10^{-9}
Yang et al.	$k = \frac{k_b}{1 + R_k k_b/d}$	N/A	8.192×10^{-9}
New model	$k = \frac{(d+l)}{\frac{d}{k_b} + R_k}$	1	11.82×10^{-9}
		1.5	13.62×10^{-9}
		2	15.41×10^{-9}

2.2.4.3 Comparison of models using experimental data of platinum

Here, we compare the predictions of the models using experimental data for in-plane thermal conductivity of polycrystalline platinum nanofilms, reported in [61] . The thickness of the nanofilms ranges from 15.0 to 63.0 nm and the mean grain size measured by x-ray diffraction varies between 9.5 and 26.4 nm [61]. To determine the Kapitza resistance, the three analytical models (Eqs. (2.1), (2.2), and (2.15)) were fitted against the experimental data of platinum. An example of this fitting procedure is shown in Figure. 14. The predicted values of the Kapitza resistance for the three analytical models are listed in Table 4. The Kapitza resistance predicted by our new model is higher than the value from Yang et al. model by 10.8% for a 1 nm boundary width and by 21.5% for a 2 nm boundary width. A final comment on the differences between the analytical models is now in order. As we mentioned before, the first model proposed by Nan and Birringer misses the fact that a GB is shared by two grains [9]. Therefore, that model underestimates the Kapitza resistance by a factor of two as was shown by Yang et al. [8]. Our new model takes another step forward by taking into consideration the effect of the GB width, which makes it more suitable to model nanocrystalline solids.

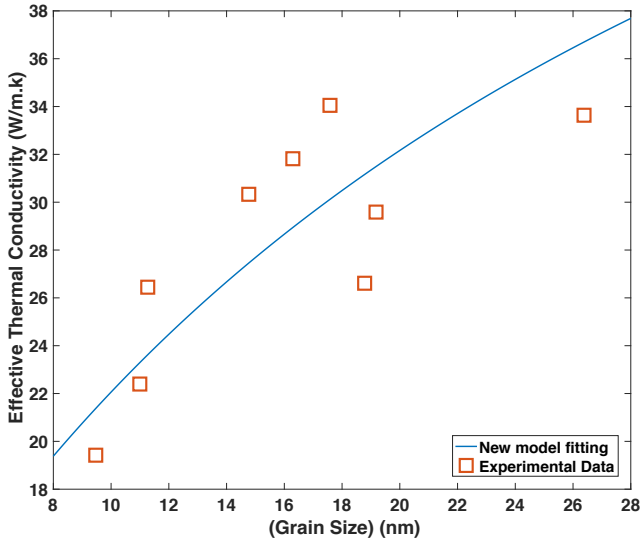

Figure 14. Fitting of the experimental data for the effective thermal conductivity of platinum. The solid line is the best fit to the new model (Eq. (2.15)).

Table 4. The Kapitza resistance predicted by the different analytical models.

Fitted model		$l\ (nm)$	R_k (m^2 K/W)
Nan and Birringer	$k = \frac{k_b}{1 + 2R_k k_b/d}$	N/A	0.1662×10^{-9}
Yang et al.	$k = \frac{k_b}{1 + R_k k_b/d}$	N/A	0.3324×10^{-9}
New model	$k = \frac{(d+l)}{\frac{d}{k_b} + R_k}$	1	0.3682×10^{-9}
		1.5	0.3861×10^{-9}
		2	0.4039×10^{-9}

2.2.5 Simulations of the effective thermal conductivity of polycrystalline solids

Here we validate our new model for the case of polycrystalline solids using representative microstructures. To that end, we use the phase-field method to generate and evolve these microstructures. Specifically, we utilize the phase-field model of grain growth that is implemented in the open-source MOOSE framework[62]. We investigate two microstructures: (1) a static microstructure with hexagonal grains, (2) a dynamic microstructure with equiaxed grains.

2.2.5.1 Effective thermal conductivity of static hexagonal grains

We investigate first the effective thermal conductivity of a static microstructure with hexagonal grains. Since hexagonal grains have straight sides, curvature-driven grain growth cannot take place. Thus, steady state calculations were performed using a bulk conductivity of 1 W/mK, GB conductivity of 0.1 W/mK, and a GB width of 2 nm. The results of the finite-element simulations and the analytical models are compared in Figure. 15. As can be seen from the figure, the effective thermal conductivity increases with grain size because of the reduction in the total GB area as the grain size increase. It is also clear from the figure that the predictions of the new model agree more closely with the FEM results than the model of Yang et al. For instance, the difference between the results of Yang et al. model and FEM varied from 2.73 % to 11.48 % across the grain size range studied. On the other hand, the difference between the results of the new model and FEM varied from 0.03 % to 0.24 % across the same grain size range.

As we discussed before, another way to evaluate the models is to compare their predictions of the Kapitza resistance instead of the effective conductivity, similar to the work presented in subsection 2.2.3. From the FEM simulations, the Kapitza resistance can be calculated directly from the flux and temperature gradient across the grain boundary as given by Eq. (2.7). For the analytical models, the Kapitza resistance can be obtained by fitting the equations of the models given the grain size and effective conductivity data from the finite-element simulations. The value of the Kapitza resistance obtained directly form the FEM simulation was $20 \times 10^{-9}\, m^2.\frac{k}{W}$. The predictions of the analytical models are listed in Table 5. As evident from the table, the new model displays better agreement with the numerical value.

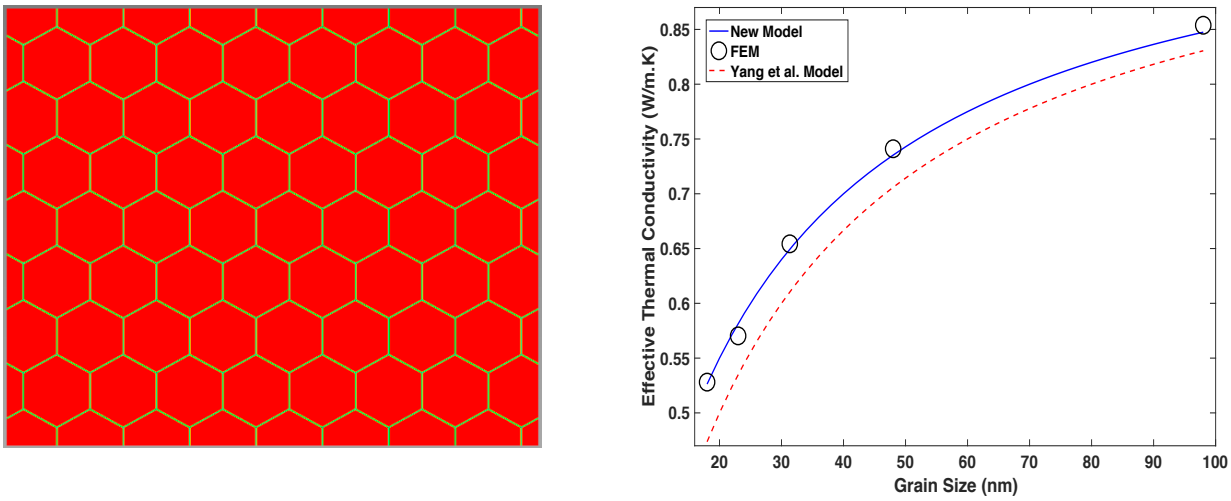

Figure 15. Effective thermal conductivity of a polycrystalline solid with hexagonal grains: (left) a snapshot of the microstructure, (right) the quantitative change of the effective thermal conductivity with grain size.

Table 5. Errors in the values of the Kapitza resistance obtained from the analytical models

Fitted Model		$R_k\ (m^2.\frac{k}{W})$	Error
Yang et al Model	$k = \frac{k_b}{1 + R_k k_b / d}$	16.67×10^{-9}	16.65 %
New model	$k = \frac{(d + l)}{\frac{d}{k_b} + R_k}$	19.94×10^{-9}	0.3 %

2.2.5.2 Effective thermal conductivity of evolving equiaxed grains

Here, we study the changes of the effective thermal conductivity in polycrystalline solids undergoing grain growth. Voronoi tessellation is utilized to approximate the shapes of random equiaxed grains. Since the effective conductivity is sensitive to the grain size, its value is expected

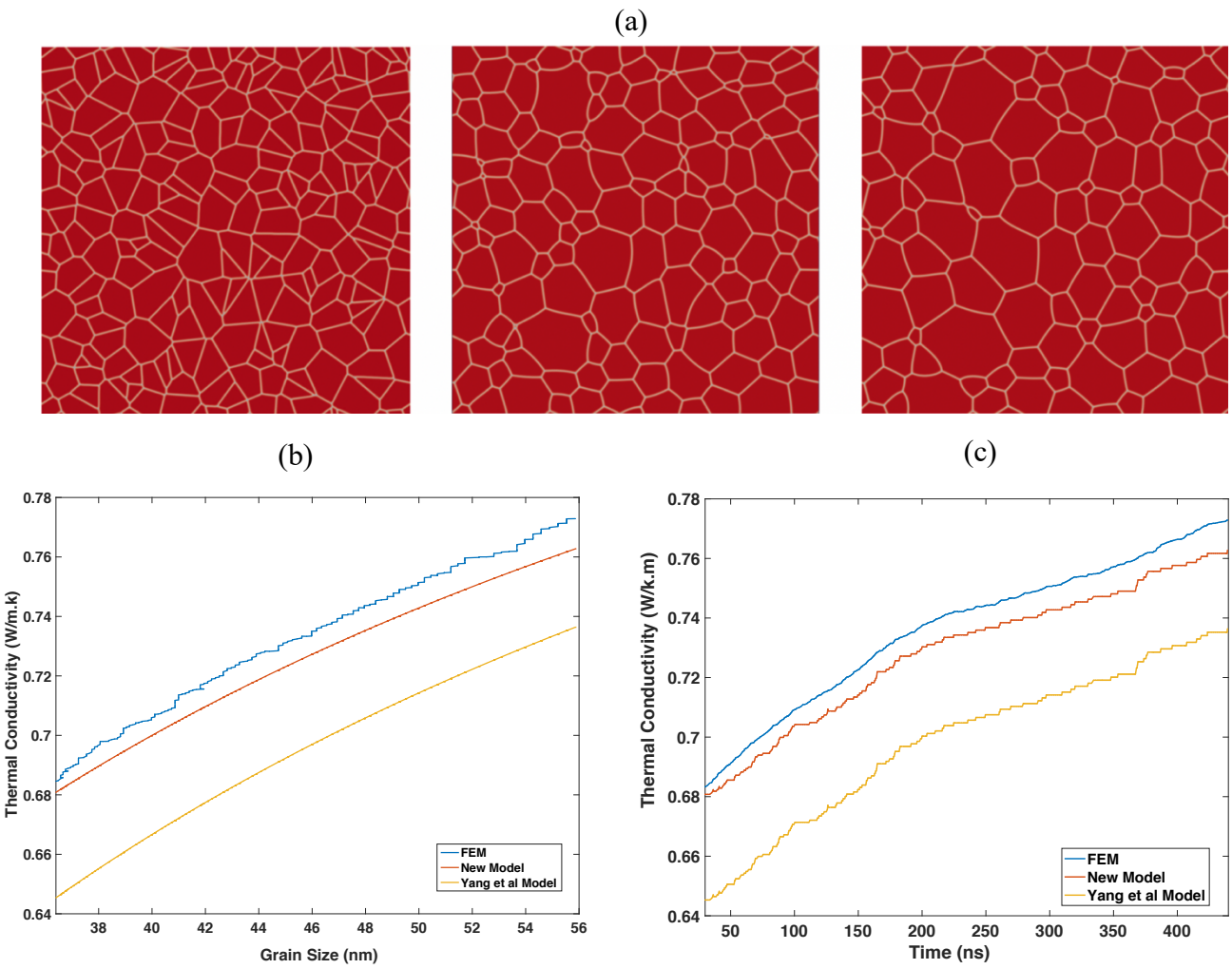

Figure 16. Variation of the thermal conductivity of a polycrystalline solid during grain growth. (a) Snapshots of the microstructure evolution, and the corresponding change of the effective thermal conductivity with (b) grain size and (c) time.

to vary during grain growth. To capture this variation, we solve the steady-state heat conduction equation along with the phase-field kinetic equations of grain growth[63].

The grain growth model parameters are the same as in[63], and the parameters for the steady-state heat conduction calculations are as follows: 1 W/mK for the bulk conductivity, 0.1 W/m.K for the GB conductivity, and 2 nm for the GB width.

During grain growth, to reduce the interfacial energy of the system, the number of grains decreases and the mean grain size increases. As a result, the effective thermal conductivity increases as the process continues. This is captured in Figure. 16 that shows both the microstructure evolution and the change in the thermal conductivity. Again, the results show the effective thermal conductivity

predicted by the new model agrees more closely with FEM than Yang et al. model. For instance, the difference between the results of Yang et al. model and FEM varied from 5% to 6 % across the grain size/evolution time range studied. On the other hand, the difference between the results from our new model and FEM varied only from 0.4 % to 1.3 % across the same range studied.

2.2.6 Derivation of a scaling scheme to accelerate mesoscale phase-field simulations

As we have seen in the previous subsection, one can utilize the phase-field method to track both the evolution of microstructure and thermal conductivity of solids. However, running simulations for microstructures with large grain sizes becomes unfeasible if the physical width of GB is used. Nonetheless, based on the derivations we presented above, one can devise an approach to scale up the numerical value of the interface width without changing the effective conductivity. This can be accomplished as follows. Based on the new Kapitza formula (Eq. 2.29), by assuming constant GB thermal conductivity, the new model (Eq. 2.15) gives the effective conductivity as,

$$k = \frac{(d + l)}{\frac{d}{k_b} + \frac{l}{k_{gb}}} \tag{2.49}$$

Therefore, one can first calculate the effective conductivity based on the actual value of the GB width and its corresponding GB conductivity (for a given value of the Kapitza resistance). Then, we utilize the same relation (Eq. (2.49) to calculate a new scaled value for the GB conductivity that corresponds to the new value of GB width, which we are free to pick for numerical convenience.

As an example for implementing this procedure, We pick the following physical values for the parameters in eq. (2.49): d = 1.25 μm , and l = 1 nm, $k_b and\ k_{gb}$ equal to 4.5 W/m. K, and 0.35 W/m. K, respectively. By substitution of these values into Eq. (2.49), we obtain k =4.45786 W/m. K. We then perform FEM simulation with the same values of the parameters. From the simulation, the effective thermal conductivity was found to be k =4.457862 W/m. K. Now, the same result can be obtained with a much larger GB width and appropriately scaled GB conductivity. By rearranging Eq. (2.49), we obtain

$$k_{gb} = \frac{l}{\frac{(d+l)}{k} - \frac{d}{k_b}} \tag{2.50}$$

Hence, if we choose a GB width of 50 nm instead of 1 nm, Eq. (2.50) can be used to calculate the corresponding GB conductivity that will result in the same effective conductivity. In this specific example, this value is $k_{gb} = 3.612243\ W/m.k$. To validate this approach, the FEM simulation was repeated again with the scaled values of the GB conductivity and width. The results of the FEM simulations are listed in Table 6. As evident from the table, the scaled values give rise to the same effective conductivity calculated based on the original values, and hence it proves the validity of the scaling approach proposed here.

Table 6. Validation of the scaling approach for enabling large scale simulations.

model	Original interface width (nm)	Original interface thermal conductivity. $W/(m.K)$	Scaled interface width (nm)	Scaled interface thermal conductivity. $W/(m.K)$	Effective Thermal conductivity. $W/(m.K)$
FEM	1	0.35	50	3.612243	4.457862

CHAPTER III

AN EXPERIMENTALLY VALIDATED MESOSCALE MODEL OF THERMAL CONDUCTIVITY OF A UO_2 AND BEO COMPOSITE NUCLEAR FUEL[1]

An experimentally validated mesoscale model was developed to simulate the effective thermal conductivity of UO_2–BeO nuclear fuel with different microstructural features. The effects of the second phase (BeO) fraction and morphology, temperature, and interface thermal resistance were investigated. The model predicts that the continuous second phase configuration has a higher effective thermal conductivity than the dispersed second phase configuration for the same volume fraction and temperature. Companion experiments were conducted to validate the model predictions. It was demonstrated that accounting for the interface (Kapitza) thermal resistance is necessary to improve the model predictions. The largest difference between the model calculations and experimental results was about 5%, which is within the precision of the experimental measurements.

3.1 Introduction

The Fukushima Daiichi accident renewed interest in the development of next generation nuclear fuels for current light water reactors. This work models the effective thermal conductivity of a composite uranium dioxide-beryllium oxide (UO_2–BeO) nuclear fuel with applications as a next generation fuel. Previous work on this fuel form has deter- mined the achievable improvement in thermal conductivity associated with an embedded, inter- connected BeO network and investigated FEM modeling of the microstructure.[64, 65] This work uses a joint experimental and modeling approach to quantify the Kapitza resistance between the UO_2 and BeO components and employs the Kaptiza resistance to improve the accuracy of predictions of the thermal conductivity of the composite. Ishimoto first demonstrated the improvement achievable with an embedded, interconnected BeO network within the UO_2 fuel by processing above the eutectic temperature (above 2200°C).[66] The thermal conductivity of the fuel was increased by approximately 60% at

[1] Reprinted with permission from "An Experimentally Validated Mesoscale Model of Thermal Conductivity of a UO_2 and BeO Composite Nuclear Fuel" by FERGANY BADRY, RYAN BRITO, M. GOMAA ABDOELATEF, SEAN MCDEAVITT and KARIM AHMED. 2019. JOM, Copyright [2019] by The Minerals, Metals & Materials Society (JOM).

room temperature with a 4.2 vol.% continuous BeO matrix. In contrast, a dispersed BeO microstructure only increased the thermal conductivity around 10%. [66]At reduced temperatures aligned with current manufacturing procedures, Sarma et al. showed similar improvements could be made by co-sintering UO2 granules coated in BeO at 1700°C.[64] The work compared a green granule and slug bisque manufacturing procedure to fabricate pellets from 5 vol.% to 20 vol.% BeO, both achieving pellet densities > 90% of the theoretical density (%TD). The UO2 was also dis- solved in nitric acid to show the BeO was a mechanically robust, continuous network.[64] Garcia et al. produced UO2-x BeO samples (x = 2.5 vol.%, 5 vol.%, 7.5 vol.%, 10 vol.%) to enable an evaluation of the enhancement achievable by a BeO matrix using samples manufactured from the same source materials and using identical processing parameters. The results indicated that the thermal conductivity of UO2 improved approximately 10% for each 1 vol.% of BeO added.[67] The experimental work of Ishimoto, Sarma, and Garcia provided a detailed experimental development of the fuel design that provides a comparative basis for computational results.

The thermal conductivity of the fuel microstructure has also been modeled using the FEM program ANSYS. Latta et al.[65] validated the model against the results from Ishimoto within the error of the experimental measurement without explicitly accounting for the Kapitza resistance. When applied to the co-sintered microstructure demonstrated by Sarma at 10 vol.%, the model resulted in 9–19% error, varying with temperature. The discrepancy was attributed to poor understanding of the inter- face region of the UO_2 and BeO phases, suggesting further study was needed into the thermal boundary resistance and the thermal conductivity of the components in this application. Nevertheless, the fuel form was modeled in CAMPUS (CityU Advanced Multiphysics Nuclear Fuels Performance with User-defined Simulations) fuel performance code showing the fuel performed consistent with an accident-tolerant fuel.[68]

The previous work demonstrated the feasibility of the development of a UO_2–BeO fuel and began exploring the viability of using computational resources to model the improvement shown experimentally. There is, however, opportunity to improve the modeling of the fuel in complex microstructures, as noted by Latta. [65] This work further explores the relationship of microstructure and thermal conductivity and quantifies the impact of a thermal boundary resistance on the effective thermal conductivity. Experimental results of the thermal conductivity of a dispersed microstructure up to 10 vol.% are reported here, extending the volume fraction

previously studied by Ishimoto from 4.2 vol.%. [66] This work also broadens the volume fractions and microstructures modeled for this material system from a continuous 10 vol.% reported by Latta to multiple volume fractions of both dispersed and continuous microstructures. [65] The Kapitza resistance also has not been explicitly determined previously for this material system. These problems are well suited for the computational techniques employed in MOOSE (Multi- physics Object-Oriented Simulation Environment) developed at Idaho National Laboratory. MOOSE uses the finite-element method (FEM) for solving differential equations corresponding to a variety of physics problems and has several built-in capabilities to generate the microstructures required for this work.[62]

This study seeks to model the effective thermal conductivity of an ATF composite in MOOSE. A uranium dioxide and beryllium oxide composite was selected to provide an experimental comparison of the model results, as described in the background. For the experimental approach, samples with a dispersed BeO microstructure of varying volume fractions were fabricated to provide experimental data for comparison with MOOSE results and to quantify the Kaptiza resistance in this system. The model formulation and implementation in MOOSE consider the effect of dimensionality, methods to generate the distribution of the second phase, and application of the interface thermal (Kapitza) resistance. Various microstructures, concentrations, and distributions of the conductive additive are considered in the results and discussion as well as the impact of a Kaptiza resistance between the two components. This work concluded that the composite thermal conductivity could be well represented using the model introduced here.

3.2 Experimental Approach

3.2.1 Sample Preparation

The experimental approach to fabricating and analyzing the composite uranium dioxide (UO2)-beryllium oxide (BeO) with a continuous BeO network was given by Garcia et al.[67] To produce a dispersed microstructure, the experimental samples were fabricated and analyzed using similar procedures. The uranium dioxide powder was sourced from International Bio-Analytical Industries Inc. and ball-milled on a rotary jar mill. The beryllium oxide powder was sourced from Acro Organics and jet-milled. The desired volume fraction of jet-milled BeO powder was introduced to the ball-milled UO2 powder and mixed. The powder mixture was pre- compacted at

680 MPa and reground in a mortar and pestle. The pre-compacted powder mixture was self-milled prior to final compaction at 230 MPa. The green compacts were sintered on alumina at 1690°C for 18 h under an ultrahigh purity argon atmosphere using a 20 °C/min ramp rate. Samples of 5 and 10 vol.% BeO were fabricated with a dispersed BeO microstructure. Five samples at each volume fraction were produced, but the final thermal property measurements were limited in some cases to three samples because of chipping during sample preparation.

3.2.2 Thermal Analysis

The thermal conductivity of the composite samples was calculated by the equation

$$k = \rho c_p \alpha \qquad (3.1)$$

where k is the thermal conductivity, q is the density, cp is the specific heat, and a is the thermal diffusivity. The bulk densities were determined using the Archimedes immersion method with ethanol as the working fluid. The fraction of theoretical density was computed as the ratio of the bulk density to a volumetric weighted average of the component bulk densities.[69, 70] The specific heat was calculated by a volumetric weighted average of the component-specific heats, which has been shown to be an accurate approximation in this composite system.[67, 69, 70] The thermal diffusivity was experimentally measured by light flash analysis using a NETZSCH LFA 447 NanoFlash instrument. Samples were polished within 0.0005 in parallel, as measured by a micrometer, and coated with a thin layer of graphite. Measurements were collected from 25°C to 300°C at 25°C increments and interpreted using the Cowan model provided by Net- zsch.[71] The experimental samples exhibited varying porosity across samples and concentrations, which influenced the calculation of the composite thermal conductivity. The total porosity across all samples was within the range of 4.9–7.6% with no bias associated with the BeO volume fraction. The average of the total porosity for the 5 and 10 vol.% BeO was 6.0% and 6.8%, respectively. For comparative purposes, the thermal conductivity results at a given volume fraction were corrected to 100% theoretical density using a Maxwell–Garnett correction and averaged.[72, 73]

3.3 Mesoscale model formulation

3.3.1 Thermal Modeling of Composites

To study the effect of a second phase on the effective thermal conductivity, constant temperatures T_r & T_l are applied on the right and left side, respectively. The top and bottom boundaries (y-direction) are taken as adiabatic. Consequently, the thermal gradient points in the x-direction. The dimension of the problem domain is given by L. The heat flux, q, profile in the system is obtained by solving the steady-state conduction equation given by

$$\nabla.(K\,\nabla T) = 0 \qquad (3.2)$$

where k is the thermal conductivity that varies spatially throughout the domain according to the microstructure. Similar to pervious studies [15, 18, 20, 22, 39, 47-51], we utilize a combined phase field and finite-element approach to directly account for the effect of microstructure on the effective thermal conductivity of the composite. In order to distinguish between the matrix, second phase particles, and interfaces, the phase-field variables η_i are assigned such that their values indicate the type of region (e.g., matrix, second phase particle, or interface). The thermal conductivity is then assigned based on these values. Assigning a reduced thermal conductivity values at the interface is equivalent to assuming a specific interfacial thermal (Kapitza) resistance. The details of this procedure for the UO_2-BeO composite are given in Section 3.3 below. Lastly, the overall effective thermal conductivity can be calculated from

$$K_{eff} = \frac{q\,L}{T_l - T_r} \qquad (3.3)$$

where q is the average heat flux, T_r & T_l are the temperatures at right and left boundaries respectively, and L is the width of the simulation domain [15, 18, 20, 22, 39, 47-51].

3.3.2 Effect of Dimensionality on Thermal Conductivity

While 3D calculations are favored to validate realistic models, they are often computationally expensive to perform. Bakker demonstrated the calculated, reduced 2D thermal conductivity can be related to the realistic 3D thermal conductivity (Eqs. 3.4 and 3.5).[74] In certain cases, as shown in Figure. 17, the extra degree of freedom of the flux in the 3D case compared with the 2D case causes the 3D conductivity to be larger than the 2D conductivity, irrespective of whether the conductivity of the dispersed phase is larger or smaller than that of the matrix material.[74]

Nonetheless, this difference can usually be ignored for small volume fractions of the second phase. To demonstrate this, 2D and 3D simulations of a single second phase particle embedded in a matrix representative of the dispersed microstructure were conducted. The matrix and second phase particle thermal conductivities were taken to be the thermal conductivity of UO2 and BeO, respectively. The solutions are presented in Figure. 17. As evident from the figure, the 3D calculated thermal conductivity is higher than the 2D counterpart at all fractions, supporting the conclusions of Bakker. [74] However, Teague et al. [51] found that the 2D calculated thermal conductivity could be higher than its 3D thermal conductivity depending on the microstructure heterogeneities. Thus, the dimensionality factor is applied only to the dispersed microstructure in this work. For the dispersed case, the difference between 3D and 2D thermal conductivities is< 5% for volume fractions< 10 vol.%, as captured in Figure. 17.d. For experimental data obtained at lower volume fractions, 2D simulations are expected to be sufficient. Otherwise, the difference between the 2D and 3D conductivities can be quantified by

$$E_{err} = \frac{K_{3D} - K_{2D}}{K_{3D}} \tag{3.4}$$

Where: E_{err}: the error/fractional difference between 2D and 3D simulations, K_{2D}: thermal conductivity based on 2D simulations, and K_{3D}: real thermal conductivity/ thermal conductivity based on 3D simulations.

Moreover, based on Eq. (4), the real/3D thermal conductivity can be obtained from the reduced 2D calculations through

$$K_{3D} = \frac{K_{2D}}{1 - E_{err}} \tag{3.5}$$

In general, however, the difference will depend on the morphology and distribution of the second-phase particles.

3.3.3 Microstructure Representation

3.3.3.1 Dispersed Microstructure

The dispersed microstructure was obtained by utilizing a single order parameter, g, which takes a value of 1 inside the second phase particle, a value of 0 inside the matrix, and a value between 0 and 1 through the interface region. For the dispersed configuration, the domain size was 500 nm by 500 nm with a particle radius of 12.6 nm for the 5 vol.% case and 17.84 nm for the 10 vol.%

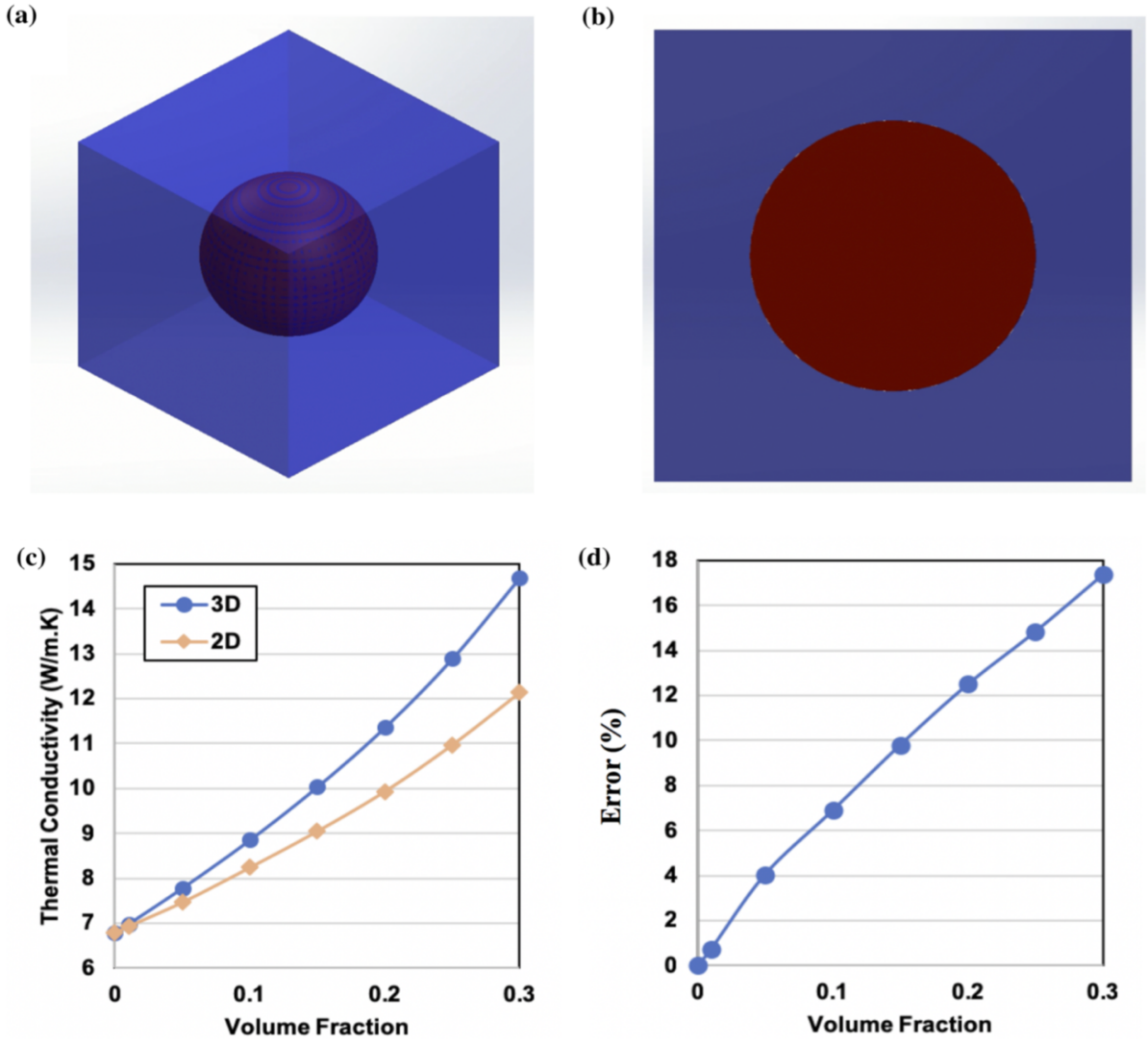

Figure 17. A visual representation of the difference between 3D and 2D thermal conductivities of a two phase material (a and b) at different volume fractions of second phase (shown in red). The particle thermal conductivity is BeO thermal conductivity, and the matrix thermal conductivity is UO_2 thermal conductivity. The calculated effective thermal conductivity values for the 2D and 3D simulations are shown in (c) with the difference/ error between the 2D and 3D simulations presented in (d).

case. For the FEM mesh, a quad element type with a size of 0.25 nm was used. The interface width is taken to be 1 nm.[59, 60] The thermal conductivity was assigned according to

$$K = \begin{cases} K_{UO_2} & if\ \eta = 0 \\ K_{int}(T) = x * K_{UO_2}(T) * \left[\frac{K_{UO_2}(T')}{K_{UO_2}(T)}\right]^3 & \text{if } 0 < \eta < 1 \\ K_{BeO} & if\ \eta = 1 \end{cases} \quad (3.6)$$

Where $K_{UO_2}(T)$: UO_2 bulk thermal conductivity at temperature T, T': Reference temperature taken to be 200 C, $K_{BeO}(T)$: BeO bulk thermal conductivity at temperature T, $K_{int}(T)$: Interface thermal conductivity at T, and x = 0.95: A fitting parameter.

The fitting parameter was determined by fitting the proposed model against the experimental value of the effective thermal conductivity at T = 200°C for the 5 vol.% dispersed microstructures. Heat transport through these materials occurs largely by phonons. The interfaces in the composite act as phonon scattering sites and decrease the thermal conductivity in those regions. [2] In a continuum model, this effect can be accounted for via the incorporation of an interfacial Kapitza resistance.[4, 5] The Kapitza resistance (R_k) is defined as

$$R_k = \frac{\Delta T}{q} \quad (3.7)$$

where ΔT is the temperature drop across the interface between the two phases and q is the average heat flux. Here, the inclusion of the Kapitza resistance is realized by assigning reduced thermal conductivity values across the interfaces of UO_2 and BeO, as demonstrated in Eq. 3.6 and depicted in Figure. 18. Different forms were tried to approximate the interfacial resistance, and Eq. 3.6 proved to give the best results compared with the experimental data. While the specific form for the interface conductivity used here might not be unique, our simulations suggest that any such form must possess two features. First, it should give thermal conductivity values for the interfacial region that is lower than the bulk values of the phases. Second, according to the experimental data, since the thermal conductivities of BeO and UO_2 vary with the temperature, one expects the interface thermal conductivity to be temperature dependent as well. We assume here that it is related to the temperature-dependent bulk thermal conductivity of the low conducting phase.

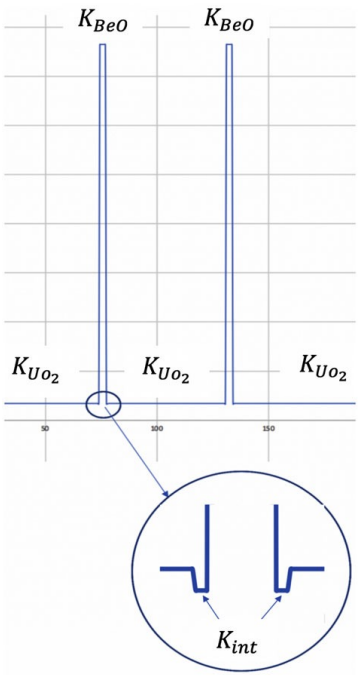

Figure 18. An illustration of the spatial dependence of the thermal conductivity across the interface. The reduced interfacial thermal conductivity approximates the interface (Kapitza) resistance.

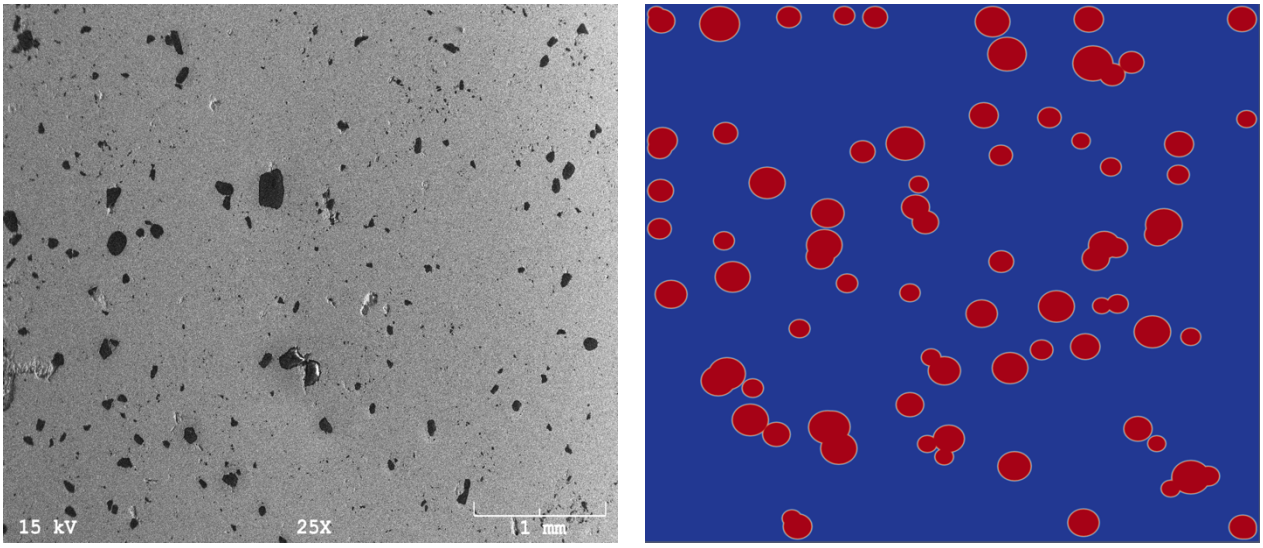

Figure 19. Experimental (left) and simulated (right) images for the dispersed microstructure. In the experimental micrograph, the high conducting phase (BeO) is shown in black and the low conducting phase (UO2) is shown in gray. In the simulation image, BeO is shown in red and UO_2 is shown in blue.

Equation 3.6 satisfies those conditions. Lastly, to compare with experiments, different volume fractions were simulated by changing the radius. An example of a dispersed microstructure is shown in Figure. 19.

3.3.3.2 Continuous Microstructure

The continuous microstructure was obtained by constructing Voronoi diagrams using multiple order parameters, as in the phase-field models of grain growth.[63] In contrast to the dispersed case, the UO_2 is represented as the second phase particles (grains) and the BeO is represented as the matrix (in the sense that it is the continuous phase). An order parameter η_i will take a value 1 inside each grain i (a UO_2 phase particle i) and value 0 elsewhere in the domain. In the matrix (BeO), η_i takes a value between 0 and 1. The domain size for the continuous case was 450 nm by 450 nm with a grain size (UO_2 bulk areas) of 100.6 nm for the 10 vol.% case and 174 nm for the 6 vol.% case. For the FEM mesh, a quad element type was used, sized at 0.25 nm, and based on the literature, the interface width is about 1 nm.[59, 60] An example of the continuous microstructure is shown in Figure. 20. The thermal conductivity is then described as

$$K = \begin{cases} K_{UO_2} & \eta_i = 1 \\ K_{int} = x * K_{UO_2}(T) * \left[\frac{K_{UO_2}(T')}{K_{UO_2}(T)}\right]^3 & 0 \le \eta_i \le 0.1,\ and\ 0.9 \le \eta_i \le 1 \\ K_{BeO} & 0.1 \le \eta_i \le 0.9 \end{cases} \quad (3.8)$$

Note the consistency between Eqs.3.6 and 3.8 in defining the interfacial thermal conductivity with the fitting parameter x also taken to be 0.95. The fitting parameter was determined by fitting the proposed model against the experimental value of the effective thermal conductivity at T = 200°C and volume fraction 6%. The volume fractions of BeO were also varied to compare the model predictions with the experimental results. The different volume fractions were selected by changing the number of dispersed UO_2 particles.

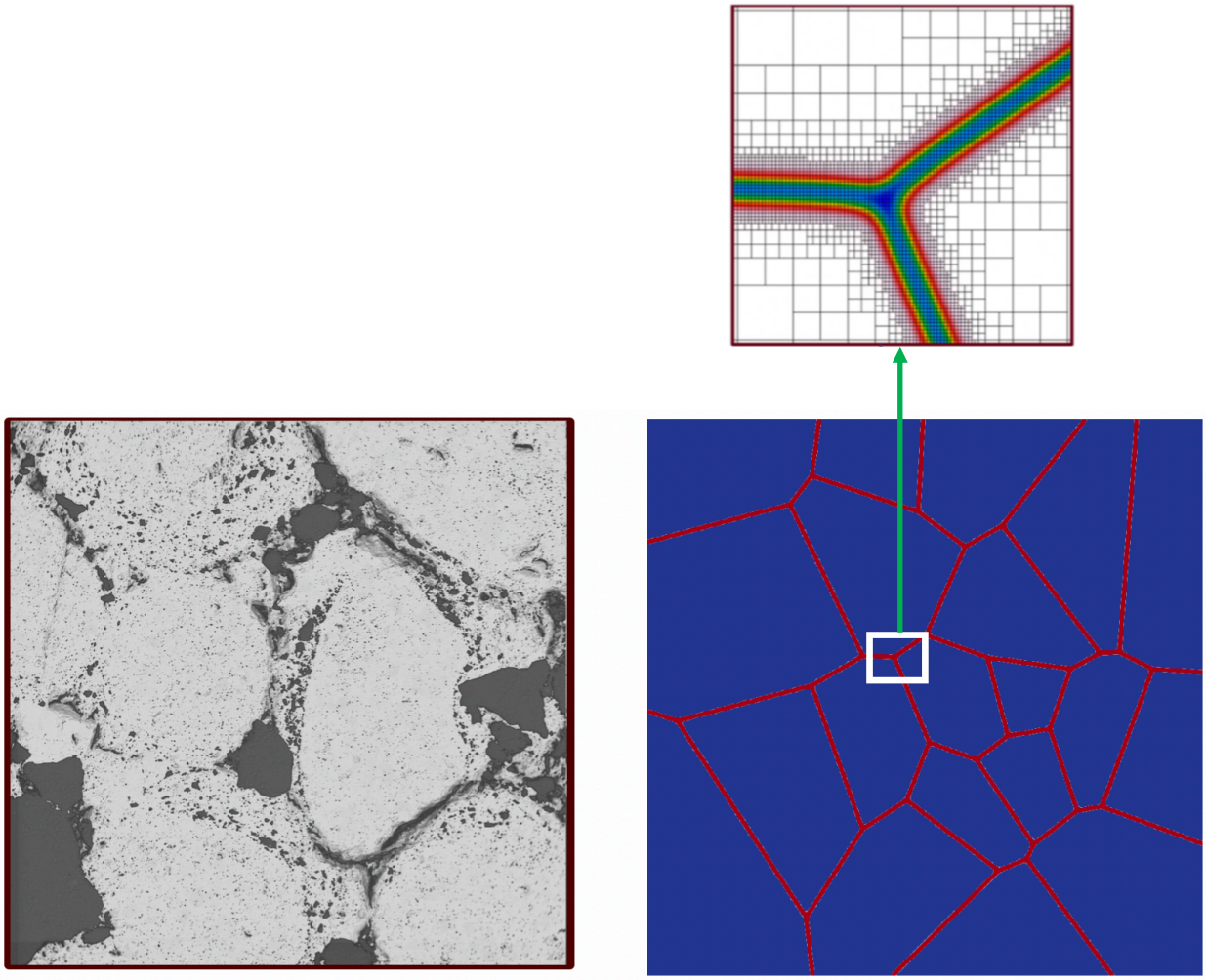

Figure 20. Experimental (left) and simulated (right) images for the continuous microstructure. In the experimental micrograph, the high conducting phase (BeO) is shown in dark gray and the low conducting phase (UO2) is shown in light gray. In the simulation image, BeO appears brown and UO2 is shown in white. In the magnified image, the interface region between the UO2 phase and BeO is shown in red.

3.4 Results and Discussion

The dispersed experimental results presented here and the continuous experimental results from Garcia et al. are shown in Figure 21.[67] For the dispersed case, concentrations of 5 vol.% and 10 vol.% BeO were considered and are shown with the thermal conductivity of UO_2 from the literature, which has been corrected from 95%TD to 100%TD for comparative purposes across all samples.[70] For the dispersed 20 vol.% BeO sample, at temperatures< 100°C, the thermal conductivity of the composite was lower than that of UO_2, a feature inconsistent with the trends

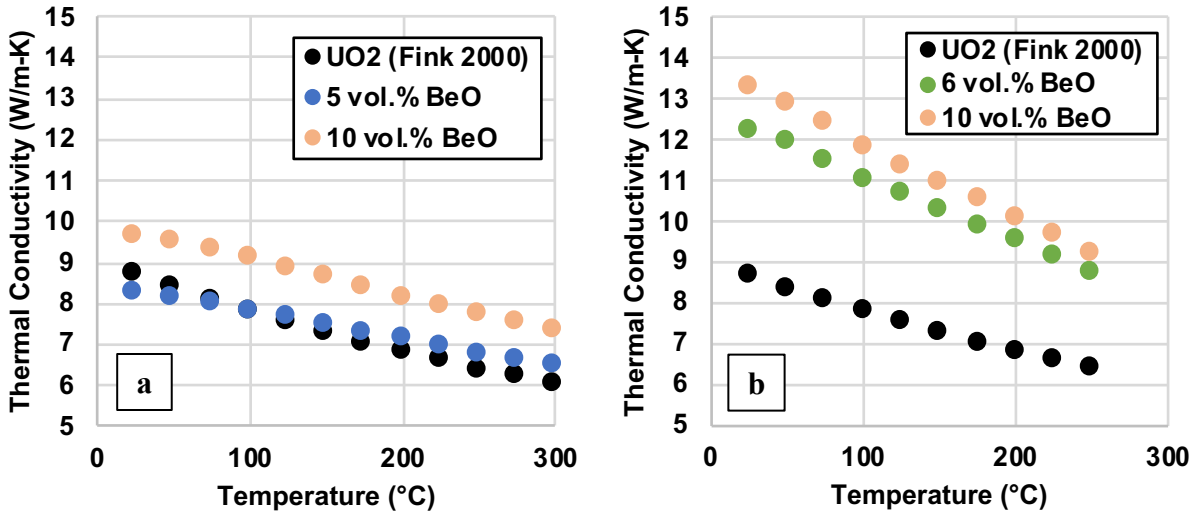

Figure 21. The experimental measurements of the thermal conductivity of UO2-BeO composites of varying concentration with a dispersed (a) microstructure, presented here, and continuous (b) microstructure from Garcia et al. [66].

seen in other samples of this work and in the literature. The deviation in these results compared with the trend impacted later accuracy of the modeled microstructure over this temperature range. For the continuous case from Garcia et al. concentrations of 6 vol.% and 10 vol.% BeO were considered and are shown with the thermal conductivity of UO_2 from the literature.[67, 70] The results highlight the impact of the arrangement of the microstructure on the improvement of the thermal conductivity in the composite. The continuous case shows a much larger enhancement in the composite thermal conductivity compared with the dispersed case.

Previous work by Ishimoto on dispersed UO_2–BeO composites did not exceed 4.2 vol.% of BeO;[66] however, if the linear trend up to 4.2 vol.% is continued up to 10 vol.%, then comparison of this work and Ishimoto's results can be made at 200°C where the two data sets intersect in temperature.[66] The dispersed samples from this study were 13–16% less thermally conductive than the trend shown in the work of Ishimoto.[66] With a similar approach, the continuous microstructure results reported by Garcia et al. can be compared with those reported by Ishimoto.[66, 67] The continuous samples reported by Garcia et al. were 12–17% less thermally conductive than the trend reported in the work of Ishimoto. [66, 67] The similar magnitude and consistent reduction in improvement in the thermal conductivity have been attributed to the difference in the processing temperature from 2200°C to 1600°C for the continuous case and

1800°C to 1690°C for the dispersed case. [66, 67] Additional comparisons of the continuous microstructure with past work are detailed in Garcia et al.[67]

3.4.1 Dispersed Microstructure

The dispersed microstructure was modeled in MOOSE with and without the Kapitza resistance implemented. As described previously (Figure.19), the microstructure was represented in two dimensions as a random dispersion of circular inclusions of BeO. The thermal conductivity takes values of the thermal conductivity of UO_2 in the bulk and of BeO within the inclusions. Without the implementation of the Kaptiza resistance in the boundary region, the thermal conductivity takes values between the two as the order parameter changes. The initial prediction of the thermal conductivity was comparable to earlier attempts to model the composite properties which differed from the experimental results by 9–19%.[65] For the dispersed 5 vol.% case shown in Figure. 22, the difference between the experimental results and MOOSE model varied from 5% to 17% with temperature. Notably, MOOSE over- predicted the effective thermal conductivity by the most at lower temperatures where the experimental sample exhibited thermal conductivity less than that of UO_2. It is suspected that additional experimental work at this concentration may improve the agreement with the MOOSE results. For the dispersed 10 vol.% case, the difference between the experimental results and MOOSE model varied from 3% to 11% with temperature.

When the Kapitza resistance was introduced into the implementation of the thermal conductivity as discussed earlier, the composite thermal conductivity was reduced as expected. As shown in Figure. 22. for the dispersed 5 vol.% BeO case, the reduction in the composite thermal conductivity with the introduction of a Kaptiza resistance was 4–10% across the temperature range studied. For the dispersed 10 vol.% BeO case, the reduction was 6–14% for the same Kapitza resistance.

The reason for the higher reduction compared with the corresponding reduction in 5 vol.% BeO case is the larger surface area of second phase particles in the 10 vol.% BeO case than in the 5 vol.% BeO case, resulting in a larger effect when the Kapitza resistance is implemented. The agreement between the experimental work and MOOSE results improved as demonstrated in Figure. 22. Without the implementation of the Kapitza resistance, the MOOSE results were strictly greater

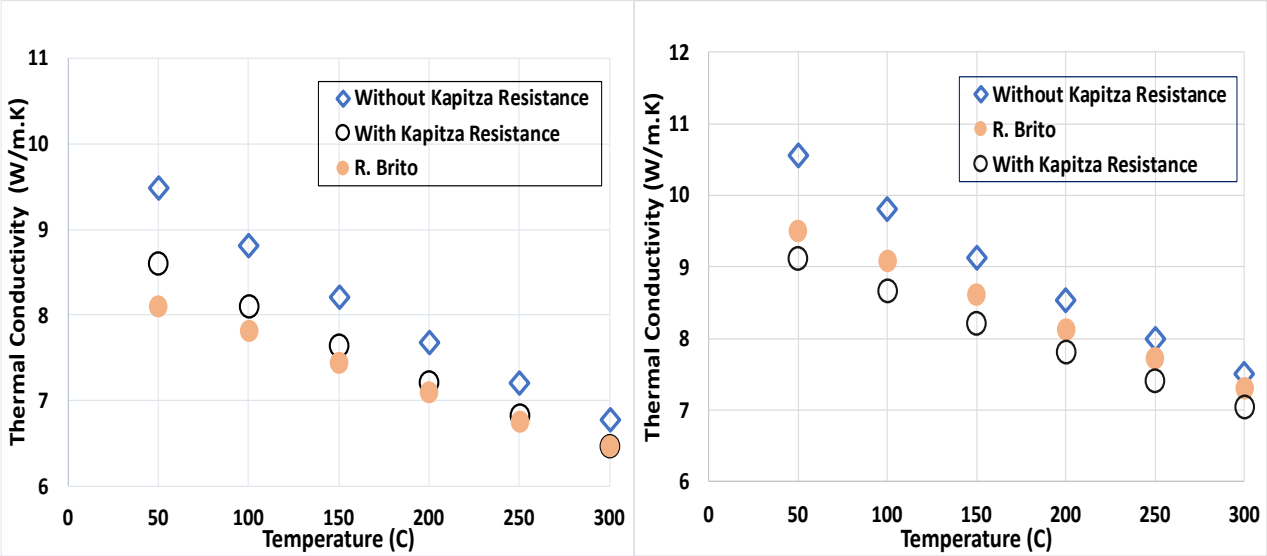

Figure 22. A comparison of the experimental and MOOSE results for 5 vol.% (left) and 10 vol.% (right) composites with a dispersed microstrcture. Accounting for the interface resistance improved the model predictions.

than the experimental results, and the Kapitza resistance strictly reduced the effective thermal conductivity, making the improved agreement unsurprising.

As there are no published thermal resistance values for BeO–UO_2 interfaces, this work presents new data for the value of the Kapitza resistance across these interfaces. The Kapitza resistance value was calculated from Eq.3.7 at T` = 200°C to be 1:55 × 10^{-10} m^2 K/W. Accounting for the Kapitza resistance, the differences between the model pre- dictions and experimental results were reduced appreciably. For the dispersed 5 vol.% BeO case, the agreement was improved from a 5–17% difference to a 0.2–6% difference across the temperature range where the maximum difference was at the lowest temperature modeled (50°C) and the error decreased as temperature increased until reaching its minimum at the highest temperate (300°C). Again, at low temperatures the experimental

samples exhibited uniquely low thermal conductivity values, so the agreement may be improved with additional experimental work. For the dispersed 10 vol.% BeO case, the agreement was improved from a 3–11% difference to 3.5–4% difference across the temperature range. Again, the maximum error occurred at the lowest temperature (50°C) and the minimum occurred at the highest temperature (300°C).

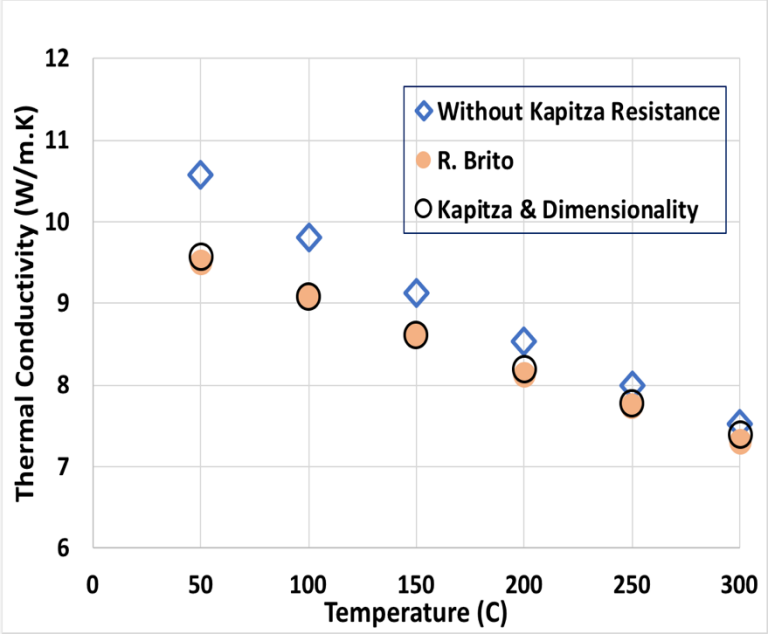

Figure 23. A comparison of the experimental and MOOSE results for 10 vol.% composites. The agreement improves when we consider the interface (Kapitza) resistance and the dimensionality factor.

It is noteworthy to mention that the simulation results for 10 vol.% are lower than the experimental results across the temperature range. This has been attributed to the dimensionality effect that increases with the volume fraction of second phase (Figure. 17). If we consider the effect of dimensionality (converting a 2D thermal conductivity to a 3D thermal conductivity), we see improved agreement between the experimental and MOOSE results, e.g., only a difference of 0.6–1% across the temperature range as seen in Figure. 23. Thus, converting from a 2D thermal conductivity to a 3D thermal conductivity makes the comparison more consistent.

3.4.2 Continuous Microstructure

As evident from the results for the dispersed case, accounting for the Kapitza resistance is necessary to improve the model predictions. The continuous microstructure was represented in MOOSE as described earlier. As can be inferred from Eq. 3.8 and Figure. 20, the thermal conductivity takes values of the thermal conductivity of UO2 in the grains and of BeO at the spaces between those grains, with a reduced value at the interfaces. The Kapitza resistance value, determined from Eq. 3.7, was similar to the dispersed microstructure case. As Figure. 24 shows, accounting for the Kapitza resistance, the differences between the model predictions and experimental results were

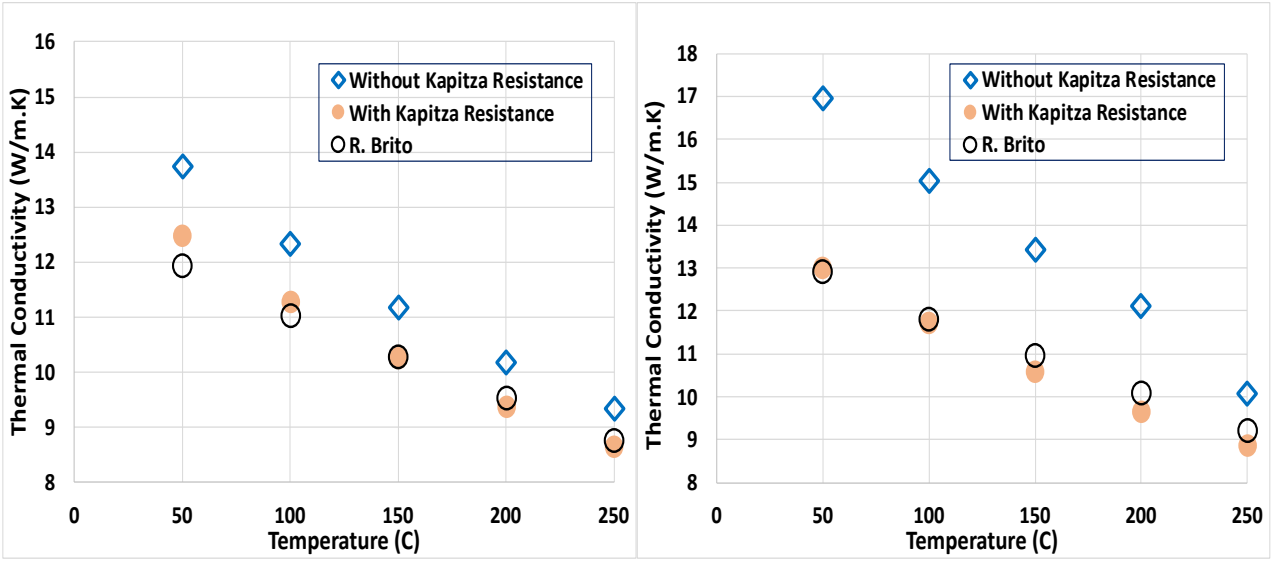

Figure 24. Comparisons between the model predictions and the experimental results from Garcia et al. for 6 vol.% (left) and 10 vol.%. (right) composites with a continuous microstructure [66]. The interface thermal resistance was considered in the simulations.

reduced significantly. For the continuous 6 vol.% BeO case, the agreement was improved from a 6.75–15% difference to a 1.3– 4.5% difference for the range of temperature con- sidered with the maximum difference at the lowest temperature modeled (50°C). For the continuous 10 vol.% BeO case, the agreement was improved from a 9–31% difference to 0.5–4% difference for the range of temperature considered. It is clear that the Kapitza resistance has a larger impact on the continuous 10 vol.% BeO case than on the continu- ous 6 vol.% BeO case because as the volume fraction of the second phase increases, the interface region's surface increases. Similar to the dispersed case, those differences are within the accuracy of the experimental measurements.

CHAPTER IV

AN EXPERIMENTAL VALIDATED MESOSCALE MODEL OF THE EFFECTIVE THERMAL CONDUCTIVITY OF U-ZR METALLIC NUCLEAR FUEL

Two 3D experimentally validated mesoscale models are developed to simulate the effective thermal conductivity of U and U–Zr nuclear fuel with different microstructural features. The effects of the second phase fraction, temperature, and interface thermal resistance are investigated. Companion experiments were conducted to validate the model predictions. It was demonstrated that accounting for the interface (Kapitza) thermal resistance and Zr precipitation phenomenon are necessary to improve the model predictions. The largest difference between the model calculations and experimental results was about 4.5%, which is within the precision of the experimental measurements.

4.1 Introduction

Uranium-Zirconium (U-Zr) fuels are the main candidate fuels for fast reactors [75-78]. One of the pronounced challenge for this type of fuel is swelling phenomena [79].To mitigate this challenge, manufacturing the fuel with a high initial porosity is preferable [75]. This could have a significant effect on the effective thermal conductivity due to fact that porosity particles have a thermal conductivity with few orders of magnitude less than that of U-Zr. At the same time, thermal conductivity is an important physical property for any nuclear reactor not only because its direct effects on the reactor's operation, efficiency, and safety, but also due to its significant and direct effects on the fuel microstructure evolution. For instance, both Zr content redistribution and Lanthanides transport phenomenon are affected by the temperature gradients [76, 80, 81]. Thus, assessment and studying the effect of high initial porosity and heterogeneity microstructure on the effective thermal conductivity of U-Zr is needed. This is a crucial step to develop a new fuel with an initial microstructure that yield a higher fuel performance.

A many of analytical expressions and empirical formulas have been developed to estimate and study the effects of microstructural inhomogeneity[82]. The first and most basic model was derived by Maxwell[83]. Based on effective medium approximations (EMA), Maxwell has

developed an expression of effective thermal conductivity for a continuous matrix with dispersed particles with uniform shape (spherical /circular). The effect of particle size, interaction between the dispersed particles, and generated interfacial thermal resistance between the second phase particles and the matrix were ignored. So, many models were developed later to include the effects that were ignored. For instance, Hasselman and Johnson have modified the Maxwell model in order to include the Kapitza effect, and frequently the inclusion size was included also[84]. Other models were developed analytically based on one directional heat flux assumption for system with spherical and cubic particles[85-87]. Moreover, the Maxwell model was generalized by Bauer[88] to consider the distributions with multiple pore shapes, sizes. Despite all of the previous efforts, still there are some realistic features missing such as the interaction between the particles or the agglomeration effect.

As a result of shortage abilities of the analytical models, many of numerical methods approaches were proposed to study the impact of microstructure heterogeneities on the effective thermal conductivity. For instance, a mesoscale model was developed to study the effect of grain size and porosity fraction variation on the effective thermal conductivity in polycrystalline microstructure [20, 22]. A finite element method (FEM) to study the effect of intergranular fission gas bubbles on the effective thermal conductivity in a polycrystalline material was proposed by P. C. Millett and M. Tonks [18]. Another further step was took by studying the effect of lenticular intergranular gas bubbles on grain boundary Kapitza resistance in a bi-crystal [89]. This work was developed later for the effective Kapitza resistance of UO2 grain boundaries and based on 3D simulation [19]. By coupling of mesoscale modeling approaches with the conducted experimental work, Teague et al. [51] have evaluated the effect of microstructure components such as precipitates, pores, and fission product layer on effective thermal conductivity of high burn-up oxide fuel. Moreover, Hu et al. [16] used phase filed model to construct three dimensional structures with realistic features of irradiated U–Mo metallic fuels to assess various microstructural features such as grain size, inter- and intra- granular gas bubbles on the effective thermal conductivity. Similar work was done later [90] but for U-7Mo and based on two dimensional structures.

In general, few researchers conduct modeling and simulation of microstructural inhomogeneity on the effective thermal conductivity of U-Zr. For mesoscale simulations, one of the most important

work was done by Di Yun et al. [91] The author has focused on the effect of porosity on the effective thermal conductivity and temperature distribution of U-Zr. This work considered different shapes of porosity particles, such as spheres and discs. Moreover, this work assigned pores with different sizes based different zones (outer, middle, or inner zones). In order to consider the random orientations effect, the thin disc pores in three different orientations respect to the radial direction of the thermal gradient were considered. Despite that, this work considered only the uniform arrangement of those particles in each zone. By other words, the interaction between the particles and the agglomeration effect was not considered. Additionally, the interfacial thermal resistance that take a significant place between the fuel components was not included by any of the aforementioned studies.

Here we develop and implement two quantitative mesoscale models for the effective thermal conductivity of depleted uranium (Dep_U) and uranium zirconium (U-Zr). These models account for the effects of temperature, underlying microstructure, and interface thermal resistance for calculating the effective thermal conductivity. Additionally, this work uses a joint experimental and modeling approach to quantify the Kapitza resistance between the fuel components and utilize it to improve the accuracy of predictions of the thermal conductivity of the Dep-U and U-10Zr. Companion experiments were conducted to validate the model predictions. It was demonstrated that accounting for the interface (Kapitza) thermal resistance and Zr precipitation phenomenon are necessary to improve the model predictions. The largest difference between the model calculations and experimental results was about 4.5%, which is within the precision of the experimental measurements.

4.2 Materials and Methods

The detailed description of sample preparation and thermal property determination in [75]. Samples were prepared inside an inert atmosphere glove box due to the pyrophoricity of the metal powders. The uranium powder was obtained by hydride de-hydride of depleted uranium metal. The metal was heated to 225°C under a argon 5% hydrogen cover gas to convert to the hydride form. This was followed by heating to 325°C and placed under vacuum to return the hydride to uranium metal. To prepare alloys the uranium was mixed with zirconium powder by tumbling for 1-2 hours. The powders were pressed in steel dies at 67 MPa, 168 MPa, and 503 MPa held for 1

minute. The green pellets were sintered in vanadium crucibles held in alumina boats under a UHP argon cover gas. Temperatures from 850°C to 1100°C, and sintering times from one to twenty-four hours were varied to obtain various densities.

Thermal diffusivity measurements from 20°C to 300°C were carried out with a Netzsch Light Flash Analyzer (LFA) Model 447. While in the glove box samples were coated with graphite lubricant then placed in a sealed custom-built holder with sapphire windows. The LFA is not inside a glove box, so the holder was necessary to prevent oxidation of the samples during the measurements.

The thermal diffusivity (α) was combined with the specific heat capacity (C_p) and density (ρ) to obtain the thermal conductivity (κ) according to the following:

$$\kappa = \alpha \cdot C_p \cdot \rho \tag{4.1}$$

The molar heat capacity for α-uranium was estimated by equation [92]:

$$C_{n\alpha U} = 24.959 + 2.132\ X\ 10^{-3}T + 2.370\ X\ 10^{-5}T^2\ (203 \leq T \leq 873\ K) \tag{4.2}$$

The molar heat capacity of U10Zr was estimated with equation [92]:

$$C_{nU10Zr} = 1.359 + 0.05812T + 1.086\ X\ 10^{6}/T^2\ (203 \leq T \leq 873\ K) \tag{4.3}$$

Where the molar heat capacity was in J/mol·K and the temperature in K. The values for U5Zr were linearly interpolated between uranium and U10Zr.

The sintered depleted uranium and zirconium-uranium alloy samples were mounted in epoxy for sectioning, polishing, and imaging in scanning electron microscope. Samples were coated in carbon and loaded in a JEOL JSM-6400 at 10-20 KeV with a working distance of 15mm for imaging. Densities were determined by geometric measurement and the immersion method with ethanol as the working fluid.

4.3 Mesoscale model Formulation

4.3.1 Thermal model

A computational approach that combine finite-element and phase-field methods is utilized. In such approach, constant temperatures T_r & T_l are applied on the right and left side (x direction), respectively. The other four boundaries (y and z directions) are taken as adiabatic. Consequently, the thermal gradient points in the x-direction. This 3D configuration is shown in Figure. 25. The heat flux, q, profile in the system is obtained by solving the steady-state conduction equation, e.g.,

$$\nabla.(K\,\nabla T) = 0 \tag{4.4}$$

where k is the thermal conductivity, which varies spatially throughout the domain to account for the underlying microstructure, as will be demonstrated in the next subsection (4.3.2).

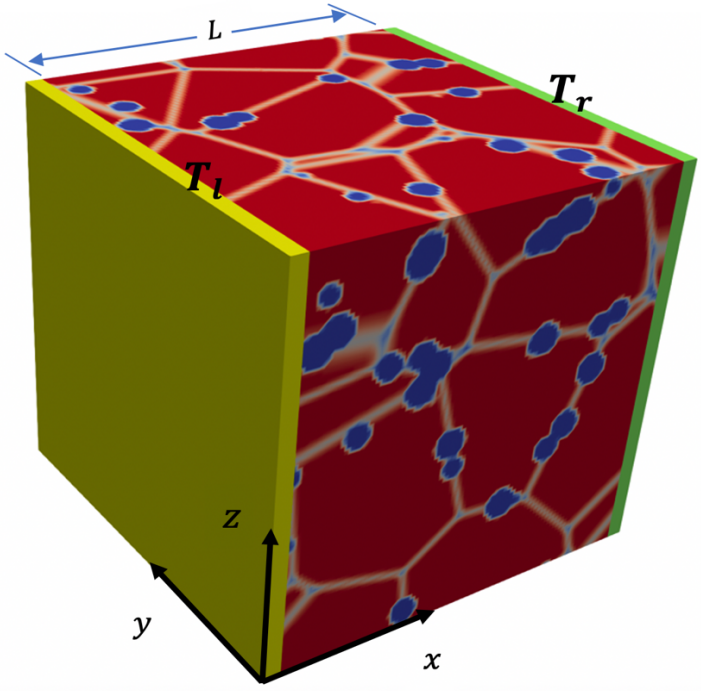

Figure 25. A configuration of three dimensional (3D) thermal modeling approach.

Then, the overall effective thermal conductivity can be obtained from

$$K_{eff} = \frac{q\,L}{T_r - T_l} \tag{4.5}$$

where q is the average heat flux, T_r & T_l are the temperatures at right and left boundaries respectively, and L is the width of the simulation domain (see Figure. 25). [15, 18, 20, 22, 39, 43, 47-51, 93].

where the heat transports through materials by phonons and electrons movement. The interfaces in the composite act as energy carriers scattering sites and decrease the thermal conductivity in those regions[2, 4, 5]. The Kapitza resistance (R_k) is defined as

$$R_k = \frac{\Delta T}{q} \tag{4.6}$$

where ΔT is the temperature drop through the interface between the two phases and q is the average heat flux.

Besides, the effective thermal conductivity is also calculated also based on Maxwell approximation[94].

$$\frac{K_{eff} - K_m}{K_{eff} + (d-1)K_m} = V_{2p}\left[\frac{K_{2p} - K_m}{K_{2p} + (d-1)K_m}\right] \tag{4.7}$$

Where $K_m =$ is matrix thermal conductivity, K_{2p}= second phase thermal conductivity, V_{2p} is the volume fraction of the second phase and d = dimensionality factor = 3 for 3D configurations.

4.3.2 Microstructure Representation

The phase-field method is used to represent the microstructure. The dispersed microstructure is obtained by utilizing order parameters which take a value of 1 inside the second phase particle, a value of 0 inside the matrix, and a value between 0 and 1 through the interface region. For the simulated 3D configuration, the domain size was 512 nm* 512 nm *512 nm with non-uniform inclusions sizes vary from 10 to 80 nm. Those particles were let to relax for few time steps[52-55]. For the FEM mesh, a hexagonal element type with a size of 2 nm was used. The interface width is taken to be 3 nm and two levels of adaptivity are implemented through this region to reduce the element size to 0.5 nm to accurately representing the interfacial thermal resistance.

4.3.2.1 Microstructure of depleted uranium (Dep_U)

The Dep_U microstructure is obtained by utilizing a phase filed model by utilizing a single order parameter (see Figure. 26-right). In this model, the phase-field variable η is assigned such that its values indicate the type of region (pores, pore interface or bulk fuel). The thermal conductivity is then assigned based on these values according to Eq.4.8. An empirical model is developed for argon thermal conductivity against temperature (see Figure. 27-left) [95].

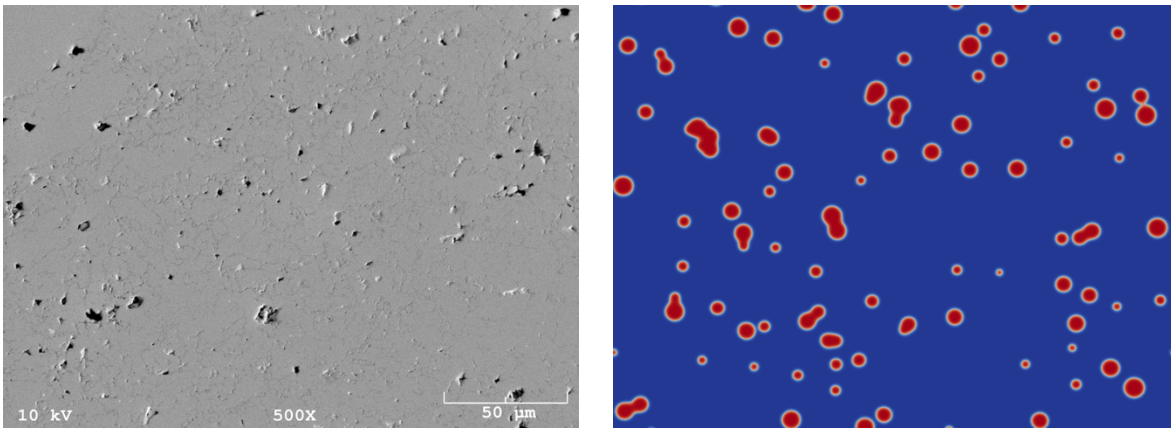

Figure 26. BSE of Dep_U (left) sample. The light gray corresponds to uranium and black to pores. Simulated (right) image for Dep_U microstructure. pores are shown in red and Dep_U is shown in blue.

Kim model is used to predict the thermal conductivity of fuel matrix component (see Figure. 27-right). An empirical model is developed for the interface conductivity, this model is fitted against the experimental data to determine the fitting parameter x. Moreover, according to the experimental data, since the thermal conductivities of matrix and porosity particles vary with the temperature, one expects the interface thermal conductivity to be temperature dependent as well. We assumed here that it is related to the temperature-dependent bulk thermal conductivities of the Dep_U and argon (Ar) pores, as demonstrated in Eq. (4.8).

Hence, the thermal conductivity is assigned according to

$$K(T,\eta) = \begin{cases} K_U(T). & \eta = 0 \\ K_{int}(T) = x\left(\frac{k(T)_U - k(T)_{Ar}}{2} + k(T)_{Ar}\right)\left(\frac{k(T)_U * k(T)_{Ar}}{k(T')_U * k(T')_{Ar}}\right)^3 & 0 < \eta < 1 \\ K_{\mathrm{Ar}}(T). & \eta = 1 \end{cases} \quad (4.8)$$

Where $K_U(T)$ is Dep_U bulk thermal conductivity at temperature T, $K_{\mathrm{Ar}}(T)$: Ar bulk thermal conductivity at temperature T, and $K_{int}(T)$: Interface thermal conductivity at T. T' is the reference temperature $= 290$ ℃, T_{max} is the maximum temperature $= 300$ ℃, T_{min} is the minimum temperature T= 40 ℃ and the fitting parameter x =0.15. This fitting parameter is determined by fitting the proposed empirical model against the experimental values of the effective thermal conductivity with the theoretical density 82.5%.

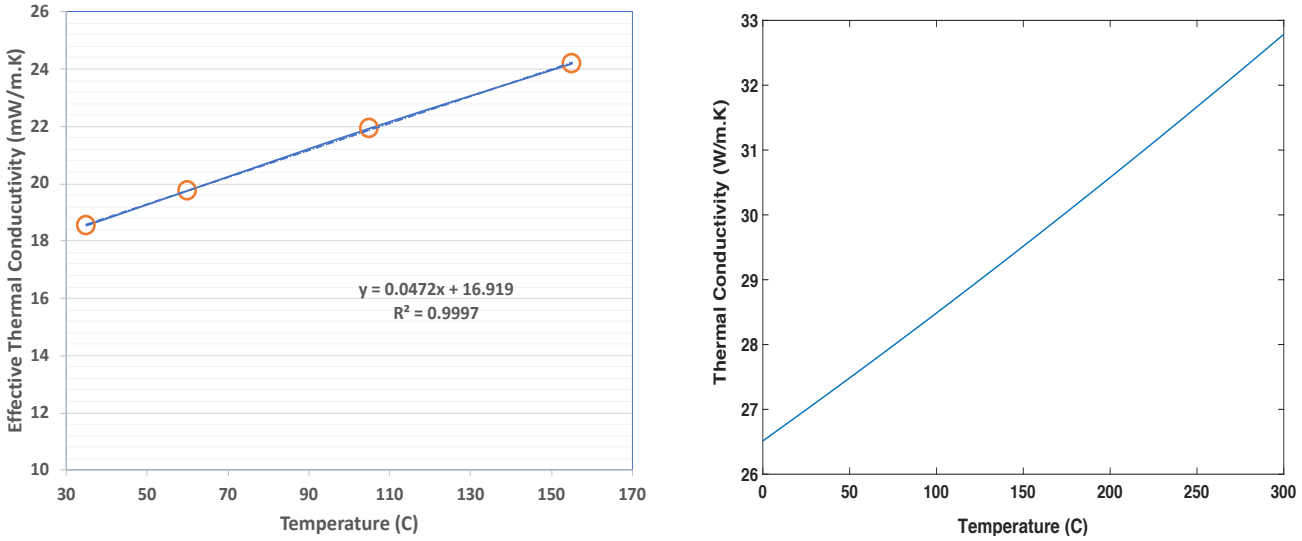

Figure 27. The effective thermal conductivity of argon gas (left), and the effective thermal conductivity of depleted uranium (right)-based on Kim model.

4.3.2.2 Microstructure U-10Zr

By reviewing the BSE images of U-10Zr that showed in Fig 27-left, we found clearly that there is a third phase show up. So, the new phase is created due to Zr precipitation phenomenon. Based on the conservation of mass, creation the Zr precipitates lead to decrease the Zr wt% in the fuel matrix. Two main assumption were made, first, the composition of Zr precipitates are assumed as 100% Zr. Second, the Zr content will be reduced from 10% wt to 9% wt of Zr due to the precipitation phenomenon, and that content is uniformly distributed through the fuel matrix. Based on that, the total volume and the volume fractions of precipitates are calculated for all various theoretical densities by using Eqs. 4.9 and 4.10, respectively (see appendix A1), and presented in Table 7.

$$V_{Pr} = \left(\frac{M_{Zr}}{M}\right)\left(\frac{\rho}{\rho_{Zr}}\right) V\, \rho_{TD}(\gamma_{zr} - \gamma_{Zr}^{m}) \tag{4.9}$$

Then, the volume fraction of the precipitates can obtain by

$$\frac{V_{Pr}}{V} = \left(\frac{M_{Zr}}{M}\right)\left(\frac{\rho}{\rho_{Zr}}\right) \rho_{TD}(\gamma_{zr} - \gamma_{Zr}^{m}) \tag{4.10}$$

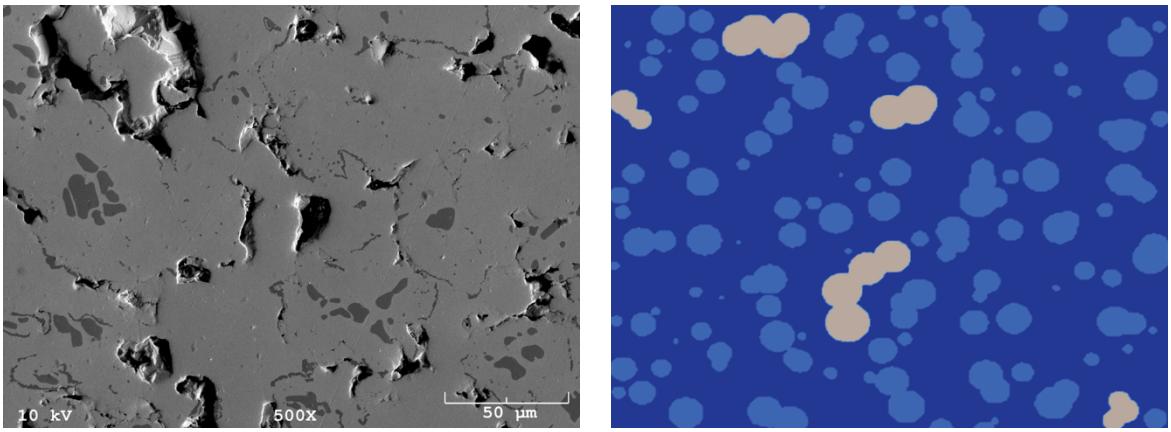

Figure 28. BSE of U-10Zr (left) sample. The light gray corresponds to U-10Zr, dark gray to zirconium and black to pores. Simulated (right) image for U-10Zr microstructure. pores are shown in light blue, Zr precipitates are shown in peach, and U-10Zr is shown in blue.

Similar to the pervious case, the U-Zr microstructure is obtained by utilizing the phase-field model. But due to fact that this microstructure includes more than two phases, two order parameters are assigned (see Figure. 28-right). phase-field variables η_i are assigned such that their values indicate the type of region (bulk U-Zr fuel, pores, pore interface or Zr-precipitates).

Again, the thermal conductivity is then assigned based the indicated region. Kim model was used to produce the input data of thermal conductivity of U-Zr fuel matrix component (see Figure. 29).

Table 7. Total precipitates volume and volume fractions.

Theoretical density (%)	Total precipitates volume(nm^3)	Precipitates volume fra (%)
73.8	2.17×10^6	1.62
76.1	2.24×10^6	1.67
80.9	2.38×10^6	1.77
83.8	2.46×10^6	1.84

*The precipitates volume fractions were calculated respect to the total volume of the domain (512 nm×512nm×512nm).

An empirical model is developed for the interface conductivity, this model is fitted against the experimental data to determine the fitting parameter x. thus, the thermal conductivity is assigned according to

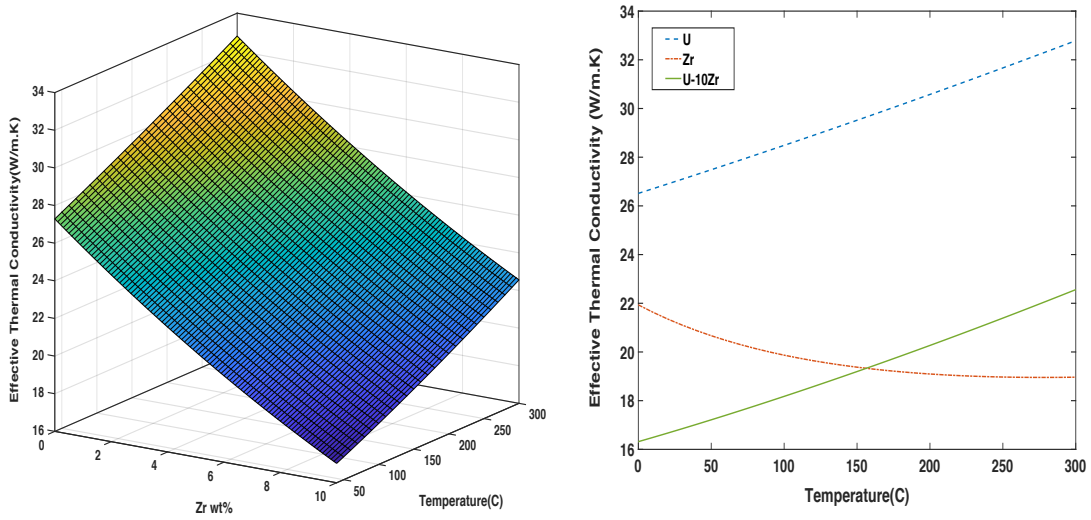

Figure 29. 3D configuration of the effective thermal conductivity of U-Zr (left) as function in temperature and zirconium weigh percent. 2D configuration of the effective thermal conductivity of depleted uranium, uranium zirconium and zirconium (right)-based on Kim model.

$$K(T,\eta_1,\eta_2)=\begin{cases} K_{U-Zr} & \eta_1+\eta_2=0 \\ K_{Ar} & \eta_1=1,\eta_2=0 \\ K_{int}(T)=\left(\dfrac{k(T)_{U-Zr}-k(T)_{Ar}}{2}+k(T)_{Ar}\right)\left(1+x\dfrac{T-T'}{T_{max}-T_{min}}\right)^2 & 0<\eta_1<1,\eta_2=0 \\ K_{Zr} & 0\le\eta_1\le 1,\eta_2=1 \end{cases} \tag{4.11}$$

Where K_{U-Zr} is U-Zr bulk thermal conductivity at temperature T, K_{Zr} is Zr bulk thermal conductivity at temperature T, T' is the reference temperature $= 120$ ℃, T_{max} is the maximum temperature $= 300$ ℃, T_{min} is the minimum temperature $= 40$ ℃, and the fitting parameter $x =$ 1.18. This fitting parameter was determined by fitting the proposed empirical model against the experimental values of the effective thermal conductivity with the theoretical density 76.1%.

4.4 Results and Discussion

The depleted uranium (Dep_U) and uranium zirconium (U-Zr) results are presented here through this section. All the simulations are conducted in 3D to be appropriate for validation and comparison with the conducted experimental data. As described previously (Figures 26 and 28), the microstructure is represented as random dispersion of non-uniform shape inclusions of second phase (Ar). The dispersed microstructure is modeled in MOOSE with and without with the Kapitza resistance implemented. For the Dep_U case, theoretical densities of 78.3%, 82.5%,86.9% and 88.6% are considered and shown with the thermal conductivity of depleted uranium that conducted

experimentally. For the U-Zr case, theoretical densities of 73.8%, 76.1%, 80.9%, and 83.8% are considered and plotted with the experimental values of thermal conductivity of U-Zr. The results highlight the impact of the implementing of interface thermal conductivity between the fuel components and considering the Zr precipitation phenomenon on the improvement the thermal conductivity prediction in the nuclear fuel.

4.4.1 Mesoscale model of depleted uranium

This subsection presents the predictions of the developed mesoscale and the Maxwell models against the experimental data of the effective thermal conductivity of Dep_U. Figure. 30 shows the predicted and the measured effective thermal conductivity versus temperature for various theoretical densities of Dep_U. As obvious from the figure, the effective thermal conductivity increases with the increase of temperature for the experimental and the continuum models with almost linear trend.

MOOSE has the ability to consider effect of many microstructure features such as particles size, shape and distribution. Some of these features has a positive effect on the effective thermal conductivity. For instance, reducing the inclusion size or increasing the curvature could motivate the heat diffusion and that render the MOOSE results are slightly higher than those produced by Maxwell model.

The initial predictions of MOOSE (without implementing the Kapitza resistance) and Maxwell are higher than the experimental results and that due to fact that is implementing an interfacial thermal resistance between the fuel components reduces the effective thermal conductivity value. For the theoretical densities 78.3%, 82.5%, 86.9%, and 88.6% cases shown in Figure. 30, the difference between the experimental and MOOSE results varied from 22.5-26%, 18.6-25.4%, 9.5-15.6%, and 9.4-14.3% with temperature, respectively.

When the Kapitza resistance is introduced into the implementation of the thermal conductivity as discussed earlier, the effective thermal conductivity was reduced as expected. As shown in Figure. 30 for theoretical densities 78.3%, 82.5%, 86.9%, and 88.6% cases, the reductions in the overall thermal conductivity with the introduction of the Kapitza resistance are 17.9-20.6%, 15.7-17.8%, 13-14.5%, and 11.3-12.8% across the temperature range studied, respectively.

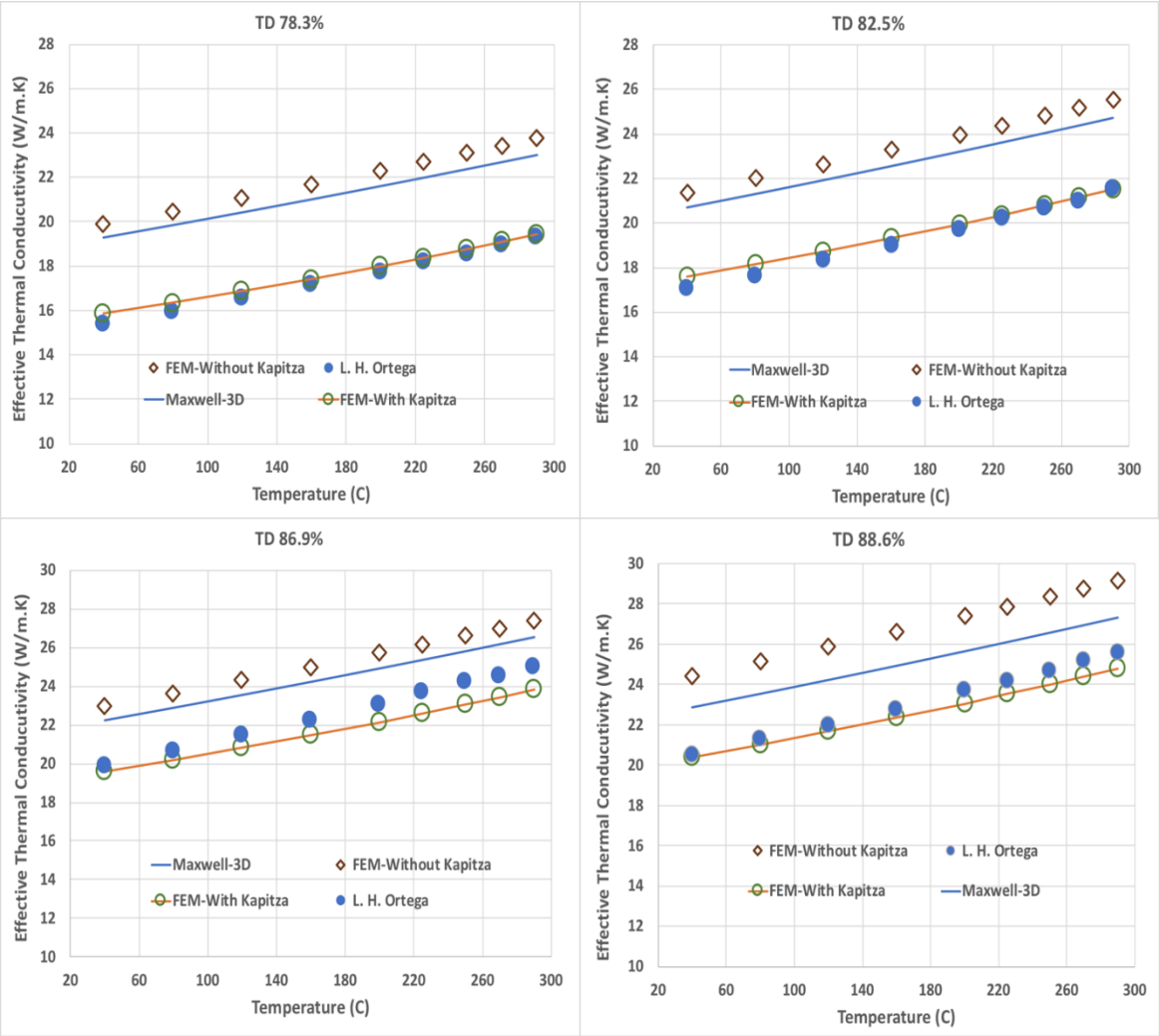

Figure 30. Effective Kapitza resistance versus temperature for various theoretical densities of depleted uranium.

Notably, the reduction in the overall thermal conductivity due to Kapitza effect decreases as the theoretical density of the fuel increases. The reason behind that is increasing the theoretical density lead to decreasing the surface area of second phase particles, resulting in a smaller effect when the Kapitza resistance is implemented. The agreement between FEM and the experimental work results is improved as showed in Figure. 30. Without the implementation of the Kapitza effect, the FEM results were sternly greater than the experimental results, and the Kapitza resistance appreciably reduces the effective thermal conductivity, making the improved agreement unsurprising. For theoretical densities 78.3%, 82.5%, 86.9%, and 88.6% cases, the agreement is

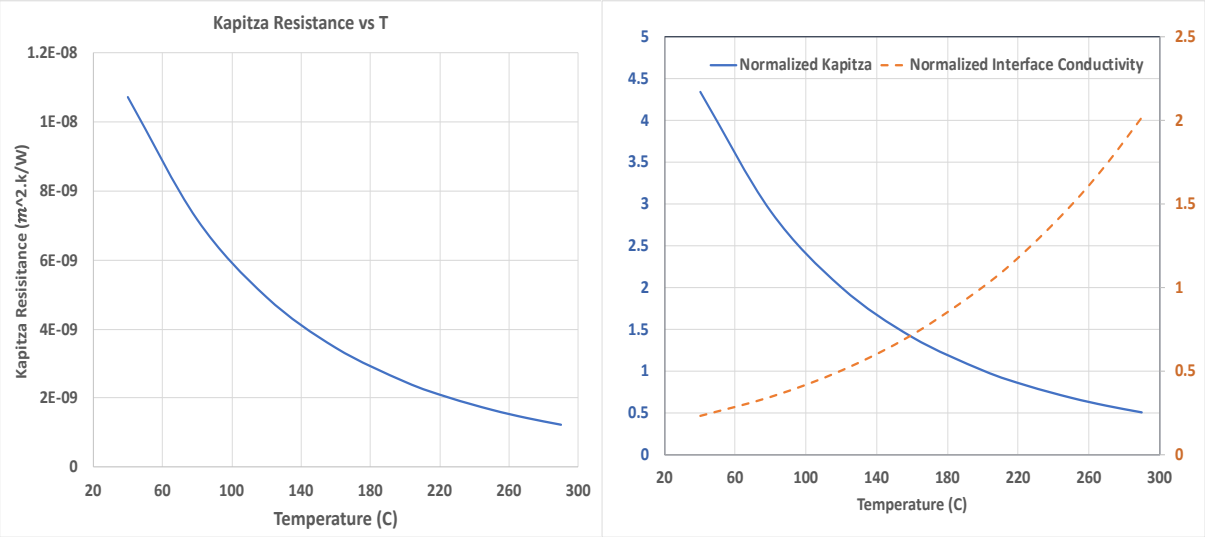

Figure 31. The effective Kapitza resistance (left) and the normalized interface thermal conductivity and the normalized effective Kapitza resistance (right) versus temperature of depleted uranium/Argon interface.

improved from 22.5-26%, 18.6-25.4%, 9.5-15.6%, and 9.4-14.3% difference to 0.7-2.9%, 0-3.1%, 1.3-4.2%, and 0.3-2.9% difference across the temperature range studied, respectively.

Figure.31. (left) shows the behavior of Kapitza resistance against temperature based on Eq. 4.6 and the developed empirical model of the interface thermal conductivity (Eq. 4.8). The Kapitza resistance between the fuel matrix and second phase particles decreases as temperature increases and that due fact that both bulk thermal conductivities increase with temperature and the interface thermal conductivity as we mentioned above should be related to the thermal conductivity of one or two sides that surrounded the interface.

Figure.31. (right) presents the trend of normalized Kapitza resistance and interface thermal conductivity versus a temperature. As obvious from the figure, the interface thermal conductivity increased few times when the temperature increased from 40 ℃ to 290 ℃. This is almost matching with the literature[30]. Where in [30] the interface thermal conductivity increased three times but here increased around four times and we think that might due to that the interface here is gas-solid not solid-solid like in [30]. Since the gas atoms are more sensitive to the temperature, so the atom configuration through the interface is changing significantly with increasing the temperature. Moreover, the interface thermal conductivity is sensitive to the atom structure inside GB[30-35], by generalizing this fact here to be for any interface that could explain the reason behind increasing the interface thermal conductivity few times.

4.4.2 Mesoscale model of U-10Zr

This subsection presents the predictions of the developed mesoscale and the Maxwell models of the effective thermal conductivity of U-10Zr. Figure 32 shows the predictions of the Maxwell model against the experimental results of effective thermal conductivity of U-10Zr. The most striking result to emerge from the data shown in Figure 32 is that the effective thermal conductivity predicted based on Maxwell model lower than those measured experimentally for all various theoretical densities of U-10Zr (almost except 80.9% case with the range 40 ℃ to 200 ℃.) .

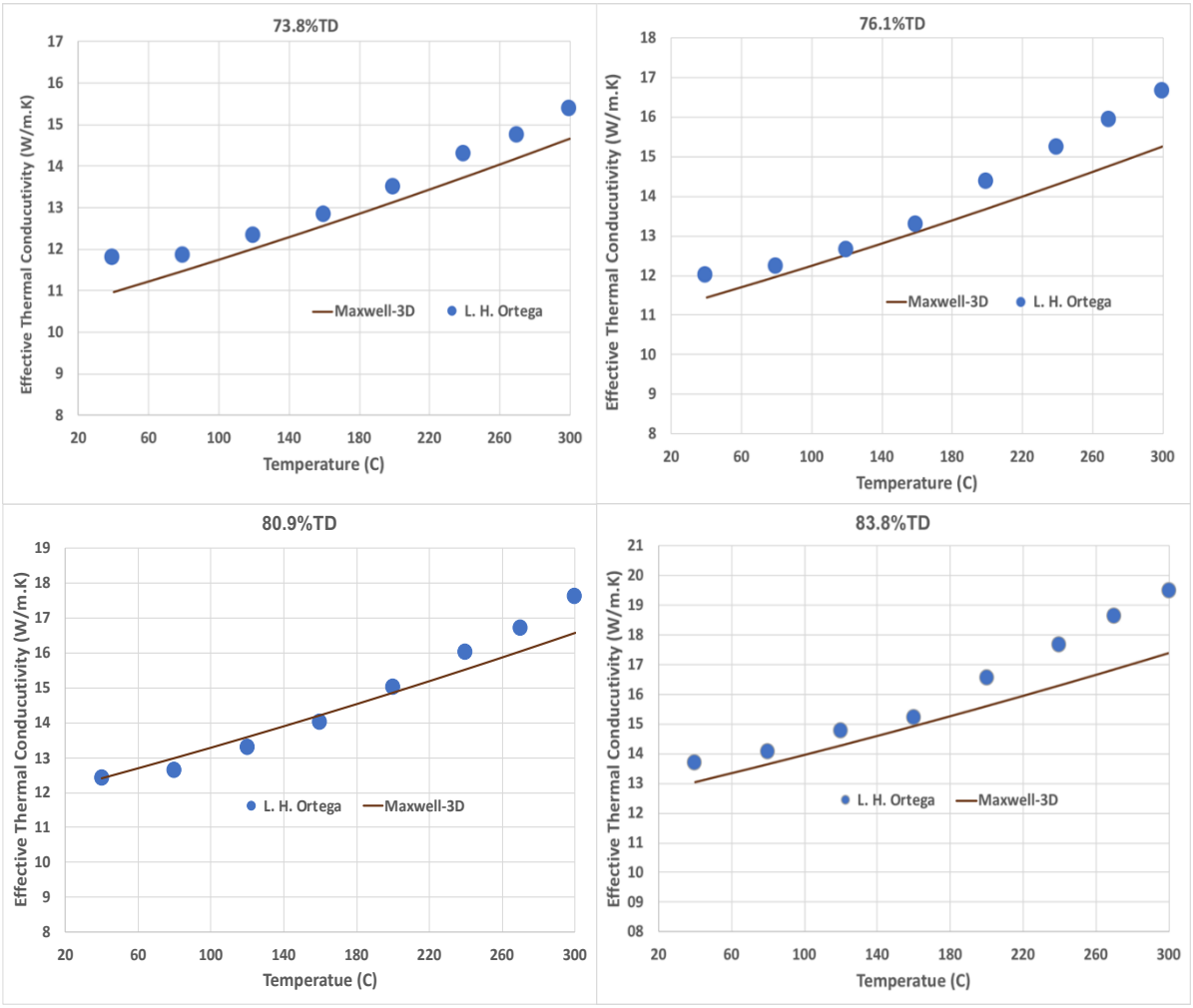

Figure 32. The effective Kapitza resistance based on Maxwell model and experimental measurements versus temperature for various theoretical densities of U-10Zr.

This is clearly in contrast to the result that is showed in the previous subsection. Moreover, this is unexpected due to fact that the Kapitza resistance is not considered in the Maxwell model and that should render its results higher than the experimental values.

Based on the aforementioned, we can infer that there is/are parameter/parameters other than the Kapitza resistance takes place and affects positively on the measured values and is/are not considered in the Maxwell model. Since this challenge showed only in U-Zr case, we can infer that Zr content has a direct connection to this unclear result. By reviewing the BSE images showed in Figure 28, we found clearly that there is a third phase show up in the U-10Zr while not in Dep_U. The new phase was created due to Zr precipitation phenomenon. Thus, the simulations are modified by adding a third phase (Zr-precipitates), the total volume of precipitates that are dispersed into few random particles based on the calculated values in table 7. The interface thermal resistance of the dispersed precipitates is ignored. This due to fact that its maximum volume fraction is less than 2%. Figure 33 shows that by adding the precipitates effect, in contrast to the Maxwell's results showed in figure 32, the MOOSE results are higher than measured values and that can be explained by that creation the Zr precipitates lead to reducing the Zr content in the fuel, and according to the empirical models [96, 97] and the experimental data in the literature [98, 99], the effective thermal conductivity increases as the Zr content decreases.

Additionally, Figure 33 shows that the initial predictions of MOOSE (without implementing the Kapitza resistance) are higher than the experimental results and that due to the absent of interfacial thermal resistance between the fuel matrix and second phase particles. For the theoretical densities 73.8%, 76.1%, 80.9%, and 83.8% cases shown in Figure 33, the difference between MOOSE and the experimental results varied from 7-8%, 9-4%, 12.9-4.5%, and 9-0.25% with temperature, respectively.

The agreement between FEM and the experimental work results is improved as showed in Figure 33. Without the implementation of the Kapitza effect, the FEM results were sternly greater than the experimental results, and the Kapitza resistance appreciably reduces the effective thermal conductivity, making the improved agreement unsurprising. For theoretical densities 73.8%, 76.1%, 80.9%, and 83.8% cases, the agreement was improved from 7-8%, 4-9%, 4.5-12.9%, and 0.25-9% difference to 3.8-4.4%, 0.15-1.4%, 1.4-3.6%, and 1.4-2.4% difference across the temperature range studied, respectively.

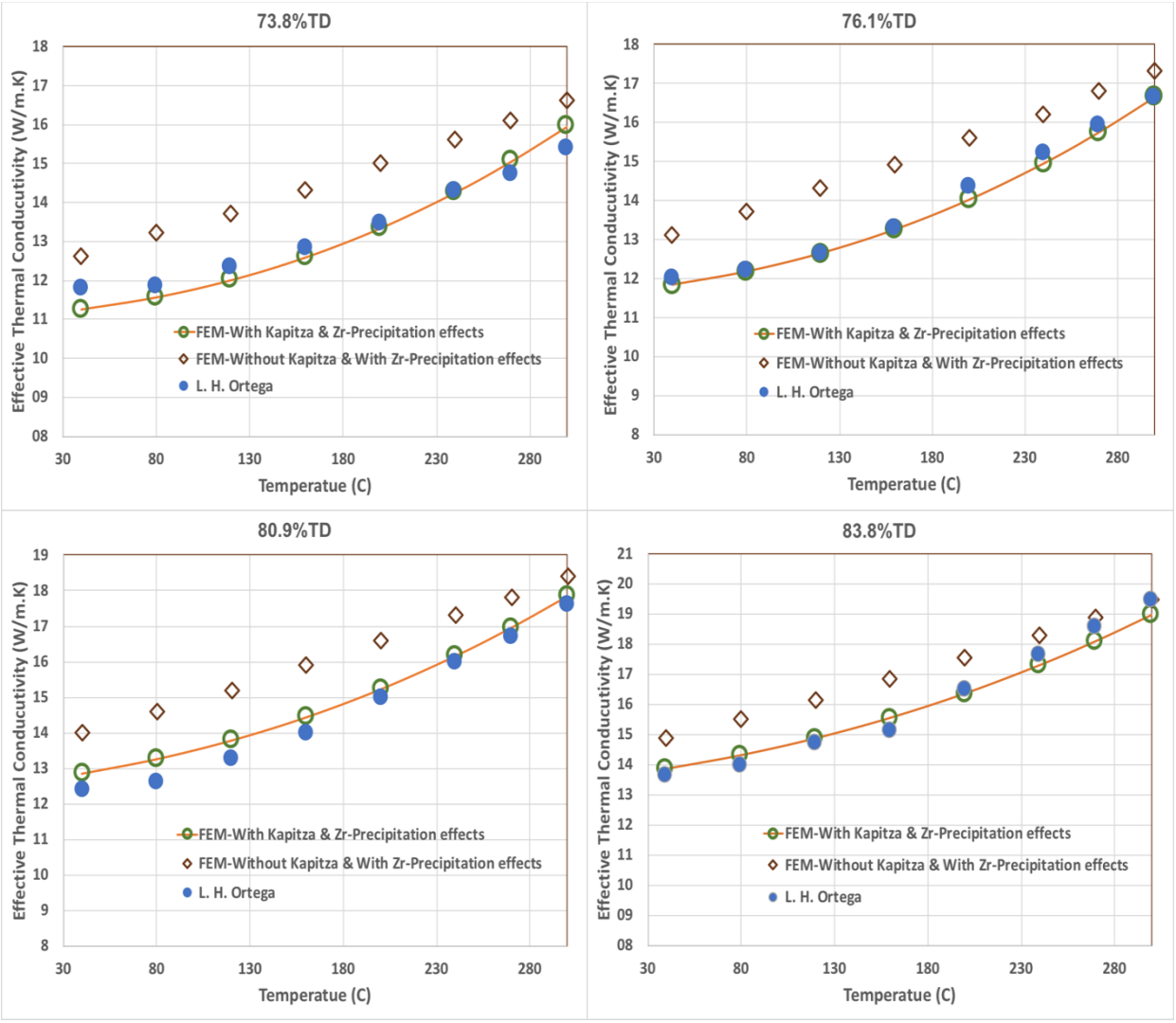

Figure 33. The effective Kapitza resistance versus temperature for various theoretical densities of U-10Zr with considering the precipitates effect.

Figure 34 (left) shows that when the Kapitza resistance is introduced into the implementation of the thermal conductivity as discussed earlier, the effective thermal conductivity is reduced as expected. As shown in Figure. 34 (left) for theoretical densities 73.8%, 76.1%, 80.9%, and 83.8% cases, the reduction in the overall thermal conductivity with the introduction of the Kapitza resistance was 4-14%, 3.85-13%, 3-10.25%, and 2.7-8.65% across the temperature range studied, respectively. Similar to the previous case, the reduction in the overall thermal conductivity due to Kapitza effect decreases as the theoretical density of the fuel increases. The reason behind that is increasing the theoretical density led to decreasing the surface area of second phase particles,

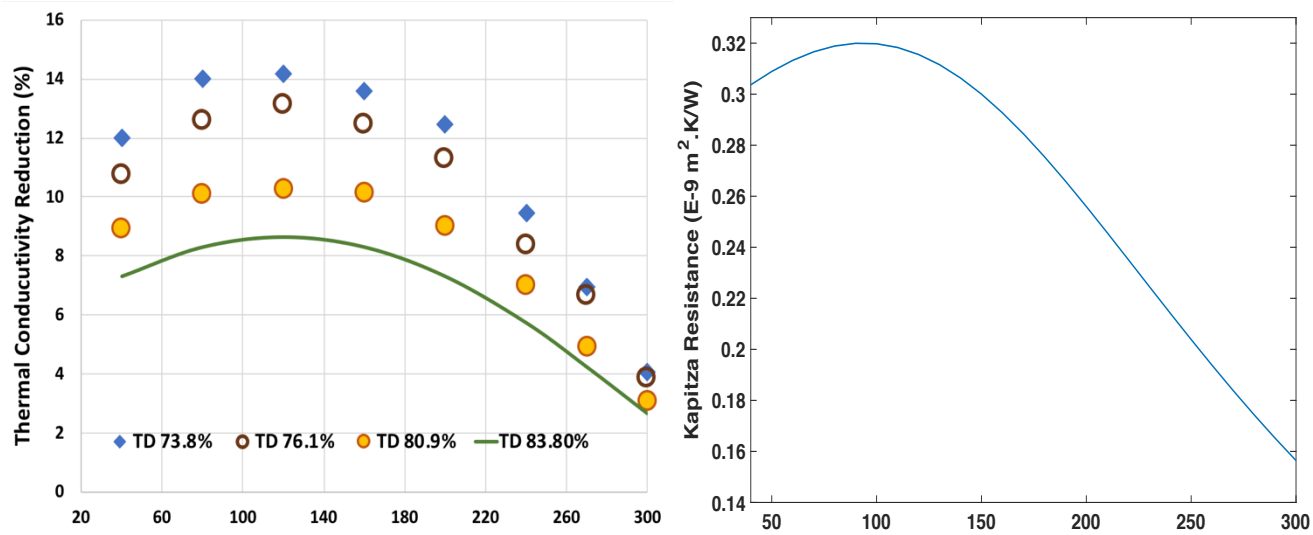

Figure 34. Thermal conduction reduction due to Kapitza effect (left) the effective Kapitza resistance versus temperature (right) and for all various theoretical densities of U-10Zr.

resulting in a smaller effect when the Kapitza resistance is implemented.

Figure 34 (right) shows that the behavior of Kapitza resistance versus temperature. First, by comparison this figure with Figure 31(left), we can see that the interfacial resistance for U-Zr with second phase particles is less than those for dep_U. This might happen due to fact that Zr atoms are considering as light atoms respect to U and adding the light atoms to an interface could improve the interface thermal conductivity because the atoms bridging improving[30-35, 57]. Second, the trend hers is increasing with temperature up to some point and decreasing after that. Since We can infer that the Zr atoms are the main reason behind that behavior for two facts. First, this is not the trend of pure uranium in the previous case, where the trend was decreasing continuously with temperature. Second, the effective thermal conductivity of the pure Zr is decreasing with temperature to some point and then start increasing which is similar to the current behavior of the Kapitza resistance.

CHAPTER V

A HYBRID ML– MESOSCALE SIMULATION-BASED APPROACH TO THERMAL CONDUCTIVITY MODELING

5.1 Introduction

Machine learning is an application that provides systems the ability to access data and use it to learn for themselves and improve from experience without human intervention. Typically, ML algorithms are divided into supervised, unsupervised, semi-supervised, and reinforcement learning. In supervised learning, the learning algorithm uses a set of input values and a corresponding set of output values to infare a suitable function to make accurate predictions of the output values that will be associated with new input values. By sufficient training, the developed model will be to provide targets for any further input. On the opposite, in unsupervised learning algorithms, the training data are not labeled. The algorithm does not predict the output, but it examines the input data to identify its patterns or describe its hidden structures[100]. In semi-supervised learning, the learning algorithm uses both labeled and unlabeled data for training, so it can significantly enhance learning accuracy. Unlike supervised learning, Reinforcement machine learning algorithms do not use maps or labeled data. Instead, the reinforcement learning algorithm uses trial and error search and a delayed reward approach in the absence of training dataset. This approach provides software agents the capability to determine the best behavior without any external intervention within a specific context to maximize its performance[101].

5.2 A hybrid ML-Mesoscale Model of Thermal Conductivity

In general, regression, classification, and anomaly detection methods are widely used in supervised learning algorithms. Where the main target here is to predict the effective thermal conductivity, this work is done based on supervised learning algorithms, more specifically regression algorithms. To build any ML model, five main steps should be implemented (schematically illustrated in Figure. 35):

A. Data collection.

The input data can be obtained from various sources such as computational methods, the literature, or experimental studies; in the current work, most of the data used are taken from the experimental team of nuclear materials and fuel cycles at Nuclear Engineering Department, Texas A&M.

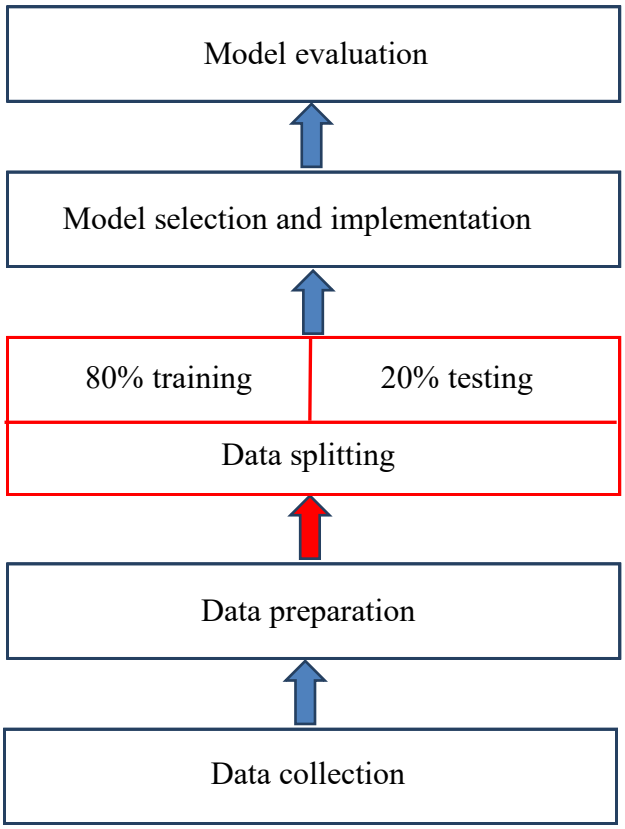

Figure 35. A schematic illustration of conventional ML approach.

B. Data preparation

Data preparation is an essential step in developing any ML model; careful data preparation leads to significant improvement in model predictions. For instance, sometimes the datasets include invalid values, or some data are missing. In the case of missing values, the algorithm will not be executed. Moreover, the invalid data will reduce the accuracy of the model.

C. Data splitting

Usually, input data is randomly split into 80% and 20% for training and testing, respectively. However, in this work, all available experimental data from Step A is used entirely in the training stage (schematically illustrated in Figure. 36). The testing stage is performed based on the validated mesoscale models instead of 20% of the experimental data.

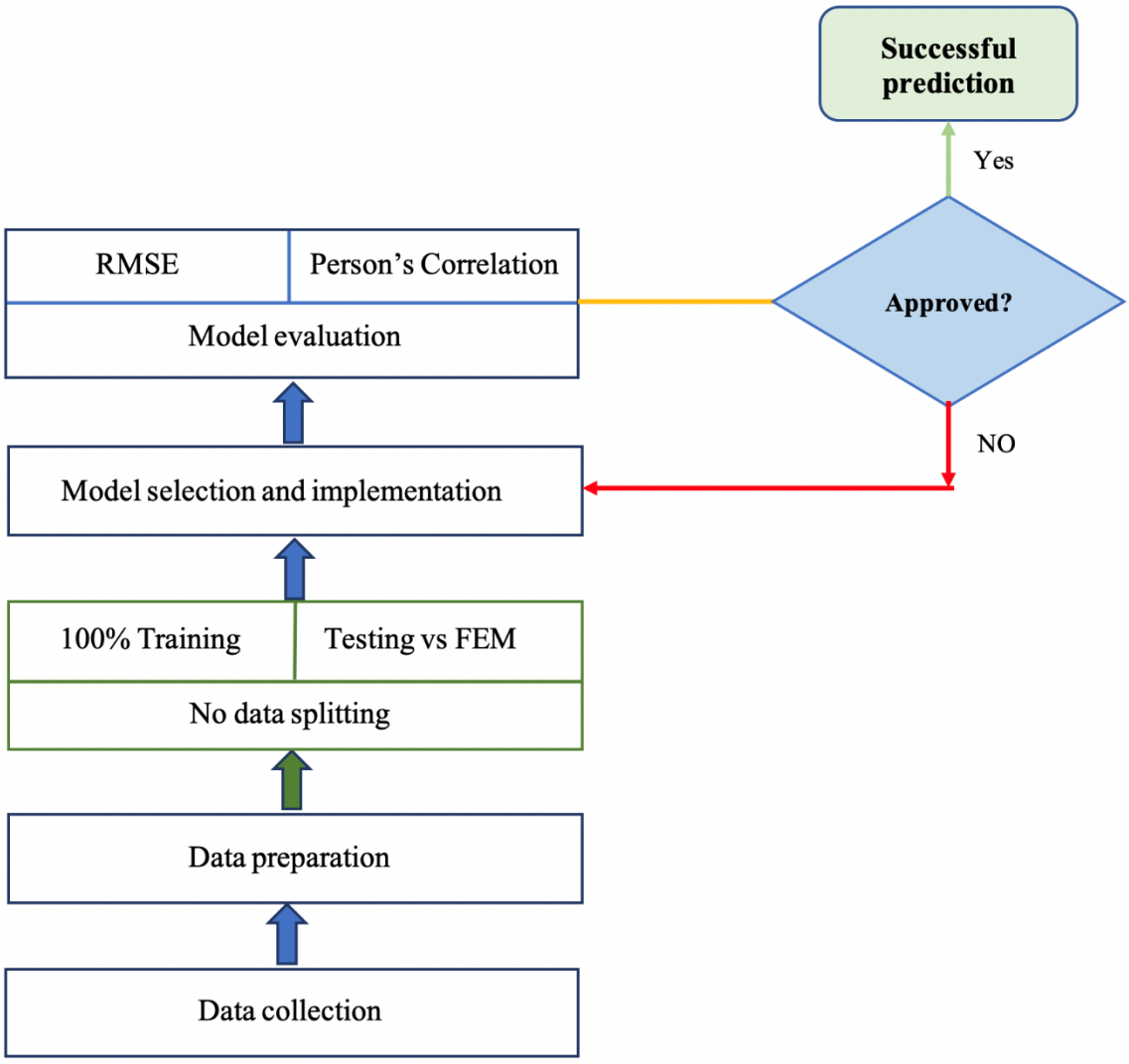

Figure 36. A schematic illustration of a hybrid ML approach & mesoscale modeling approach.

D. Choosing the best ML algorithm.

Various supervised learning algorithms are implemented in this study. Based on the testing stage, each algorithm's performance is evaluated, and the optimal model is determined.

I. Bayesian ridge algorithm

Ridge Regression is a classical regularization method broadly used in statistics and machine learning. The conventional least squares estimates are unbiased, but their prediction come with high variances. So, ridge is a simple technique to prevent over-fitting which may result from simple linear regression. Basic principle for the ridge regression is a degree of bias to the regression estimates that could increase the biased for specific range but improve it on the overall range and prevent the overfitting.

$$\sum_{i=1}^{M}(y_i - \hat{y}_i)^2 = \sum_{i=1}^{M}(y_i - \sum_{j=1}^{p} w_j \times x_{ij})^2 + \lambda \sum_{j=1}^{p} w_j^2 \quad (5.1)$$

Where λ is the penalty parameter and w_j is fitting coefficients.

By using the Bayesian method, the linear regression is using probability distributions rather than point estimates. The response, y, is not estimated as a specific value, but is expected to be drawn from a probability distribution[102]. Thus, the model for Bayesian Linear Regression with the response sampled from a normal distribution is:

$$y \sim N\ (\beta^T\ X, \sigma^2\ I) \quad (5.2)$$

The goal of Bayesian Linear Regression is not to find the specific "best" value of the model parameters, but rather to determine the posterior distribution for the model parameters.

$$P(\beta|y, X) = \frac{(y|\beta, X) * P(\beta|X)}{P(y|X)} \quad (5.3)$$

Here, P(β|y, X) is the posterior probability distribution of the model parameters given the inputs and outputs. This is equal to the probability of the data, P(y|β, X), multiplied by the prior probability of the parameters and divided by a normalization constant[102].

II. Random Forest Algorithm

The random forest algorithm is a supervised regression and classification algorithm that creates the forest with a number of trees. Like in the nature, the forest looks like more robust with the more trees in the forest. In the similar way, in the random forest regressor, the higher the number of trees in the forest produces the high the accuracy results [103]. So, the basic principle for the random forest is to combine many decision trees into a single model. By this combination, the predictions will be closer to the mark on average. Moreover, the main difference between the random forest algorithm and the decision tree algorithm is that in Random Forest, the processes of selecting the root node and splitting the feature nodes is randomly. For instance, each time a split in a tree is considered, a random sample of m predictors is selected as split candidates from the full set of p predictors. The split is allowed to use only one of those m predictors [104].

before each split, select $m \leq P$ *of the input features at random as candidates for splitting*

Moreover, The random forest algorithm have many advantages such as can be used for a variety of tasks including be used for both classification and regression tasks, very robust, [105]. Additionally, no overfitting problem show up with using the random forest algorithm in any classification problem [103].

To explain this more, let us assume there is a training set of N training examples, and for each example there are P features, and a random forest will consist of N_{tree} decision trees [105] (see Figure 37).

1. Bootstrap aggregating

Subsets of the training data of size n will be sample repeatedly from the training set of N examples where n is less than N. Sampling will be done at random but with replacement. This process is called bootstrap aggregating.

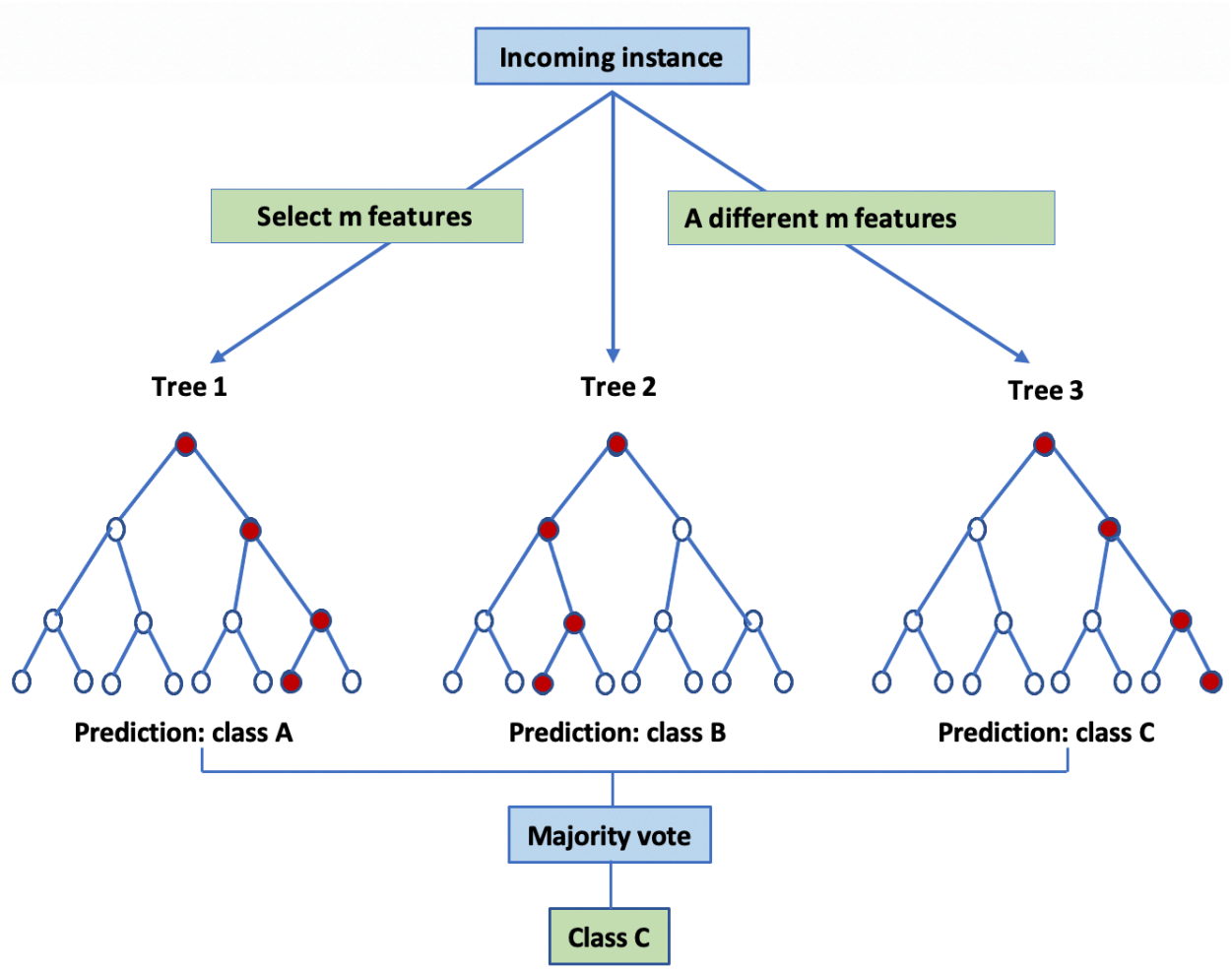

Figure 37. Random forest inference for a simple classification example with just three trees

2. Random subspace method

As we mentioned above, with each training example has M features, a subset of them of size m < P will be selected to train each tree. Thus, each tree will use only m features of n training examples.

3. Training decision trees

N_{tree} decision trees are created and each one is trained on a different set of m features and n training examples. The trees are not snipped, as they would be in the case of training a simple decision tree regressor.

4. Perform inference by aggregating predictions of decision trees

To make a prediction for a new input data, the relevant features of this example is passed to each of the N_{tree} estimators. Then, the N_{tree} predictions are combined to produce the overall prediction of the random forest. It is noteworthy to mention here, that for the classification purpose, the majority voting will be used to decide on the predicted class, but in the case of regression, the mean value of the predictions is utilized of all the decision trees.

III. Multi-polynomial Algorithm.

The multiple-polynomial regression algorithm was implemented to predict the thermal conductivity of the selected nuclear fuels. This Algorithm is constructed to computes the relationship between the dependent variable (thermal conductivity) with one or more independent (temperature and composition) variables. Where the effective thermal conductivity of the selected nuclear fuels is not functioning only in the temperature but in the compositions also, so the multiple-polynomial regression algorithm was selected. The general formulation of the third order the multiple polynomial for two variables was derived and described as follow:

$$y(x_1, x_2) = \beta_0 + \beta_1 x_1 + \beta_2 x_2 + \beta_3 x_1 x_2 + \beta_4 x_1^2 + \beta_5 x_2^2 + \beta_6 x_1^3 + \beta_7 x_2^3 + \beta_8 x_1 x_2^2 + \beta_9 x_2 x_1^2 + \varepsilon \qquad (5.4)$$

Where:

$\beta_0, \beta_1, - - -, \beta_8, and\ \beta_9 \equiv are\ determination$ coefficients.

$x_1 \equiv composition\ fraction\ variable$

$x_2 \equiv$ temperature in C.

$\varepsilon \equiv the\ residual$

E. Model Evaluation

Last and most important step is to evaluate performance and accuracy of the selected model. Through the current work, two metrics are used in parallel to check the efficiency of the developed model:

First, root-mean-square error (RMSE):

Measure the difference between values predicted by the proposed model and observed values. RMSE can be expressed by [106],

$$\mathrm{RMSE} = \sqrt{\frac{\sum_{i=1}^{N}(y_i - \hat{f}(x_i))^2}{N}} \tag{5.5}$$

Where: y_i is the actual value, $\hat{f}(x_i)$ is the prediction that gives $\hat{f}$ for the ith observation and N is number of non-missing data points. The RMSE will be small if the predicted responses are very close to the actual values and will be large if the predicted and true responses differ significantly [106].

Second, Pearson's correlation coefficient (r):

Measure of the associative strength between the predicted and the measured values. RMSE can be obtained by [107],

$$\mathrm{r} = \frac{\sum_{i=1}^{N}(x_i - \bar{x})(y_i - \bar{y})}{\sqrt{\sum_{i=1}^{N}(x_i - \bar{x})^2}\sqrt{\sum_{i=1}^{N}(y_i - \bar{y})^2}} \tag{5.6}$$

Where N is number of non-missing data points, x_i and y_i are the values of x and y for the ith individual, and $\bar{x}, \bar{y}$ are the corresponding mean values, these values can be obtained by

$$\bar{x} = \frac{1}{N}\sum_{i=1}^{N} x_i \tag{5.7}$$

$$\bar{y} = \frac{1}{N}\sum_{i=1}^{N} y_i \tag{5.8}$$

The r will close to the unity value if the predicted responses are almost having a linear relation with the actual values and will be far away from the unity if not.

5.3 Results and Discussion

5.3.1 A hybrid Physics-Based and Data-Driven approach for predicting the Effective Thermal Conductivity of UO2 and BeO Composite Nuclear Fuel

The training stage of the selected ML approaches: Bayesian ridge, random forest and multi-polynomial algorithms is performed based on the whole available experimental data for UO2-BeO composite nuclear fuel. The data include three different compositions, within a temperature range from 25 to 300 ℃ with 25 ℃ increment [40]. The training results are shown in Figure 38. As can be seen from the figure, the multi-polynomial algorithm has the best accuracy.

While the RMSE values for the Bayesian ridge and the random forest algorithms are 30% and 7.5%, respectively, the RMSE value achieved by the multi-polynomial algorithm is only 1.6%. Based on the training results (shown in Figure.38), the random forest and multi-polynomial algorithms are selected to be used in the testing stage.

The testing stage is usually done by using 20% of the experimental data. Nonetheless, part of the novelty presented in this work lies in utilizing the mesoscale model results in testing. In effect, this leaves 100% of the available experimental data for training only which improves the ML algorithm's accuracy and does not limit the ML to costly experimental runs. The validated developed mesoscale model is used to produce new data set for the testing stage [40]. This is done for the same temperature range used to obtain the experimental data (25-300 ℃), and at 7.5 and 12.5% BeO volume fractions.

According to the results shown in Figure.39, the maximum error between the developed random forest model and the mesoscale model was about 74%. That due to fact random forests have high performance for classification problems but have slightly less accuracy at regression problems [105]. While the maximum error between the developed multiple polynomials model and the mesoscale model is about 10% (see Figure. 40,). this means the multiple polynomials model is the best candidate to the prediction stage. Therefore, the multi-polynomial algorithm is chosen to predict the effective thermal conductivity for various compositions, and a broader temperature range of UO2-BeO composite nuclear fuel.

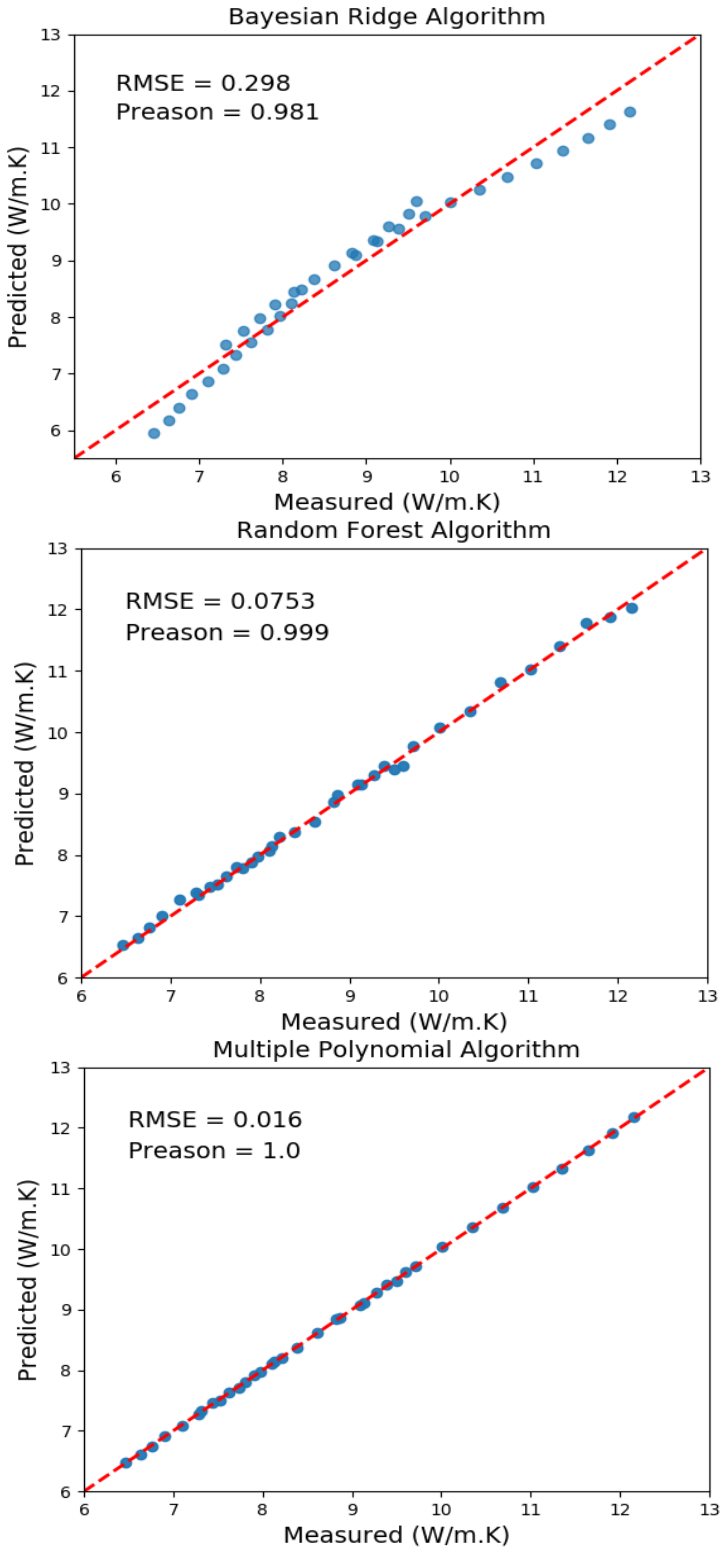

Figure 38. Training stage for various ML algorithms against the experimental thermal conductivity data at different BeO volume fractions 5%, 10%, and 15% UO2-BeO nuclear fuel

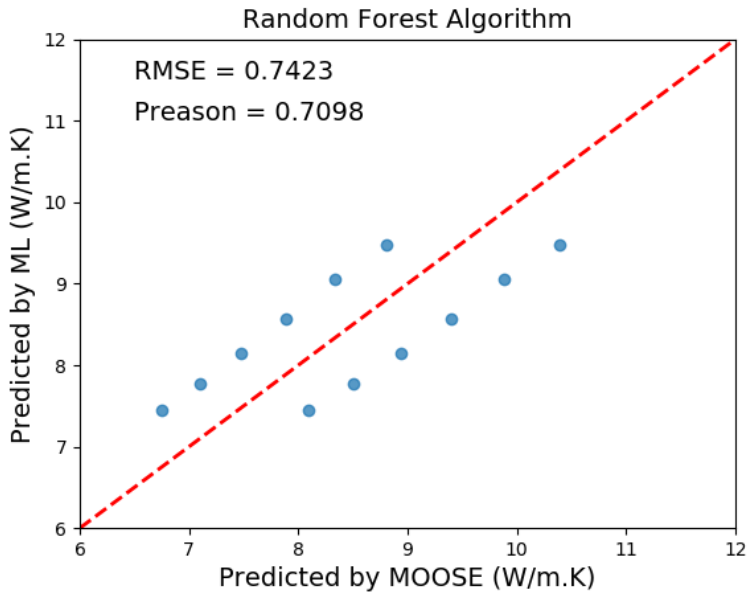

Figure 39. ML testing stage against the mesoscale model, at 7.5 and 12.5 % dispersed volume fraction of BeO based on random forest regressor algorithm

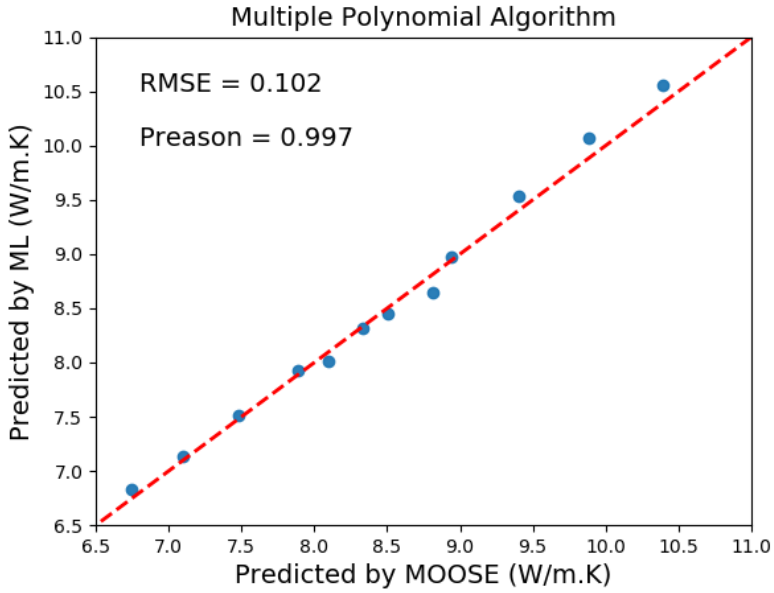

Figure 40. ML testing stage against the mesoscale model, at 7.5 and 12.5 % dispersed volume fraction of BeO based on random multiple polynomial algorithm

Thus, the selected model is used to predict unknown data of thermal conductivity coevolution of the UO_2-BeO nuclear fuel. Guided by the fact that ML is a predictive tool, we aim to apply it to estimate thermal conductivity values of systems outside the experimental range. As such,

for a broader range of BeO volume fraction (8, 12, 16, and 20%) and temperatures (25 – 400 ℃), thermal conductivity is predicted using the ML algorithm. The prediction results are presented in Figure.41. The trend, as can be seen in this figure is physically appreciated in the sense that it matches well with experimental data trends [40].

According to the predicted values, as volume fraction of the dispersed BeO increases, the sensitivity of the effective thermal conductivity increases. This is in good agreement with experimental data which are presented in Figure. 21-a.

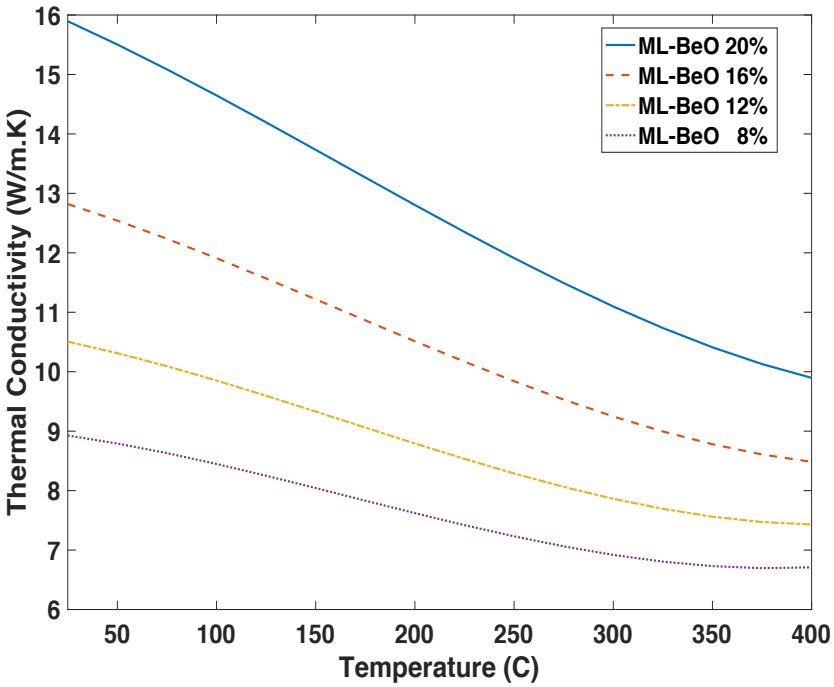

Figure 41. The prediction results from the proposed ML Algorithm for the thermal conductivity evolution of the UO2-BeO nuclear fuel at 8,12,16 and 20% dispersed volume fractions and 25-400 ℃ temperature range.

5.3.2 A hybrid Physics-Based and Data-Driven approach for predicting the Effective Thermal Conductivity of U-10Zr metallic Nuclear Fuel

Similar to the previous case, the training stage of the selected ML algorithms Bayesian ridge algorithm, random forest algorithm and multi-polynomial algorithm is performed based on the whole available experimental data for U-10Zr metallic nuclear fuel with theoretical densities of 73.8%, 76.1%, 79.6%, 83.5%and 83.8%, within a temperature range from 40 ℃ to 300 ℃ and with increment 10 ℃ [75]. The training results are presented in Figure 42.

Based on the training stage, the produced RMSE values for the Bayesian ridge and the random forest algorithms are 39.5% and 6.7%, respectively. While, the corresponding RMSE value of the multi-polynomial algorithm is 6%.

As we mentioned before, the testing stage is usually done by using 20% of the experimental data. As a novel approach, the mesoscale simulations are utilized to create the required data in the testing stage. In effect, this leaves the whole available experimental data for training only which improves the ML algorithm's accuracy and does not limit the ML to costly experimental runs. Again, the developed validated mesoscale model is used to produce a new data set for the testing stage. This is done at the same range of temperature applied for the experimental data (40-300 ℃), and theoretical densities of 75% and 80%.

Based on the training results shown in Figure. 42, the random forest and multi-polynomial algorithms are selected to be used in the testing stage. According to the results shown in Figure. 43, the maximum error between the developed random forest model and the mesoscale model is about 33.8% and that is for the same reason mentioned above. Moreover, as obvious from Figure 43, the produced error is less than the one created in Figure 39. The reason behind that is the amount of the training data used in U-Zr which is more than the one used in UO_2-BeO. Based on the results shown in Figure. 44, the maximum error between the developed multiple polynomials model and the mesoscale model is about 9%, that means the multiple polynomials model is the best candidate to the prediction stage.

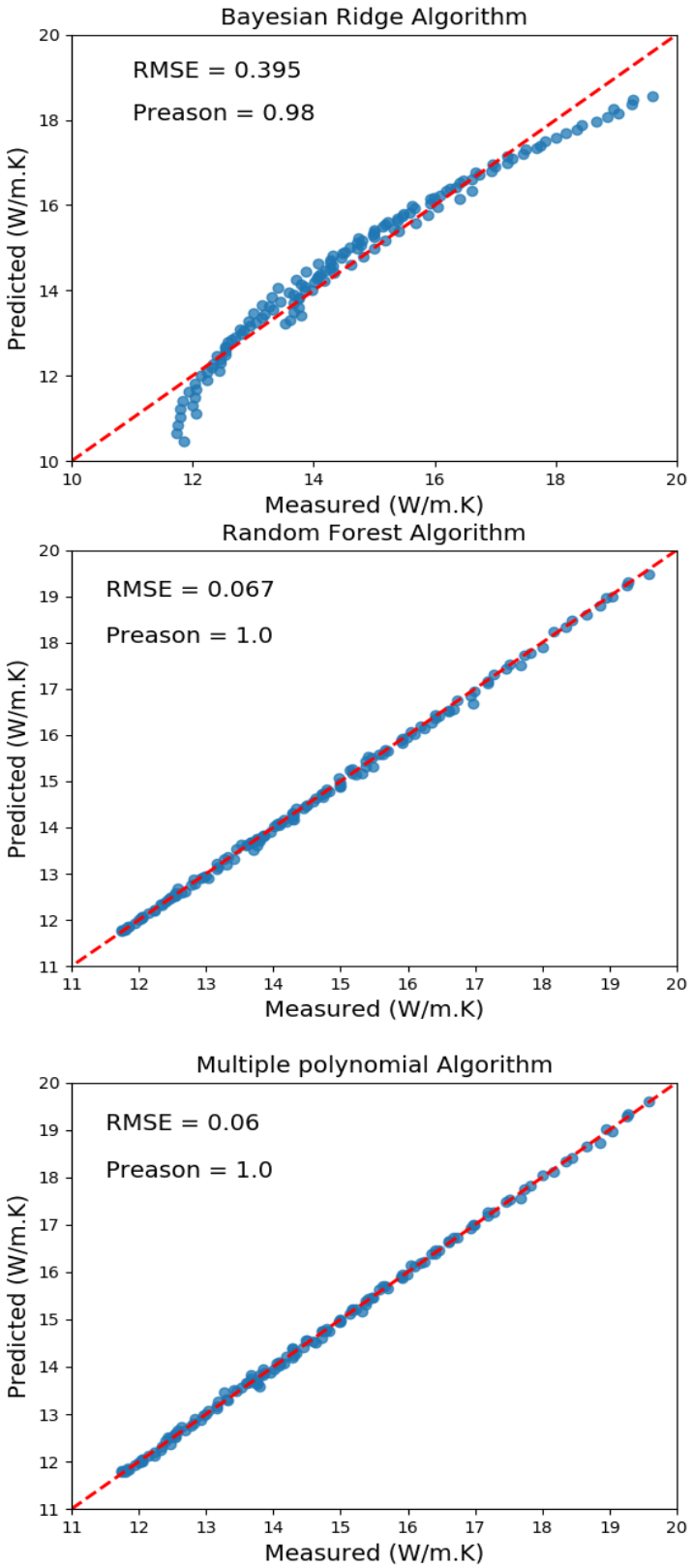

Figure 42. Training stage for various ML algorithms against the experimental thermal conductivity data at different theoretical densities 73.8%, 76.1%, 79.6%, 83.5% and 83.8% of U-10Zr nuclear fuel.

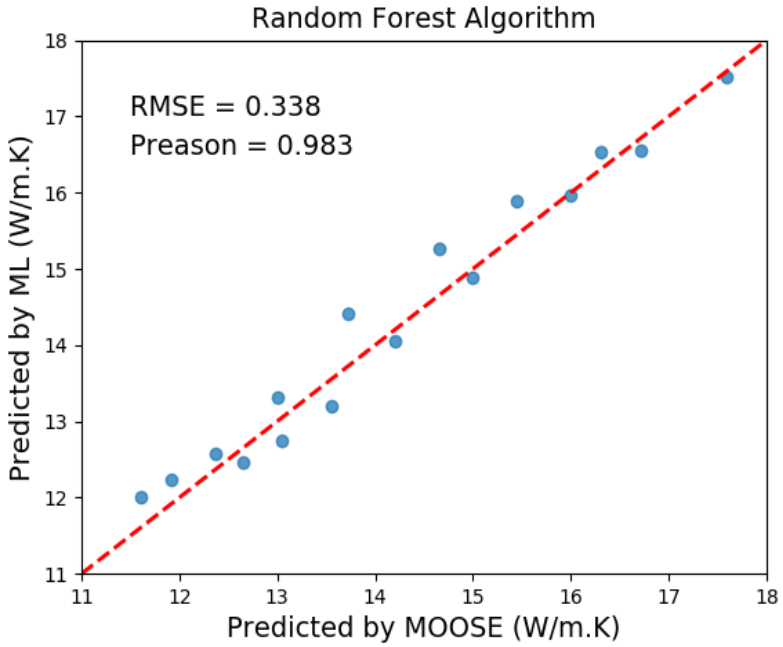

Figure 43. Testing stage against the mesoscale thermal conductivity data at different theoretical densities 75% and 80% of U-10Zr nuclear fuel based on random forest algorithm.

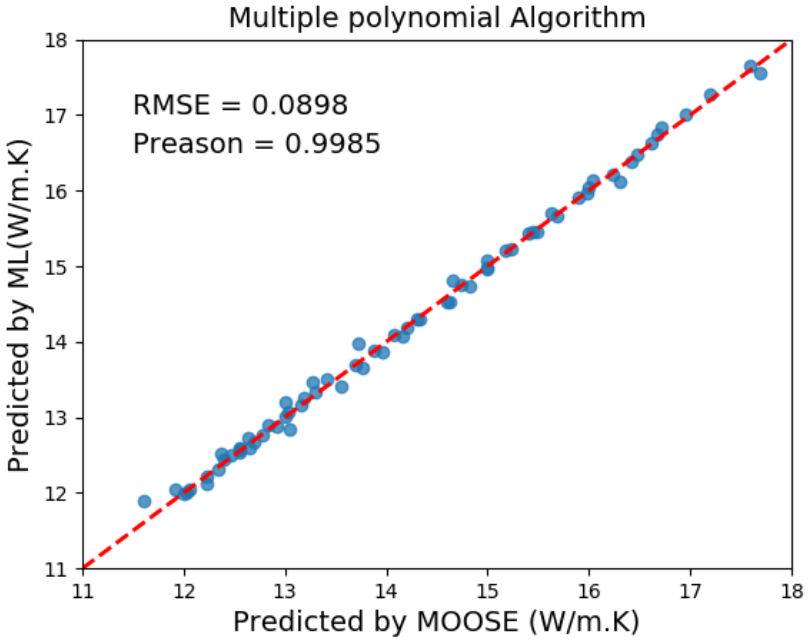

Figure 44. Testing stage against the mesoscale thermal conductivity data at different theoretical densities 75% and 80% of U-10Zr nuclear fuel based on multiple polynomials algorithm.

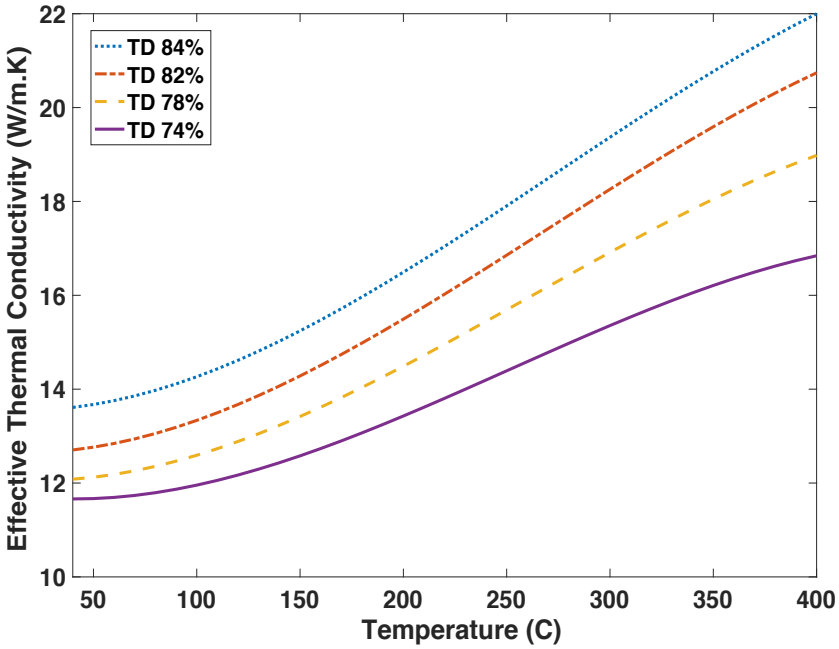

Figure 45. Prediction at different theoretical densities 74%, 78%, 82% and 84% of U-10Zr nuclear fuel based on multiple polynomials algorithm.

Lastly, the multiple polynomials model is used to predict unknown data of thermal conductivity of the U- 10Zr nuclear fuel. Guided by the fact that ML is a predictive tool, we aim to apply it in estimating thermal conductivity values for systems outside experimental range. As such, a broader range of theoretical density and temperatures (40 – 400 ℃) were predicted using the ML algorithm. The prediction results are presented in Figure.45.

Similar to the pervious case, the predictions of thermal conductivity of U-Zr metallic nuclear fuels outside experimental range as shown in Figure 32 are consistent with experimental data.

CHAPTER VI

SUMMARY AND CONCLUDING REMARKS

A novel model for the effective thermal conductivity of polycrystalline solids was developed. In contrast to existing models, this model is based on the thin-interface description of boundaries. This treatment leads to two major advantages over the classical sharp-interface description. First, it enables the model to predict the thermal conductivity of nanocrystalline materials, where the grain size is comparable to the GB width. Second, it allows the model to simulate the enhancement or degradation of interfacial transport due to segregation, interface roughness, interface strengthening, or interface phase transition.

In our derivation of the model, we introduced a general expression for the effective Kapitza resistance/conductance of a thin interface. This new expression was validated using finite-element simulations for different GB thermal conductivity profiles. This new continuum-based treatment of interfacial heat transport is expected to contribute to the understanding of optimizing heat transport via the different methods of interface engineering, which are usually only modeled using atomistic simulations [12, 13, 35, 37].

The predictions of the new model were compared with the existing analytical models. It was shown that the thin-interface based model predicts higher values for the effective thermal conductivity and Kapitza resistance than its sharp-interface counterparts. These predictions were verified using finite-element simulations. For nanograins, the new model predicts 10%-100% higher values of the effective thermal conductivity than Yang et al. model [8], as the grain size approaches the width of the grain boundary. Moreover, the new model was shown to be capable of describing the change of thermal conductivity with microstructure. By coupling the heat-conduction and phase-field equations, finite-element simulations of the co-evolution of microstructure and thermal conductivity were performed for different grain structures. The predictions of the new models were closer to the results from the FEM simulations than those given by the model of Yang et al. [8]. While, we focused here on heat transport across grain boundaries in polycrystalline materials, we also discussed in the appendix how this new approach can be generalized to the case of hetero-interfaces in multiphase materials. However, a complete treatment of this case is beyond the scope of this study and will be investigated in the future.

Additionally, as with any model, this new model has some limitations. Two main limitations can be recognized. First, the model ignores quantum effects that might alter the transmission and scattering probabilities of heat carries in the vicinity of interfaces. However, it is well known that these effects are of importance only in the low temperature regime. Second, the model assumes the validity of Fick's law to describe heat conduction. While this is difficult to justify for nanocrystalline materials, several non-equilibrium molecular dynamics simulations demonstrated that it is a reasonable assumption[12, 13, 35, 37]. This assumption is also employed in most of existing analytical/continuum models and even experimental studies of heat transport in heterogenous solids[1, 8-11]. Nonetheless, our main approach can be adapted to other constitutive laws of interest. For instance, one can utilize the concepts of extended irreversible thermodynamics to derive more appropriate constitutive laws that account for non-local, non-linear, and ballistic effects on interfacial heat transport[108].

A quantitative mesoscale model of the effective thermal conductivity of UO2–BeO fuel composite nuclear fuel was developed. The model accounts for the effects of temperature, underlying microstructure, and interface thermal resistance on the effective thermal conductivity. The model predictions were validated against contemporary experiments, and excellent agreement was achieved. Specifically, the differences between the model predictions the experimental results were on average< 5% for most temperatures and volume fractions, which is within the level of precision of the experimental measurements. It was demonstrated that considering the interface thermal resistance in the model formulation is required to obtain better predictions.

Both the model and experimental results confirmed that the effective thermal conductivity for a continuous microstructure is higher than its counterpart in the dispersed microstructure. This can be attributed to the fact that heat flows more easily in composites with a continuous conducting phase, which will also have a lower interfacial area and hence lower overall interface resistance. Therefore, it is recommended to produce UO2–BeO composites with a continuous microstructure for use as an accident-tolerant fuel (ATF).

In this study also, development and implementation of two quantitative mesoscale models for the effective thermal conductivity of dep_U and U-Zr were undertaken. Similar to UO2–BeO composite fuel, these models account for the effects of temperature, underlying microstructure,

and interface thermal resistance on the effective thermal conductivity. Additionally, this work used a joint experimental and modeling approach to quantify the Kapitza resistance between the fuel components and utilized it to improve the accuracy of predictions of the thermal conductivity of the Dep-U and U-10Zr. Companion experiments were conducted to validate the model predictions. It was demonstrated that accounting for the interface (Kapitza) thermal resistance and Zr precipitation phenomenon are necessary to improve the model predictions. The largest difference between the model calculations and experimental results was about 4.5%, which is within the precision of the experimental measurements.

A hybrid ML– mesoscale simulation-based approach to thermal conductivity modeling is developed through this study. This novel model is developed based on integrating the conducted experimental work, validated mesoscale models, and various ML algorithms. The main advantage of this new approach is overcoming the accompanying challenges of the experimental and computational work. The developed combined model is implemented to predict the effective thermal conductivity of UO2- BeO Composite and U-Zr metallic nuclear fuels. Moreover, the advantage of using this hybrid phase-field and finite-element approach is that it can directly simulate the coevolution of the microstructure and physical properties of materials in both steady–steady state and transient situations and under different driving forces.[109, 110]

REFERENCES

[1] H. Dong, B. Wen, and R. Melnik, "Relative importance of grain boundaries and size effects in thermal conductivity of nanocrystalline materials," *Sci Rep,* vol. 4, p. 7037, Nov 13 2014.

[2] D. S. Smith, S. Fayette, S. Grandjean, C. Martin, R. Telle, and T. Tonnessen, "Thermal resistance of grain boundaries in alumina ceramics and refractories," (in English), *J Am Ceram Soc,* vol. 86, no. 1, pp. 105-111, Jan 2003.

[3] W. Chen and X.-M. Bai, "Unified Effect of Dispersed Xe on the Thermal Conductivity of UO2 Predicted by Three Interatomic Potentials," *Jom-Us,* vol. 72, no. 4, pp. 1710-1718, 2020.

[4] M. A. Angadi *et al.*, "Thermal transport and grain boundary conductance in ultrananocrystalline diamond thin films," (in English), *J Appl Phys,* vol. 99, no. 11, Jun 1 2006.

[5] D. G. Cahill *et al.*, "Nanoscale thermal transport," *J Appl Phys,* vol. 93, no. 2, pp. 793-818, 2003.

[6] M. A. Meyers, A. Mishra, and D. J. Benson, "Mechanical properties of nanocrystalline materials," (in English), *Prog Mater Sci,* vol. 51, no. 4, pp. 427-556, May 2006.

[7] P. G. Klemens, "The Scattering of Low-Frequency Lattice Waves by Static Imperfections," (in English), *P Phys Soc Lond A,* vol. 68, no. 12, pp. 1113-1128, 1955.

[8] H. S. Yang, G. R. Bai, L. J. Thompson, and J. A. Eastman, "Interfacial thermal resistance in nanocrystalline yttria-stabilized zirconia," (in English), *Acta Mater,* vol. 50, no. 9, pp. 2309-2317, May 24 2002.

[9] C. W. Nan and R. Birringer, "Determining the Kapitza resistance and the thermal conductivity of polycrystals: A simple model," (in English), *Phys Rev B,* vol. 57, no. 14, pp. 8264-8268, Apr 1 1998.

[10] J. Amrit, "Grain boundary Kapitza resistance and grain-arrangement induced anisotropy in the thermal conductivity of polycrystalline niobium at low temperatures," (in English), *J Phys D Appl Phys,* vol. 39, no. 20, pp. 4472-4477, Oct 21 2006.

[11] P. L. Palla and S. Giordano, "Transport properties of multigrained nanocomposites with imperfect interfaces," *J Appl Phys,* vol. 120, no. 18, 2016.

[12] R. Li, K. Gordiz, A. Henry, P. E. Hopkins, E. Lee, and T. Luo, "Effect of light atoms on thermal transport across solid-solid interfaces," *Phys Chem Chem Phys,* vol. 21, no. 31, pp. 17029-17035, Aug 21 2019.

[13] R. Rastgarkafshgarkolaei, J. Zhang, C. A. Polanco, N. Q. Le, A. W. Ghosh, and P. M. Norris, "Maximization of thermal conductance at interfaces via exponentially mass-graded interlayers," *Nanoscale,* vol. 11, no. 13, pp. 6254-6262, Mar 28 2019.

[14] X.-M. Bai, M. R. Tonks, Y. Zhang, and J. D. Hales, "Multiscale modeling of thermal conductivity of high burnup structures in UO2 fuels," *J Nucl Mater,* vol. 470, pp. 208-215, 2016.

[15] K. Chockalingam, P. C. Millett, and M. R. Tonks, "Effects of intergranular gas bubbles on thermal conductivity," (in English), *J Nucl Mater,* vol. 430, no. 1-3, pp. 166-170, Nov 2012.

[16] S. Y. Hu, A. M. Casella, C. A. Lavender, D. J. Senor, and D. E. Burkes, "Assessment of effective thermal conductivity in U-Mo metallic fuels with distributed gas bubbles," (in English), *J Nucl Mater,* vol. 462, pp. 64-76, Jul 2015.
[17] L. Liang, Y. S. Kim, Z.-G. Mei, L. K. Aagesen, and A. M. Yacout, "Fission gas bubbles and recrystallization-induced degradation of the effective thermal conductivity in U-7Mo fuels," *J Nucl Mater,* vol. 511, pp. 438-445, 2018.
[18] P. C. Millett and M. Tonks, "Meso-scale modeling of the influence of intergranular gas bubbles on effective thermal conductivity (vol 412, pg 281, 2011)," (in English), *J Nucl Mater,* vol. 413, no. 2, pp. 136-136, Jun 15 2011.
[19] L. Z. Zhang *et al.*, "A quantitative comparison between C-0 and C-1 elements for solving the Cahn-Hilliard equation," (in English), *J Comput Phys,* vol. 236, pp. 74-80, Mar 1 2013.
[20] P. C. Millett, D. Wolf, T. Desai, S. Rokkam, and A. El-Azab, "Phase-field simulation of thermal conductivity in porous polycrystalline microstructures," *Journal of Applied Physics,* vol. 104, no. 3, 2008.
[21] M. R. Tonks *et al.*, "Development of a multiscale thermal conductivity model for fission gas in UO2," (in English), *J Nucl Mater,* vol. 469, pp. 89-98, Feb 2016.
[22] H. Wang, S. Biswas, Y. S. Han, and V. Tomar, "A phase field modeling based study of microstructure evolution and its influence on thermal conductivity in polycrystalline tungsten under irradiation," (in English), *Comp Mater Sci,* vol. 150, pp. 169-179, Jul 2018.
[23] M. Mohr, L. Daccache, S. Horvat, K. Brühne, T. Jacob, and H.-J. Fecht, "Influence of grain boundaries on elasticity and thermal conductivity of nanocrystalline diamond films," *Acta Mater,* vol. 122, pp. 92-98, 2017.
[24] J.-P. Crocombette and L. Gelebart, "Multiscale modeling of the thermal conductivity of polycrystalline silicon carbide," *J Appl Phys,* vol. 106, no. 8, 2009.
[25] S. Aubry, C. J. Kimmer, A. Skye, and P. K. Schelling, "Comparison of theoretical and simulation-based predictions of grain-boundary Kapitza conductance in silicon," *Phys Rev B,* vol. 78, no. 6, 2008.
[26] M. Khafizov *et al.*, "Thermal Conductivity in Nanocrystalline Ceria Thin Films," *J Am Ceram Soc,* vol. 97, no. 2, pp. 562-569, 2014.
[27] K. Shrestha *et al.*, "The grain-size effect on thermal conductivity of uranium dioxide," *J Appl Phys,* vol. 126, no. 12, 2019.
[28] Z. R. Zhong and X. W. Wang, "Thermal transport in nanocrystalline materials," (in English), *J Appl Phys,* vol. 100, no. 4, Aug 15 2006.
[29] T. Watanabe, S. B. Sinnott, J. S. Tulenko, R. W. Grimes, P. K. Schelling, and S. R. Phillpot, "Thermal transport properties of uranium dioxide by molecular dynamics simulations," *J Nucl Mater,* vol. 375, no. 3, pp. 388-396, 2008.
[30] K. P. Tai, A. Lawrence, M. P. Harmer, and S. J. Dillon, "Misorientation dependence of Al2O3 grain boundary thermal resistance," (in English), *Appl Phys Lett,* vol. 102, no. 3, Jan 21 2013.
[31] S. Fujii, T. Yokoi, and M. Yoshiya, "Atomistic mechanisms of thermal transport across symmetric tilt grain boundaries in MgO," (in English), *Acta Mater,* vol. 171, pp. 154-162, Jun 1 2019.

[32] S. Fujii, T. Yokoi, C. A. J. Fisher, H. Moriwake, and M. Yoshiya, "Quantitative prediction of grain boundary thermal conductivities from local atomic environments," *Nat Commun,* vol. 11, no. 1, p. 1854, Apr 15 2020.
[33] A. Sood *et al.*, "Direct Visualization of Thermal Conductivity Suppression Due to Enhanced Phonon Scattering Near Individual Grain Boundaries," (in English), *Nano Lett,* vol. 18, no. 6, pp. 3466-3472, Jun 2018.
[34] D. Xu, R. Hanus, Y. Xiao, S. Wang, G. J. Snyder, and Q. Hao, "Thermal boundary resistance correlated with strain energy in individual Si film-wafer twist boundaries," (in English), *Mater Today Phys,* vol. 6, pp. 53-59, Aug 2018.
[35] J. Hickman and Y. Mishin, "Thermal conductivity and its relation to atomic structure for symmetrical tilt grain boundaries in silicon," (in English), *Physical Review Materials,* vol. 4, no. 3, Mar 30 2020.
[36] Y. Q. Zeng, C. L. Lo, S. J. Zhang, Z. H. Chen, and A. Marconnet, "Dynamically tunable thermal transport in polycrystalline graphene by strain engineering," (in English), *Carbon,* vol. 158, pp. 63-68, Mar 2020.
[37] A. Giri and P. E. Hopkins, "A Review of Experimental and Computational Advances in Thermal Boundary Conductance and Nanoscale Thermal Transport across Solid Interfaces," (in English), *Adv Funct Mater,* vol. 30, no. 8, Feb 19 2020.
[38] E. T. Swartz and R. O. Pohl, "Thermal-Boundary Resistance," (in English), *Rev Mod Phys,* vol. 61, no. 3, pp. 605-668, Jul 1989.
[39] M. R. Tonks *et al.*, "Multiscale development of a fission gas thermal conductivity model: Coupling atomic, meso and continuum level simulations," (in English), *J Nucl Mater,* vol. 440, no. 1-3, pp. 193-200, Sep 2013.
[40] F. Badry, R. Brito, M. G. Abdoelatef, S. McDeavitt, and K. Ahmed, "An Experimentally Validated Mesoscale Model of Thermal Conductivity of a UO2 and BeO Composite Nuclear Fuel," *Jom-Us,* vol. 71, no. 12, pp. 4829-4838, 2019.
[41] N. X. Zhou, T. Hu, and J. Luo, "Grain boundary complexions in multicomponent alloys: Challenges and opportunities," (in English), *Curr Opin Solid St M,* vol. 20, no. 5, pp. 268-277, Oct 2016.
[42] C. W. Nan, "Physics of Inhomogeneous Inorganic Materials," (in English), *Prog Mater Sci,* vol. 37, no. 1, pp. 1-116, 1993.
[43] F. Badry and K. Ahmed, "A new model for the effective thermal conductivity of polycrystalline solids," *Aip Adv,* vol. 10, no. 10, 2020.
[44] J. P. Crocombette and L. Gelebart, "Multiscale modeling of the thermal conductivity of polycrystalline silicon carbide," (in English), *J Appl Phys,* vol. 106, no. 8, Oct 15 2009.
[45] S. Torquato, *Random heterogeneous materials : microstructure and macroscopic properties* (Interdisciplinary applied mathematics ; v. 16). New York: Springer, 2002.
[46] L. Z. Zhang, M. R. Tonks, P. C. Millett, Y. F. Zhang, K. Chockalingam, and B. Biner, "Phase-field modeling of temperature gradient driven pore migration coupling with thermal conduction," (in English), *Comp Mater Sci,* vol. 56, pp. 161-165, Apr 2012.
[47] J. D. Hales *et al.*, "Asymptotic expansion homogenization for multiscale nuclear fuel analysis," *Comp Mater Sci,* vol. 99, pp. 290-297, 2015.
[48] M. Teague, M. Tonks, S. Novascone, and S. Hayes, "Microstructural modeling of thermal conductivity of high burn-up mixed oxide fuel," (in English), *Journal of Nuclear Materials,* vol. 444, no. 1-3, pp. 161-169, Jan 2014.

[49] X. M. Bai, M. R. Tonks, Y. F. Zhang, and J. D. Hales, "Multiscale modeling of thermal conductivity of high burnup structures in UO2 fuels," (in English), *J Nucl Mater,* vol. 470, pp. 208-215, Mar 2016.
[50] P. C. Millett, M. R. Tonks, K. Chockalingam, Y. F. Zhang, and S. B. Biner, "Three dimensional calculations of the effective Kapitza resistance of UO2 grain boundaries containing intergranular bubbles," (in English), *J Nucl Mater,* vol. 439, no. 1-3, pp. 117-122, Aug 2013.
[51] M. C. Teague, B. S. Fromm, M. R. Tonks, and D. P. Field, "Using Coupled Mesoscale Experiments and Simulations to Investigate High Burn-Up Oxide Fuel Thermal Conductivity," *Jom-Us,* vol. 66, no. 12, pp. 2569-2577, 2014.
[52] L. Q. Chen and W. Yang, "Computer simulation of the domain dynamics of a quenched system with a large number of nonconserved order parameters: The grain-growth kinetics," *Phys Rev B Condens Matter,* vol. 50, no. 21, pp. 15752-15756, Dec 1 1994.
[53] L.-Q. Chen, "Phase-Field Models for Microstructure Evolution," *Annual Review of Materials Research,* vol. 32, no. 1, pp. 113-140, 2002.
[54] H. W. Pan, G. M. Han, Z. Q. Han, and B. C. Liu, "Phase field simulation on microstructure evolution in solidification and aging process of squeeze cast magnesium alloy," *IOP Conference Series: Materials Science and Engineering,* vol. 84, 2015.
[55] K. Ahmed and A. El-Azab, "An analysis of two classes of phase field models for void growth and coarsening in irradiated crystalline solids," *Materials Theory,* vol. 2, no. 1, 2018.
[56] M. G. Abdoelatef, F. Badry, D. Schwen, C. Permann, Y. Zhang, and K. Ahmed, "Mesoscale Modeling of High Burn-Up Structure Formation and Evolution in UO2," *Jom-Us,* vol. 71, no. 12, pp. 4817-4828, 2019.
[57] E. A. Scott *et al.*, "Phonon scattering effects from point and extended defects on thermal conductivity studied via ion irradiation of crystals with self-impurities," *Physical Review Materials,* vol. 2, no. 9, 2018.
[58] T. Mutschele and R. Kirchheim, "Hydrogen as a Probe for the Average Thickness of a Grain-Boundary," (in English), *Scripta Metall Mater,* vol. 21, no. 8, pp. 1101-1104, Aug 1987.
[59] S. Indris, P. Heitjans, H. E. Roman, and A. Bunde, "Nanocrystalline versus microcrystalline Li2O : B2O3 composites: Anomalous ionic conductivities and percolation theory," (in English), *Phys Rev Lett,* vol. 84, no. 13, pp. 2889-2892, Mar 27 2000.
[60] M. Ulrich, A. Bunde, S. Indris, and P. Heitjans, "Li ion transport and interface percolation in nano- and microcrystalline composites," *Phys. Chem. Chem. Phys.,* vol. 006, no. 13, pp. 3680-3683, 2004.
[61] Q. G. Zhang, B. Y. Cao, X. Zhang, M. Fujii, and K. Takahashi, "Size effects on the thermal conductivity of polycrystalline platinum nanofilms," *Journal of Physics: Condensed Matter,* vol. 18, no. 34, pp. 7937-7950, 2006.
[62] I. N. Laboratory. (2020, June 10). *Moose framework* [Online]. Available: https://mooseframework.org/.
[63] C. J. Permann, M. R. Tonks, B. Fromm, and D. R. Gaston, "Order parameter re-mapping algorithm for 3D phase field model of grain growth using FEM," *Comp Mater Sci,* vol. 115, pp. 18-25, 2016.

[64] K. H. Sarma, J. Fourcade, S. G. Lee, and A. A. Solomon, "New processing methods to produce silicon carbide and beryllium oxide inert matrix and enhanced thermal conductivity oxide fuels," *J Nucl Mater,* vol. 352, no. 1-3, pp. 324-333, 2006.
[65] R. Latta, S. T. Revankar, and A. A. Solomon, "Modeling and measurement of thermal properties of ceramic composite fuel for light water reactors," (in English), *Heat Transfer Eng,* vol. 29, no. 4, pp. 357-365, Apr 2008.
[66] S. Ishimoto, M. Hirai, K. Ito, and Y. Korei, "Thermal Conductivity of UO2-BeO Pellet," *Journal of Nuclear Science and Technology,* vol. 33, no. 2, pp. 134-140, 1996.
[67] C. B. Garcia, R. A. Brito, L. H. Ortega, J. P. Malone, and S. M. McDeavitt, "Manufacture of a UO2-Based Nuclear Fuel with Improved Thermal Conductivity with the Addition of BeO," (in English), *Metall Mater Trans E,* vol. 4, no. 2-4, pp. 70-76, Dec 2017.
[68] R. Liu, W. Zhou, P. Shen, A. Prudil, and P. K. Chan, "Fully coupled multiphysics modeling of enhanced thermal conductivity UO 2 –BeO fuel performance in a light water reactor," *Nuclear Engineering and Design,* vol. 295, pp. 511-523, 2015.
[69] CINDAS. (2019, Aug 7). *Global Benchmark for Critically Evaluated Materials Properties Data,* [Online]. Available: https://cindasdata.com/Applications/TPMD/.
[70] J. K. Fink, "Thermophysical properties of uranium dioxide," (in English), *J Nucl Mater,* vol. 279, no. 1, pp. 1-18, May 2000.
[71] R. D. Cowan, "Pulse Method of Measuring Thermal Diffusivity at High Temperatures," *J Appl Phys,* vol. 34, no. 4, pp. 926-927, 1963.
[72] J. C. M. Garnett, "Colours in metal glasses and in metallic films.," (in English), *Philos T R Soc Lond,* vol. 203, pp. 385-420, Sep 1904.
[73] J. C. M. Garnett, "Colours in metal glasses, in metallic films, and in metallic solutions - II," (in English), *Philos T R Soc Lond,* vol. 205, pp. 237-288, May 1906.
[74] K. Bakker, "Using the finite element method to compute the influence of complex porosity and inclusion structures on the thermal and electrical conductivity," (in English), *Int J Heat Mass Tran,* vol. 40, no. 15, pp. 3503-3511, Oct 1997.
[75] L. H. Ortega, B. Blamer, K. M. Stern, J. Vollmer, and S. M. McDeavitt, "Thermal conductivity of uranium metal and uranium-zirconium alloys fabricated via powder metallurgy," *J Nucl Mater,* vol. 531, 2020.
[76] W. J. Carmack *et al.*, "Metallic fuels for advanced reactors," *J Nucl Mater,* vol. 392, no. 2, pp. 139-150, 2009.
[77] L. C. W. G. L. HOFMAN, and T. H. BAUER, "METALLIC FAST REACTOR FUELS," *Progress in Nuclear Energy,* vol. Volume 31, no. Issues 1–2, pp. 83-110, 1997.
[78] Y. Il Chang, "Technical rationale for metal fuel in fast reactors," (in English), *Nucl Eng Technol,* vol. 39, no. 3, pp. 161-170, Jun 2007.
[79] L. C. Walters, "Thirty years of fuels and materials information from EBR-II," (in English), *J Nucl Mater,* vol. 270, no. 1-2, pp. 39-48, Apr 1 1999.
[80] J. M. Harp, D. L. Porter, B. D. Miller, T. L. Trowbridge, and W. J. Carmack, "Scanning electron microscopy examination of a Fast Flux Test Facility irradiated U-10Zr fuel cross section clad with HT-9," *J Nucl Mater,* vol. 494, pp. 227-239, 2017.
[81] Y. S. Kim, G. L. Hofman, and A. M. Yacout, "Migration of minor actinides and lanthanides in fast reactor metallic fuel," *J Nucl Mater,* vol. 392, no. 2, pp. 164-170, 2009.

[82] K. Pietrak and T. S. Wisniewski, "A review of models for effective thermal conductivity of composite materials," (in English), *J Power Technol,* vol. 95, no. 1, pp. 14-24, 2015.
[83] J.C. Maxwell (Ed.), *Treatise on Electricity and Magnetism*. Oxford: Oxford University Press, 1873/1904.
[84] D. P. H. Hasselman and L. F. Johnson, "Effective Thermal-Conductivity of Composites with Interfacial Thermal Barrier Resistance," (in English), *J Compos Mater,* vol. 21, no. 6, pp. 508-515, Jun 1987.
[85] H. Kämpf and G. Karsten, "Effects of Different Types of Void Volumes on the Radial Temperature Distribution of Fuel Pins," *Nuclear Applications and Technology,* vol. 9, no. 3, pp. 288-300, 1970.
[86] K. L. Peddicord and M. Ades, "Prediction of Thermal-Conductivity of Sphere-Pac Fuel," (in English), *T Am Nucl Soc,* vol. 28, no. Jun, pp. 552-553, 1978.
[87] K. L. Peddicord, M. E. Cunningham, and A. Tripathi, "Porosity Correction to Thermal-Conductivity Based on Analytical Temperature Solutions," (in English), *T Am Nucl Soc,* vol. 28, no. Jun, pp. 548-549, 1978.
[88] T. H. Bauer, "A General Analytical Approach toward the Thermal-Conductivity of Porous-Media (Vol 36, Pg 4181, 1993)," (in English), *Int J Heat Mass Tran,* vol. 37, no. 2, pp. 345-345, Jan 1994.
[89] N. Castin, L. Malerba, and R. Chaouadi, "Prediction of radiation induced hardening of reactor pressure vessel steels using artificial neural networks," *J Nucl Mater,* vol. 408, no. 1, pp. 30-39, 2011.
[90] L. Y. Liang, Y. S. Kim, Z. G. Mei, L. K. Aagesen, and A. M. Yacout, "Fission gas bubbles and recrystallization-induced degradation of the effective thermal conductivity in U-7Mo fuels," (in English), *J Nucl Mater,* vol. 511, pp. 438-445, Dec 1 2018.
[91] D. Yun, A. M. Yacout, M. Stan, T. H. Bauer, and A. E. Wright, "Simulation of the impact of 3-D porosity distribution in metallic U-10Zr fuels," (in English), *J Nucl Mater,* vol. 448, no. 1-3, pp. 129-138, May 2014.
[92] G. B. Fedorov and E. A. Smirnov, "Heat capacity of uranium-zirconium systems," *Soviet Atomic Energy,* vol. 25, no. 1, pp. 795-797, 1968/07/01 1968.
[93] M. R. Tonks, D. Gaston, P. C. Millett, D. Andrs, and P. Talbot, "An object-oriented finite element framework for multiphysics phase field simulations," (in English), *Computational Materials Science,* vol. 51, no. 1, pp. 20-29, Jan 2012.
[94] J. C. Maxwell, *A Treatise on Electricity and Magnetism*. USA: Cambridge University Press, 2010.
[95] E. EDGE. (2020, November). *Thermal conductivity of gases chart* [Online]. Available: https://www.engineersedge.com/heat_transfer/thermal-conductivity-gases.htm.
[96] W. M. Chen and X. M. Bai, "Temperature and composition dependent thermal conductivity model for U-Zr alloys," (in English), *J Nucl Mater,* vol. 507, pp. 360-370, Aug 15 2018.
[97] Y. S. Kim, T. W. Cho, and D.-S. Sohn, "Thermal conductivities of actinides (U, Pu, Np, Cm, Am) and uranium-alloys (U–Zr, U–Pu–Zr and U–Pu–TRU–Zr)," *J Nucl Mater,* vol. 445, no. 1-3, pp. 272-280, 2014.
[98] M. Y. a. K. Y. Yoichi TAKAHASHI, "Thermophysical properties of uranium-zirconium alloys," *Journal ofNuclear Materials,* vol. 154, no. 1, pp. 141-144.

[99] R. W. P. Y. S. Touloukian, C. Y. Ho, and P. G. Klemens, *Thermophysical Properties of Matter*
- *The TPRC Data Series. Thermal Conductivity - Metallic Elements and Alloys*. 1970.
[100] Tim Mueller, Aaron Gilad Kusne, and a. R. Ramprasad, "Machine Learning in Materials Science: Recent Progress and Emerging Applications," in *Reviews in Computational Chemistry*, vol. 29, A. L. Parrill and K. B. Lipkowitz, Eds. United States: wiley, 2016, pp. 186-273.
[101] Expert System. (2020, May 6). *Blog, machine learning* [Online]. Available: https://expertsystem.com/machine-learning-definition/.
[102] Towards Data Science. (2020, November 16). *A Medium publication sharing concepts, ideas, and codes.* [Online]. Available: https://towardsdatascience.com/the-bayesian-paradigm-ridge-regression-418af128ae8c.
[103] Dataaspirant. (2020, November 16). *Learn. Data science. Now* [Online]. Available: https://dataaspirant.com/random-forest-algorithm-machine-learing/.
[104] T. Hastie, R. Tibshirani, and J. H. Friedman, *The elements of statistical learning : data mining, inference, and prediction*, 2nd ed. (Springer series in statistics,). New York, NY: Springer, 2009, pp. xxii, 745 p.
[105] DeepAI. (2020, November 16). *Random Forests* [Online]. Available: https://deepai.org/machine-learning-glossary-and-terms/random-forest.
[106] G. James, D. Witten, T. Hastie, and R. Tibshirani, *An introduction to statistical learning : with applications in R* (Springer texts in statistics,, no. 103). New York: Springer, 2013, pp. xvi, 426 pages.
[107] M. M. Mukaka, "Statistics Corner- A guide to appropriate use of Correlation coefficient in medical research," *Malawi Medical Journal,* vol. 24(3), pp. 69-71, September 2012 2012.
[108] G. Lebon, "Heat conduction at micro and nanoscales: A review through the prism of Extended Irreversible Thermodynamics," (in English), *J Non-Equil Thermody,* vol. 39, no. 1, pp. 35-59, Mar 2014.
[109] N. Provatas and K. Elder, *Phase-field methods in materials science and engineering*. Weinheim: Wiley-VCH, 2010, pp. xiii, 298 p.
[110] K. Ahmed and A. El-Azab, "Phase-field modeling of microstructure evolution in nuclear materials," in *Handbook of Materials Modeling*, W. Andreoni and S. Yip, Eds.: springer, 2018, pp. 1-21.

APPENDIX A

ZR PRECIPITATES MODEL

Precipitates of U-Zr fuel

We develop here a model to calculate the total precipitates volume as function in Zr wt%.

The atom density is the number of atoms per cm^3, it could be obtained based on the atom percent γ_j,

$$N_j = \left(\frac{\gamma_j}{100}\right)\left(\frac{\rho\, N_v}{M}\right) \tag{A.1}$$

or based on weight percent w_i,

$$N_i = \left(\frac{w_i}{100}\right)\left(\frac{\rho\, N_v}{M_i}\right) \tag{A.2}$$

By equating Eqs (A.1) and (A.2)

$$\frac{\gamma_j}{M} = \frac{w_i}{M_i} \tag{A.3}$$

Since

$$\left(\frac{1}{M}\right) = \left(\frac{1}{100}\right)\sum_i \left(\frac{w_i}{M_i}\right) \tag{A.4}$$

So,

$$\left(\frac{1}{M}\right) = \left(\frac{1}{100}\right)\left(\frac{w_{Zr}}{M_{Zr}} + \frac{w_U}{M_U}\right) \tag{A.5}$$

Since

$$w_{Zr} + w_U = 100 \tag{A.6}$$

So,

$$\left(\frac{1}{M}\right) = \left(\frac{1}{100}\right)\left(\frac{w_{Zr}}{M_{Zr}} + \frac{100 - w_{Zr}}{M_U}\right) \tag{A.7}$$

By combining Eqs A.3 and A.7, we can obtain this relation

$$\gamma_{Zr} = w_{Zr}\frac{M}{M_{Zr}} = \frac{w_{Zr}}{\left(\frac{M_{Zr}}{100}\right)\left(\frac{w_{Zr}}{M_{Zr}} + \frac{100 - w_{Zr}}{M_U}\right)} \tag{A.8}$$

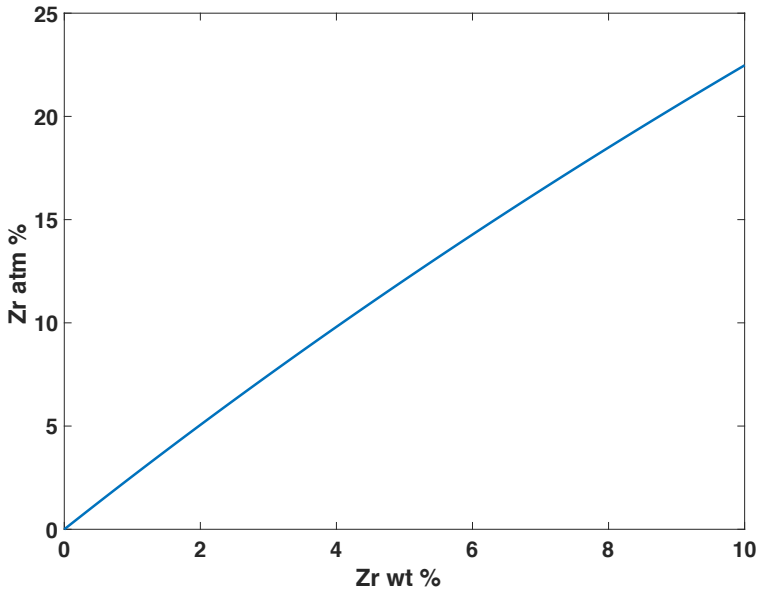

Figure 46. Plotting of Zr atom percent vs Zr wight percent of U-Zr fuel.

Now, let's redefine the atom percent of zirconium

$$\gamma_{Zr} = \frac{N_{Zr}}{N_{Zr} + N_U} \tag{A.9}$$

Where N_{Zr} and N_U represent the zirconium and uranium atom density, respectively.

Then, let's define a new parameter x called the precipitation fraction, which is the ratio of zirconium precipitated atoms to the total atoms of zirconium.

$$x = \frac{n_{Zr-p}}{n_{Zr-tot}} \tag{A.10}$$

Where n_{Zr-p} and n_{Zr-tot} represent the total precipitated zirconium atoms and total zirconium atoms, respectively.

$$n_{Zr-tot} = N_{Zr}\, V\, \rho_{TD} \tag{A.11}$$

Where V and ρ_{TD} are the total volume and theoretical density of U-Zr fuel, respectively.
Due to the precipitation phenomenon, and based on the conservation of mass principle, the initial Zr weight percent reduces in the fuel matrix as the volume of Zr precipitates increases and frequently the atom percent decreases. By using the precipitation fraction the modified atom percent γ_{Zr}^{m}, can be governed by the following equation:

$$\gamma_{Zr}^{m} = \frac{N_{Zr}(1-x)}{N_{Zr} + N_{U}} \tag{A.12}$$

By rearranging,

$$\gamma_{Zr}^{m} = \gamma_{Zr}(1-x) \tag{A.13}$$

So, the precipitation fraction based on the initial atom and modified atom percent is,

$$x = 1 - \frac{\gamma_{Zr}^{m}}{\gamma_{Zr}} \tag{A.14}$$

By recalling Eq.A.8 and modified it to be based on the modified weight (w_{Zr}^{m}) and atom percent, we obtain

$$\gamma_{Zr}^{m} = \frac{w_{Zr}^{m}}{\left(\frac{M_{Zr}}{100}\right)\left(\frac{w_{Zr}^{m}}{M_{Zr}} + \frac{100 - w_{Zr}^{m}}{M_{U}}\right)} \tag{A.15}$$

By substituting Eq. A.13 in A. 15, and rearranging, we obtain

$$x = 1 - \frac{w_{Zr}^{m}/\gamma_{Zr}}{\left(\frac{M_{Zr}}{100}\right)\left(\frac{w_{Zr}^{m}}{M_{Zr}} + \frac{100 - w_{Zr}^{m}}{M_{U}}\right)} \tag{A.16}$$

By combining Eq. A.14 and A. 10, and rearranging, we obtain

$$n_{Zr-p} = n_{Zr-tot}\left(1 - \frac{\gamma_{Zr}^{m}}{\gamma_{Zr}}\right) \tag{A.17}$$

By substituting Eq. A.11 in A. 17, and rearranging, we obtain

$$n_{Zr-p} = N_{Zr}\, V\, \rho_{TD}\left(1 - \frac{\gamma_{Zr}^{m}}{\gamma_{Zr}}\right) \tag{A.18}$$

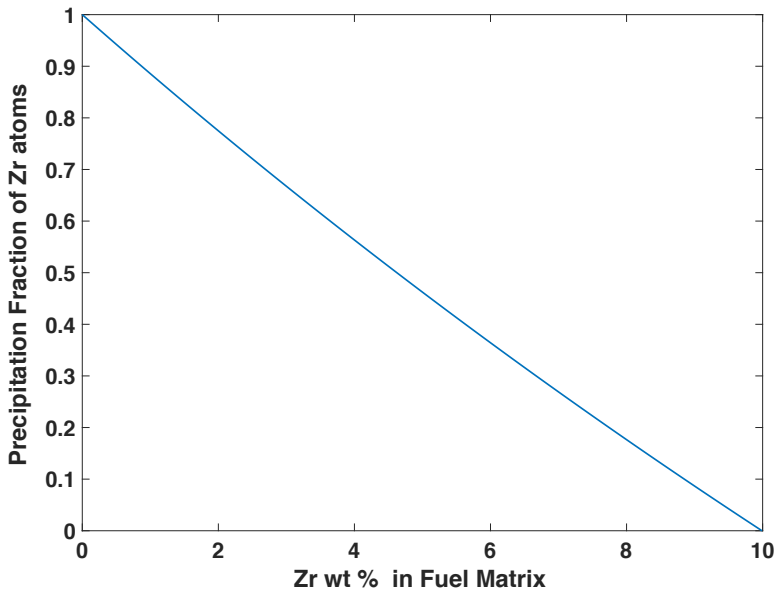

Figure 47. Plotting of precipitation fraction vs, the weight percent of zirconium atoms in U-Zr fuel.

By substituting Eq. A.1 in A. 18, and rearranging, we obtain

$$n_{Zr-p} = \left(\frac{\rho\, N_v}{M}\right) V\, \rho_{TD}(\gamma_{zr} - \gamma_{Zr}^{m}) \tag{A.19}$$

Now, the precipitated zirconium atoms can be calculated by Eq. A.19

Since Zr precipitates are assumed as pure Zr, to get the volume of the Zr precipitates, the total amount of Zr precipitated atoms should be divided by the atom density of pure zirconium. First, the atom density of pure Zr atom can obtained by,

$$N_{Zr-Pure} = \left(\frac{\rho_{Zr}\, N_v}{M_{Zr}}\right) \tag{A.20}$$

By dividing Eq. A.11 in A. 17, and rearranging, we obtain

$$V_{Pr} = \left(\frac{M_{Zr}}{M}\right)\left(\frac{\rho}{\rho_{Zr}}\right) V\, \rho_{TD}(\gamma_{zr} - \gamma_{Zr}^{m}) \tag{A.21}$$

Now, the volume of zirconium precipitates can be calculated by Eq. A.21, and the volume fractions can be calculated by,

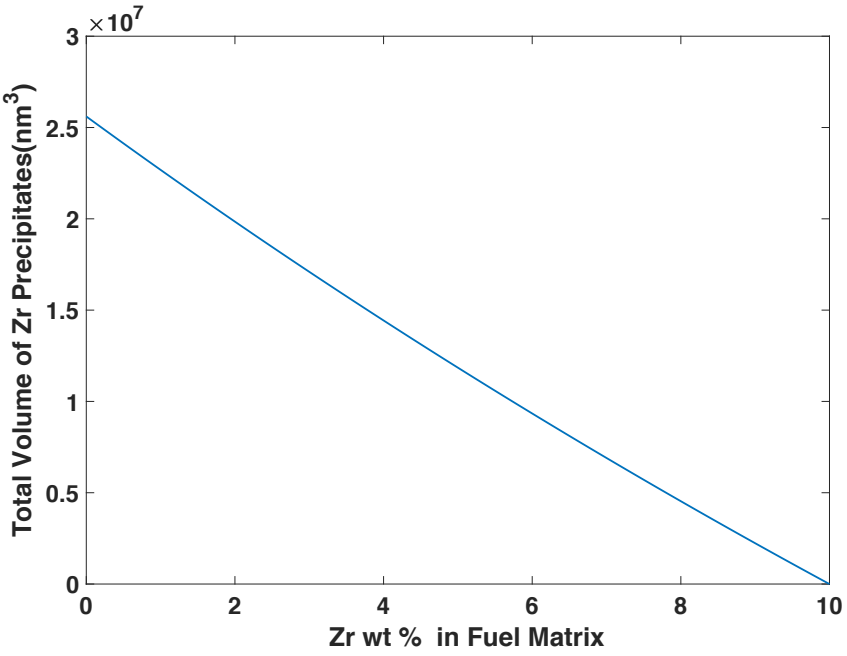

Figure 48. Total volume of Zr precipitates vs Zr weight percent in U-Zr fuel matrix.

$$V_{Pr} = \left(\frac{M_{Zr}}{M}\right)\left(\frac{\rho}{\rho_{Zr}}\right)\rho_{TD}(\gamma_{Zr} - \gamma_{Zr}^{m}) \tag{A.22}$$